HETEROGENEOUS SHOCK ENERGY DEPOSITION IN SHOCK WAVE CONSOLIDATION OF METAL POWDERS

Thesis by

Andrew Howard Mutz

In Partial Fulfillment of the Requirements
for the Degree of
Doctor of Philosophy

California Institute of Technology
Pasadena, California

1991

(Submitted May 23, 1991)

TO MY PARENTS

ACKNOWLEDGMENTS

Knowing full well there are unintended omissions, I gratefully thank Prof. Thad Vreeland for his teaching, advice and encouragement, and both Prof. and Mrs. Vreeland for their friendship and hospitality.

I surely would not have been able to work at Caltech for so long without the entertaining distractions which made life here pleasurable. Barry Krueger provided many of those distractions, as well as able scientific help completing the Keck Dynamic Compactor, and his untimely death leaves a deep silence. The help and humor of Concetto Geremia are also unforgotten in his absence. Dave Lee sparked nearly electric excitement at times. I also thank Phil Askenazy, Pascal Yvon, Brigitte Kruse, Doug Pearson, the Keck lab applied physics and material science folks, George Clovis, the Caltech fencing team, and the Garveys and Infra–Red Sox softball teams.

Technical collaborations are also numerous. Dr. Prakash Kasiraj performed the first of the shock consolidation experiments on Markomet 1064 on the 20mm gun in the Caltech Seismology Lab, in collaboration with Prof. Thomas Ahrens. Prakash also taught me the fundamentals of shock physics. Prof. Naresh Thadhani made the TEM and optical observations of Markomet 1064 and Pyromet 718. Dr. Ricardo Schwartz collaborated on the design and construction of the thermocouple experiments. The members of Caltech's Central Engineering Services machine shop, led by Norm Keidel and Louis Johnson, not only fabricated most of the Keck Compactor but also suggested design changes which caused it to work.

ABSTRACT

Shock wave consolidation of powder is a high deformation rate process in which a shock wave generated by an explosive or a colliding projectile rapidly densifies and bonds together the powder particles into a solid compact. The deposition of the shock energy during this process is highly inhomogeneous on the powder particle scale. Evidence of the extent and pattern of the energy deposition was provided by recovery experiments performed using an initially crystalline alloy which solidifies to a metallic glass upon rapid quenching from the liquid state. The amount of metallic glass was measured and analyzed using a heat flow model. The energy deposited during the shock wave passage was best modeled as deposited partly into the particle bulk and partly onto particle surfaces. To investigate this inhomogeneity, and the powder parameters which influence it, a propellant driven gas gun was designed, built and utilized. The planarity of the shock waves produced using the targets designed for the gun was established. Powder–powder thermocouples were impacted with powders of varying sizes to establish the effect of particle size on energy deposition. Small particles in contact with large ones were inferred to absorb the greater fraction of shock energy. Hardened and unhardened steel powder was shocked to investigate the effect of particle hardness on energy distribution. The recovered compacts were not measurably affected by the initial hardness. Compaction experiments were performed on a Ni based super–alloy and on a SiC reinforced Ti matrix composite to test some of the practical applications of the process and the target designs developed. Superior tensile properties were observed in the shock consolidated and heat treated Ni based 718 alloy. The SiC reinforced composite was recovered in the intended net shape with no macro–cracks in the compact body, but with fractured SiC particles.

TABLE OF CONTENTS

LIST OF ILLUSTRATIONS

Figure

LIST OF TABLES

Table

CHAPTER 1

INTRODUCTION

1.1 Overview

Shock wave consolidation is a process for forming low porosity, well bonded solid material from an initially very porous powdered material. A shock wave, generated by a high explosive or high velocity impactor, is driven through the powder. The shock wave densifies and bonds the media of interest. Ideally, a completely nonporous and fully bonded solid results. Interest in the process stems from the promise of forming parts of materials not amenable to conventional casting or sintering processes. For example, diamond powder has been explosively compacted to a dense, polycrystalline solid [1,2]. Successful static sintering of diamond requires treatment at approximately 2000° K and 60 kbar [3], and is difficult though commercially viable. Also, metastable materials such as amorphous metal alloys may only be synthesized in powder, ribbon, or sheet form. These materials can be consolidated to bulk solids via shock wave consolidation [4].

Several difficulties with shock consolidation exist. Reflected tensile waves generated by the interaction of the shock wave and the target assembly often act to disassemble the shocked material. The powders do not always completely bond to one another. The compacts produced may have very large residual strains. These difficulties are magnified with very hard, brittle materials, which are often of greatest interest. Research on improved target geometries [5], particle scale shock wave models [6], and the use of post–consolidation annealling [7,8] are addressing these problems, but the ultimate commercial success of shock wave consolidation as a manufacturing technique is uncertain [9].

The shock consolidation process functions by preferentially depositing energy at particle junctions, bonding the powder together while leaving particle interiors relatively cool. In this manner, total energy well below that required to melt the material is sufficient to densify and bond the powder to solid. This preferential heating is often intense enough to melt portions of the powder particles.

In this thesis, the preferential deposition of shock energy is experimentally investigated in several metallic systems. Recovered samples are examined for evidence of melting and freezing during shock consolidation. This data is analyzed to determine the extent of energy localization, and the dependence of total energy and hardness on this phenomenon. Real–time evidence of preferential heating is gathered through the use of powder thermocouples, and used to determine the effect of particle size and size distribution on energy localization.

1.2 Historical Background

Shock wave consolidation of powders was first studied as a means of fabricating material in the late 1940s and early 1950s. Powders were placed in waterproof bags and submerged in a pressure vessel. A gunpowder charge generated the pressure wave in the water and compacted the powder. This method was used to compact titanium carbide particles with nickel as a binder [10]. This method was difficult to characterize and was supplanted by direct explosive application [11] and by striking the powder with explosively accelerated pistons [12]. Early work built on explosive and shock wave data generated during WWII, especially during the Manhattan project, when the first plane wave experiments were conducted [13]. WWII and post–war secrecy no doubt lead to separate and independent efforts in shock physics in several nations. Early shock consolidation experiments were hindered by the lack of basic research and knowledge about the high pressure dynamic behavior of solids and powders; the systematic studies of high pressure behavior of materials published in the late 1950s provided a foundation for the study of dynamic compaction. Materials were studied under moderate shock pressures of 100–150 kbar by Walsh and Christian [14]. Higher pressures (400–4000 kbar) were used to characterize materials by Al'tschuler et al. [15]. Primed now with physical data, systematic study of shock consolidation could begin. A combination of successful shock techniques including explosive welding [16] and diamond synthesis [17] sparked new interest in shock wave consolidation of powders. Explosive powder consolidation was demonstrated by Pearson in 1961 [11], and Porembka et al. successfully consolidated uranium dioxide for nuclear fuel in 1963 [18].

Active research in shock wave powder consolidation has continued since the mid 1960s. Early systematic studies were carried out by Bergmann and Barrington [7] and by Kormer et al. [19]. This effort has not resulted in widespread commercialization of the process. While high quality samples of metal and ceramic materials have been manufactured on a small scale [5,20], the process has either been unsuccessful or uncompetitive on a commercial scale. Elimination of cracking and difficulties with scale–up have proven formidable obstacles. Particle scale modeling has made inroads towards an understanding of factors affecting interparticle bonding [6]. Shock wave simulations at the continuum level have aided the development of fixtures which minimize cracking [5]. Thorough reviews of the research work done in shock consolidation have been compiled by Gourdin [21] by Thadhani [9], and (for ceramics) by Graham and Sawaoka [22].

1.3 Continuum Shock Waves in Porous Media

The study of shock waves in powders begins with the study of shock waves in a continuous medium. Excellent texts on shock wave phenomena by Zel'dovich and Raizer [23] and by Kinslow [24] explain the following material at greater length. The changes in density, velocity, and internal energy across the shock wave front are constrained by the conservation of mass, momentum and energy. These constraints, reformulated as the Rankine–Hugoniot relationships, are contained in the following equations:

1.1) $$P - P_0 = \rho_0 V u$$

1.2) $$\rho_0 V = \rho_1 (V - u)$$

1.3) $$E_1 - E_0 = \frac{1}{2}(P + P_0)\left(\frac{1}{\rho_0} - \frac{1}{\rho_1}\right)$$

where P is the shock pressure, P_0 is the initial pressure, V is the shock wave velocity, u is the velocity of material behind the shock front, ρ_0 is the initial density, ρ_1 is the final density, E_1 is the specific energy of material behind the shock front, and E_0 is the specific energy of material before the shock front. The initial pressure is often assumed as zero; the shock pressure is typically 10^5 bar. This trio of equations includes four unknowns.

The missing piece of the puzzle is the pressure – material velocity relationship for the material being shocked. This relationship, known as the material's 'Hugoniot', allows determination of all other continuum parameters of interest. The Hugoniot of a material is typically derived by measuring the velocity at which a shock wave (generated by an impact with a material of known shock properties) propagates. If neither material is well parameterized, the particle and shock wave velocity in one material are simultaneously measured.

The most significant difference (for shock wave consolidation) between shock waves in solids and in porous media is the far greater residual increase in density in a porous material. The work done by the shock pressure acting through the density change is retained in the shocked material, and therefore a porous material is heated significantly by the passage of a shock wave. For example, a 10 GPa shock wave travelling through solid copper and then released will heat the copper by 6° C [25]. A wave of the same pressure passing through porous copper containing 40% voids will heat the copper by about 950° C [26].

The measurement of shock Hugoniots for each powder material and porosity is fortunately not necessary. Many porous materials have been studied [27] (and the results tabulated), and models such as that developed by Simons and Legner [28], provide accurate predictions of shock Hugoniot data in powders from the solid shock Hugoniot data. The Simons and Legner model predicts the powder Hugoniot using the material's density, ρ, isentropic compressibility, κ, Gruneisen coefficient, μ, and distension, m. The distension is the solid density, ρ_0, divided by the powder density, ρ_{00}. The Gruneisen coefficient is a dimensionless thermodynamic parameter defined as

1.4) $$\mu = \frac{1}{\rho}\left(\frac{\partial P}{\partial E}\right)_{\rho} .$$

The particle – velocity, u, vs. shock pressure, P, relationship given by this model is:

1.5) $$u^2 = \frac{P}{\rho_0} \frac{m(1 + P\kappa) - 1}{1 + (1 + \mu/2)P\kappa} .$$

The Gruneisen coefficient can be calculated, but the value is often derived by fitting powder Hugoniot measurements to the model. Typical values range between 1.2 and 2.5.

Shock rise time is the final parameter of interest in the continuum Hugoniot. How quickly and over what distance do material properties change from pre–shock to shock values? In solids, the shock front may be as thin as a few atomic layers [29]. In a powder, the particle size limits the sharpness of the discontinuity. This follows logically; as the material ceases to appear continuous, the shock wave front cannot further sharpen. Schwarz et al. measured the rise time of a shock wave to be of the order of the traversal time of a single particle by the shock wave [30]. The 2–D simulations of Berry and Williamson predict similar rise times [6]. Some additional data on this subject is presented in Chapter 4.

1.4 Shock Wave Behavior at the Particle Scale

Unlike the continuum behavior of shock waves, the particle scale propagation of shock waves is not very well understood. The difficulty stems from the rapidity of the process, the variations in material behavior, and the variations in particle morphology. For particles in the 100μm range, all deformation will typically take place in 50 ns, the time for a shock wave travelling at 2 km/s to traverse the particle diameter. (See chapter 4 for experimental verification.) During this time, parts of the particle will experience large (on the order of 100%) strain. Strain rate effects in the 10^7/s range are not easily measured; dynamic Kolsky bar experiments typically reach strain rates of 10^5/s [31]. Beyond this, dynamic stress–strain measurements are very difficult, and therefore constitutive relationships for materials under shock deformation are typically extrapolated from lower strain rate data.

Ballistic punch experiments can achieve strain rates similar to those in shock consolidation; shear strains of 100 were observed in 2024–T6 aluminum struck by a flat–ended projectile, and the shear bands formed in less than 12 μs [32]. Strain localization occurs by the formation of shear bands. Large shear stresses occur in shock wave consolidation of powders, but it is unclear whether shear band formation is a dominant mode of strain localization for most metals during shock consolidation.

Above some shear strain rate, most metals will exhibit shear instability and strain localization as plastic deformation causes thermal softening to exceed strain hardening [33]. Very narrow 'microshear bands' were observed in particle interiors of a shock consolidated nickel–based alloy [34].

More generally, the localization of strain near particle surfaces is a feature of shock wave consolidation of powders. The problem has been numerically modeled for shock wave consolidation in two dimensions (rod consolidation) [6]. Under shock conditions the momentum of accelerated material is a major perturbation to the quasistatic case. Average and maximum strains increase dramatically, and the characteristic scalloped particle boundary pattern is observed in the plane parallel to the shock propagation direction, as shown in Fig. 1.1. In a series of consolidation experiments at different pressures and energies with spherical titanium alloy powder [13], the transition from densification without bonding to complete bonding was explored. Onset of bonding was first observed at particle junctions with an angle of nearly 45° to the shock direction. This corresponds to the direction of maximum shear for the impact of one sphere into the other. As energy was increased, the bonding became uniform.

Strain energy localization is often sufficient to melt material near particle boundaries [35,36]. Melting can aid in interparticle bonding by dispersing surface contaminants and welding particles together. Some systems will only bond well if some interparticle melting is present [37]. The presence of melted material may be inferred from the etching behavior of melted and rapidly quenched material. This technique was used to evaluate the fraction of material melted as discussed in Chapter 3. The degree of strain localization is expected to depend on a wide variety of parameters including material strength, thermal softening rate, thermal conductivity, strain hardening behavior, particle size and shape distribution, and the macroscopic shock parameters. Some of these parameters are explored in this thesis, but the phenomena is not completely understood.

1.4 Scope of this work

Particle scale energy deposition by shock waves is the subject addressed herein. The influences of particle size and shape are investigated within material systems, and some hardness effects are also explored. Both recovery experiments and real–time data are examined. Some of the ideas developed are applied to the fabrication of a near–net shape ceramic reinforced metal matrix composite. In order to conduct these experiments, a 35mm smooth–bore propellant driven gas gun was constructed. This facility is described in some detail.

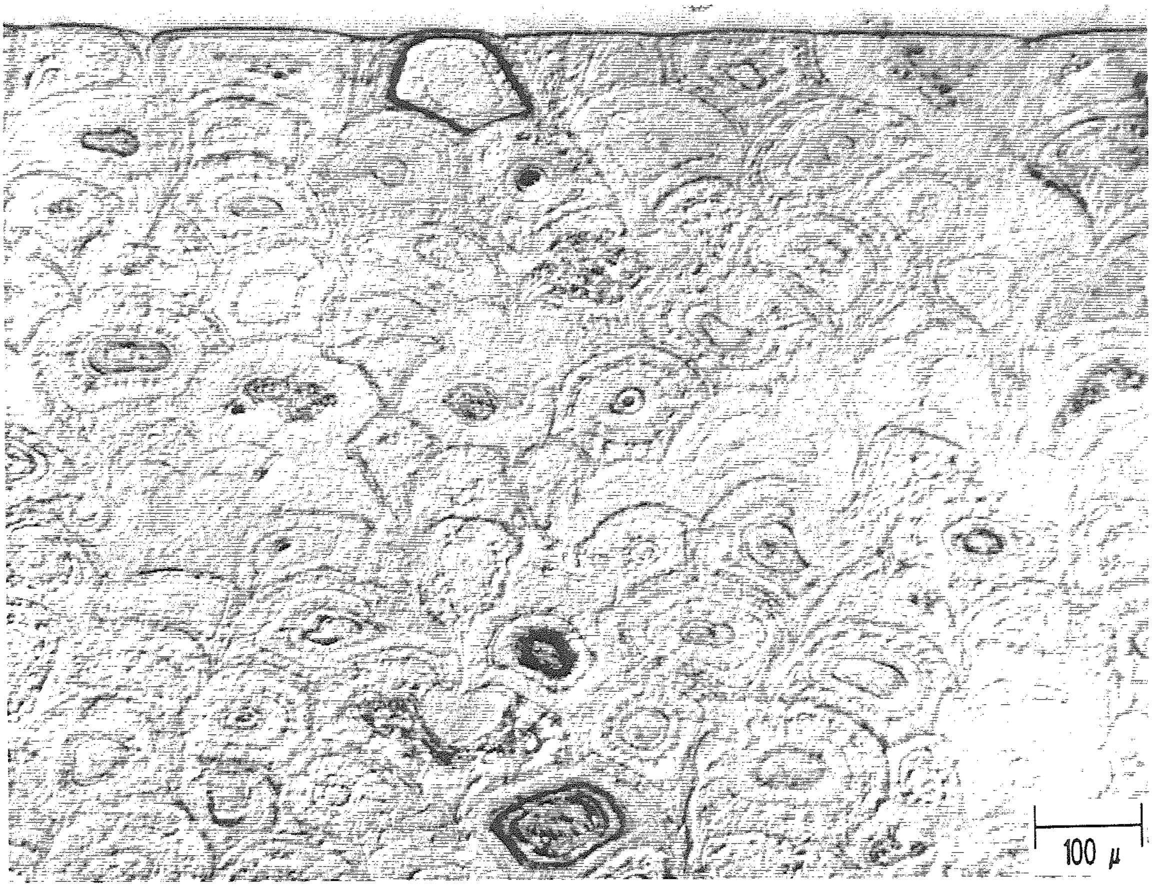

Fig. 1.1 Micrograph of polished and etched shock consolidated nickel. The powder particles were initially 125–150μm spheres, and were shocked by a 303 SS flyer plate travelling at 1.08 km/s. The shock wave travelled from the top to bottom in the section shown.

References

1. D. K. Potter and T. J. Ahrens, Appl. Phys. Let. **5**, 317 (1987).
2. K. Kondo and S. Sawai, J. Am. Ceram. Soc. **73**, 1983 (1990).
3. R. H. Wentorf, R. C. DeVries, and F. P. Bundy, **208**, 873 (1980).
4. C. F. Cline and R. W. Hopper, Scripta Met. **11**, 1137 (1977).
5. G. E. Korth, J. E. Flinn, and R. C. Green, in *Metallurgical Applications of Shock–Wave and High–Strain–Rate Phenomena*, edited by L. E. Murr, K. P. Staudhammer, and M. A. Meyers (Dekker, New York, 1986), p. 129.
6. R. A. Berry and R. L. Williamson, in *Shock Waves in Condensed Matter*, edited by Y. Gupta (Plenum, New York, 1986), p. 341.
7. O. R. Bergmann and J. Barrington, J. Am Ceramic Soc. **49**, 502 (1966).
8. R. Prummer, Ber. Deutsche Keram. Ges. **50**, 75 (1973).
9. N. N. Thadhani, Adv. Mat. & Man. Proc. **3**, 493 (1988).
10. E. Karpick, Steel, **131**. 131 (1952).
11. J. Pearson, Am. Soc. of Tool and Manuf. Eng. SP–60–159 (1961).
12. E. W. La Rocca and J. Pearson, Rev. Sci. Inst. **29**, 848 (1958).
13. G. E. Duvall, in *Metallurgical Applications of Shock–Wave and High–Strain–Rate Phenomena*, edited by L. E. Murr, K. P. Staudhammer, and M. A. Meyers (Dekker, New York, 1986), p. 3.
14. J. M. Walsh and R. H. Christian, Phys. Rev. **97**, 1544 (1955).
15. L. V. Al'tschuler, K. K. Krupnikov, and M. I. Brazhnik, Soviet Physics JETP (Engl. Trans.) **7**, 614 (1958).
16. Cowan, G. R., and Holtzman, A. H., J. Appl. Phys. **34**, 928 (1963).
17. P. S. Decarli and J. C. Jamieson, Science. **133**, 821 (1961).
18. S. W. Porembka, C. C. Simons, and R. J. Carlson, in *Symposium on Powder Packed Uranium Dioxide Fuel Elements* (Norton Co., New York, 1963).
19. S. B. Kormer, A. I. Funtikov, V. D. Urlin, A. N. Kolesnikova, Soviet Phys. JETP (English Transl.) **15**, 477 (1962).
20. T. Akashi and A. B. Sawaoka, Adv. Ceram. Mat. **3**, 288 (1988).
21. W. H. Gourdin, Mat. Sci. **30**, 39 (1986).
22. R. A. Graham and A. B. Sawaoka, in *High Pressure Explosive Processing of Ceramics*, edited by R. A. Graham and A. B. Sawaoka (Transtech, Switzerland, 1986) p. 17.
23. Y. B. Zel'dovich and Y. P. Raiser, *Physics of Shock Waves and High Temperature Hydrodynamic Phenomena* (Academic Press, New York, 1958).
24. R. Kinslow, ed., *High Velocity Impact Phenomena* (Academic Press, New York, 1970).

25. R. G. McQueen, S. P. Marsh, J. W. Taylor, J. N. Fritz, and W. J. Carter, in *High–Velocity Impact Phenomena*, edited by R. Kinslow (Academic Press, New York, 1970).

26. Calculation based on Hugoniot parameters published in *LASL Shock Hugoniot Data*, and heat capacity from the *Handbook of Chemistry and Physics.*

27. S. P. Marsh, ed., *LASL Shock Hugoniot* (University of California, Los Angeles, 1980).

28. G. A. Simons and H. H. Legner, J. Appl. Phys. **53**, 934 (1982).

29. M. A. Mogilevsky, in *Shock Waves and High–Strain–Rate Phenomena in Metals*, edited by M. A. Meyers and L. E. Murr (Plenum, New York, 1981), p 538.

30. R. B. Schwarz, P. Kasiraj, and T. Vreeland Jr., in *Metallurgical Applications of Shock–Wave and High–Strain–Rate Phenomena*, edited by L. E. Murr, K. P. Staudhammer, and M. A. Meyers (Dekker, New York, 1986), p. 313.

31. K. A. Hartley, J. Duffy, and R. H. Hawley, J. Mech. Phys. Solids. **35**, 283 (1987).

32. A. L. Wingrove, Met. Trans. **4**, 1829 (1973).

33. H. C. Rogers, *Ann. Rev. Mater. Sci.* **9**, 283 (1979).

34. N. N. Thadhani, A. H. Mutz, P. Kasiraj, and T. Vreeland Jr., in *Metallurgical Applications of Shock–Wave and High–Strain–Rate Phenomena*, edited by L. E. Murr, K. P. Staudhammer, and M. A. Meyers (Dekker, New York, 1986), p. 247.

35. D. Raybould, D. G. Morris, and G. A. Cooper, J. Mat. Sci. **14**, 2523 (1979).

36. A. M. Staver, in *Shock Waves and High–Strain–Rate Phenomena in Metals*, edited by M. A. Meyers and L. E. Murr (Plenum, New York, 1981),p. 877.

37. P. Kasiraj, in *Shock Wave Consolidation of Metallic Powder* (PhD Thesis, California Institute of Technology, 1985), p. 121.

CHAPTER 2

THE KECK DYNAMIC COMPACTOR

2.1 Introduction

A recurring issue in the shock consolidation of powders by explosive compaction is the pressure–energy history of the resulting compact. The highly two or three–dimensional nature of the shock front in cylindrical and capsule type recovery fixtures leads to a variety of shock conditions in the compact. This variation itself changes with each new material shocked, which complicates efforts to characterize shock conditions in an assembly by calculating the history for one powder and extending the results to other materials [1]. The availability of powerful computing tools is beginning to ameliorate this difficulty, but analysis is still a difficult procedure. A one–dimensional shock condition is therefore very desirable if one wishes to measure material properties in response to particular shock wave pressures or velocities. This refers specifically to the initial shock front which consolidates the powder. In spite of clever momentum traps and geometries, reflected waves of varying magnitude and direction pass through the consolidated specimen. In a successful consolidation experiment these waves are not strong enough to fracture the consolidated material produced by the initial shock front. The issue of energy history is then simplified to a Hugoniot analysis of a one–dimensional shock condition. The pressure history is equally simple during the passage of the first shock front. The one–dimensional analysis is, of course, valid only in the region of material unaffected by edge waves created at the outer edges of the target and flyer.

To exploit the advantages of the one–dimensional geometry, a propellant gun has been built and used. The Keck Lab Dynamic Compactor facility was designed with shock consolidation and recovery in mind. The tested velocity range is between 600 and 1600 m/s. The design velocity of 2000 m/s has not been utilized; most metallic materials are consolidated in the velocity range of 750 to 1300 m/s. The 3m by 35 mm inner diameter (ID) smooth bore cannon barrel accelerates a 31.5 mm diameter flyer plate mounted on a nylon sabot 25 mm long down the evacuated barrel. The smokeless shotgun powder (nitrocellulose) used provides a stable, safe source of propellant gas. An electrically heated wire ignites the gunpowder. The velocity of the projectile is measured to within 1% by timing the interval between the interruption of two light beams. The target fixture is held to the end of the barrel under vacuum. The barrel itself is mounted on a damped carriage, to provide vibration isolation for the building; the compactor is installed on the third floor. A ductile iron tube surrounds the barrel as a safety shield. See Fig. 2.1.

The breech is unusual in that the cavity containing the gunpowder during ignition is of smaller diameter than the barrel ID. See Fig. 2.2. A maraging steel sleeve is designed to hold the powder and the ignition wire, which is sealed from the rest of the barrel. The gunpowder is not evacuated with the barrel. The sleeve fits closely in the breech, and screws to the breech block, where a small hole provides room for the ignition wire. The breech reinforcement and breech block are of C300 maraging steel and the breech reinforcements have been shrink fit into place to provide a permanent compressive load in the breech. A safety interlocked firing system is operated from a neighboring room.

The compactor is instrumented at the barrel extension, a six–inch tube with a threaded collar to attach it to the barrel, as shown in Fig. 2.3. An additional one–

inch long aluminum tube provides a sacrificial coupling to the target. This tube permits the sabot to clear the barrel extension before the flyer impacts the powder. The 17–4 PH steel barrel extension has four ports for the optical velicometry system, a single vacuum connection, and a fitting for a plastic microwave radar antenna. A doppler radar [e. g. 2] velocity system supplements the optical velocity measurement. A standard K band (25 GHz) doppler module (Plessey model GDHM32) was adapted to measure the projectile velocity during the entire time of flight. Though dispersion renders the measurement difficult at the muzzle, the radar does provide data on initial acceleration and time of flight. Flyer acceleration is essentially complete within the first 2m of barrel length. The terminal velocity is therefore accurately measured by the optical system. This provided a guide for choosing an appropriate propellant, and allowed estimates of breech pressure. (The radar is no longer used regularly.) The doppler radar signal, a 'beat' frequency signal produced by mixing the original and reflected microwave signal with a nonlinear mixer diode, was digitized at 1 MHz and later Fourier transformed in 512 point sections to produce a time–velocity history.

The optical velicometry system is driven by a tungsten filament lamp through a pair of fiber optic cables. The light beams are unfocused across the barrel extension, and only the center 0.125" of the beam is incident on the receiving fibers. These are connected to a pair of light–activated switches. The TTL compatible switches gate a 10 MHz oscillator crystal. A totalizing counter records the number of cycles. The count then represents the number of 0.1 μs intervals in which the first switch is open and the second switch is closed. An external reset prevents counts after the first set. The distance between the beams is 4.0 cm.

The barrel vacuum is also connected to the barrel extension. This vacuum system is independent of the recovery tank vacuum, and driven by a two–stage mechanical pump. The barrel and powder are typically evacuated to 100 mTorr prior to firing.

The recovery system decelerates the target containing the shocked powder as well as the momentum trap. The momentum trap and target are independently coupled to the rear of the recovery vacuum tank by industrial and automotive shock absorbers, respectively. The mounts for the target and momentum trap are hinged to the recovery tank floor. This allows relatively gentle recovery of the target. See Fig. 2.4.

The target ring is a key component of the gun system [Fig. 2.5]. The powder to be compacted must be contained prior to impact, prevented from flowing radially after impact, and removed as a single piece afterward. The Keck Compactor uses a 4340 steel ring four inches in outer diameter and 2.5 inches long for this purpose. The rings are heat treated to Rc 50. A steel liner with an aluminum plug is then pressed into the ring. The unloading wave catches up to the initial shock wave in the powder (before it reaches the aluminum plug). The aluminum plug is an adequate impedance match to many metal powders, and the momentum trap coupled to the plug is also aluminum. After the shot, the plug, compact, and flyer plate are in the liner. The liner is pressed out and cut along the side to remove the compact. The ring is reusable when honed out for a slightly larger liner. The ring is typically vacuum sealed to the barrel extension to evacuate the powder, but the powder cavity can be sealed and filled with a gas prior to loading.

2.2 Experiment

A metallic glass ribbon, $Ni_{76.4}Cr_{19}Si_{2.3}B_{1.5}C_{.08}$, produced by Allied Corporation as MBF 50, was ball milled to powder. The amorphous nature was confirmed by x–ray diffraction. The powder was shock consolidated by a 5 mm thick 303 SS flyer plate travelling at 1.06 km/s. These shots were initiated to produce fully bonded metallic glasses. The powder was at 54% of full density before consolidation, and fully densified by the shock wave. After shock consolidation, the compact was sectioned, polished, and etched to reveal grain boundaries. The compact is crystalline to a depth of 3.5 mm. See Fig. 2.6. This corresponds to the position at which the shock wave pressure is reduced by the reflection from the back of the flyer plate. Beyond this level, the powder is, in effect, consolidated by the plastic sabot at considerably lower pressure. This is depicted in the time–displacement diagram of Fig. 2.7. (The pressures in each zone are calculated using the Hugoniot parameters for Ni.)

The degree of planarity in the glass–crystalline boundary is evident. Even in the edge regions where deviations from planarity are expected, the energy deposited by the initial shock wave remained above the threshold required to heat the compact to the crystallization temperature. We have not carried out a detailed calculation of the energy deposition expected in the edge regions. The appearance of the compact suggests that the edge effect is relatively small in geometries which do not shock the entire recovery ring (unlike solid multi–cavity fixtures such as the Sawaoka fixtures [3]), but do contain the powder to limit radial flow.

2.3 Analysis

The position of the transition from crystalline to amorphous metal in the compact may be determined using the Simons and Legner powder Hugoniot model discussed in Chapter 1. The experimental parameters are summarized in Table 2.1. Values of κ and μ are estimated from elemental averages. The Hugoniot is not particularly sensitive to κ and μ in the range of parameters used in our experiments.

Once the speed of the shock wave is calculated, the thickness of the flyer and the sound speed of the flyer and glass are used to estimate the depth in the consolidated sample at which the rarefaction wave originating at the flyer–sabot boundary catches up to the shock wave. Material past this point has much less energy deposited in it. The transition between energy deposition levels is marked by the retention of metallic glass in the consolidated material. In the strongly shocked region, the energy deposited is sufficient to heat the powder beyond its crystallization temperature, 467° C. If the consolidation is indeed nearly one–dimensional, the boundary between amorphous and crystalline material will be planar. The boundary is actually somewhat convex, due to the complex "ring–down" at the flyer – cavity edge [Fig. 2.6]. It is far from the shallow cone generated in an unsupported powder. A rarefaction wave originating at the flyer plate perimeter would release the shock wave in a cone of angle 23° if the powder were not supported by the steel ring. This angle is calculated using the approach described in [4],

$$\cot \phi = \sqrt{(C/V)^2 - (V-u)^2/V^2}$$

where C is the relaxation wave speed in the consolidated powder (4.7 km/s), V is the shock wave velocity (1.86 km/s), and u is the particle velocity (0.86 km/s). The cone is not observed in the polished and etched sample. A 2–D finite element calculation simulating the shock wave consolidation of a rigidly supported powder by a flyer plate striking only the powder showed relatively very little edge relaxation [5].

An energy argument supports this observation as well. In an unsupported powder, energy dissipates radially into the unshocked powder. A rigid cylindrical containment does not allow energy to dissipate radially very well; only elastic waves will propagate, and they will be transmitted poorly at the powder to solid interface. The net effect is much smaller deviation from the plane wave condition in the powder. Note that since the steel container only interacts with the flyer plate through the powder, the steel is shocked to below the powder – flyer plate interaction pressure. There is no area in the compact that experiences more than the planar shock wave pressure.

2.4 Conclusions

A propellant gun has been constructed which can accelerate a flyer plate for shock wave consolidation and recovery of the consolidated samples.

A metallic glass has been shock consolidated to solid density and partially recrystallized. The slightly convex recrystallization boundary indicates a nearly one–dimensional shock condition obtained by striking only the contained powder with the flyer plate.

Acknowledgments

Aerojet Ordnance provided the the 35mm Mann barrel in the Keck Dynamic Compactor. The successful construction of the Compactor is due in great part to the skills and recommendations of the Caltech Central Engineering Shop. The Metglas experiment was carried out by Barry Krueger and Caltech undergraduate Joseph Bach, within the research program of Prof. Brent Fultz.

Table 2.1. Parameters used to calculated shock conditions in Metglas MBF 50.

Parameter	Value	Units
Density	7.49	gm/cc
Sound speed	4.7	km/s
Rate of wave speed increase with pressure	1.45	km/s–GPa
Gruneison coefficient	1.9	
Isentropic compressibility	.005	1/GPa

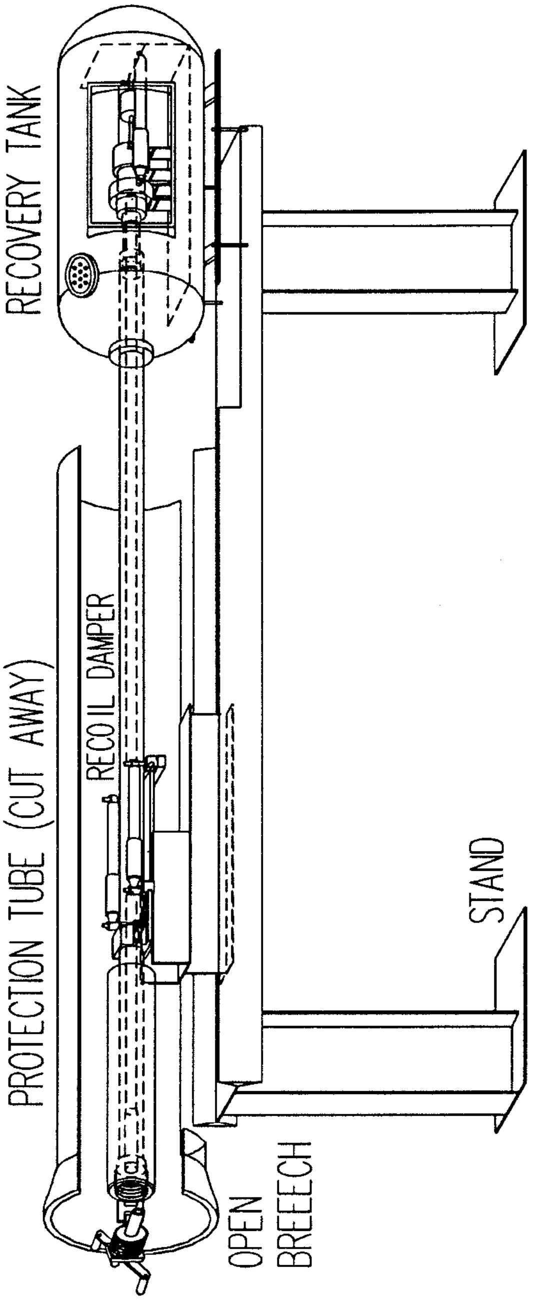

Fig. 2.1. Cutaway scale drawing of the Keck Dynamic Compactor. The ignition system, external vacuum systems, and barrel position drive have been excluded for clarity. The overall length of the assembly is approximately five meters.

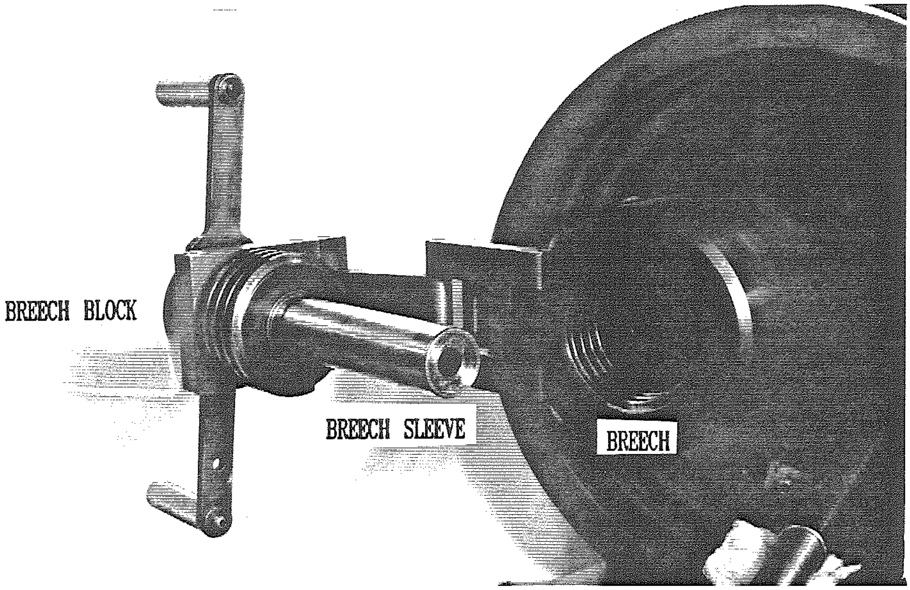

Fig. 2.2. Photograph of the open breech with the breech sleeve attached. The ignition wire passes through the breech block into the breech sleeve, and is connected to a fine tantalum wire, which ignites the propellant when current heats it.

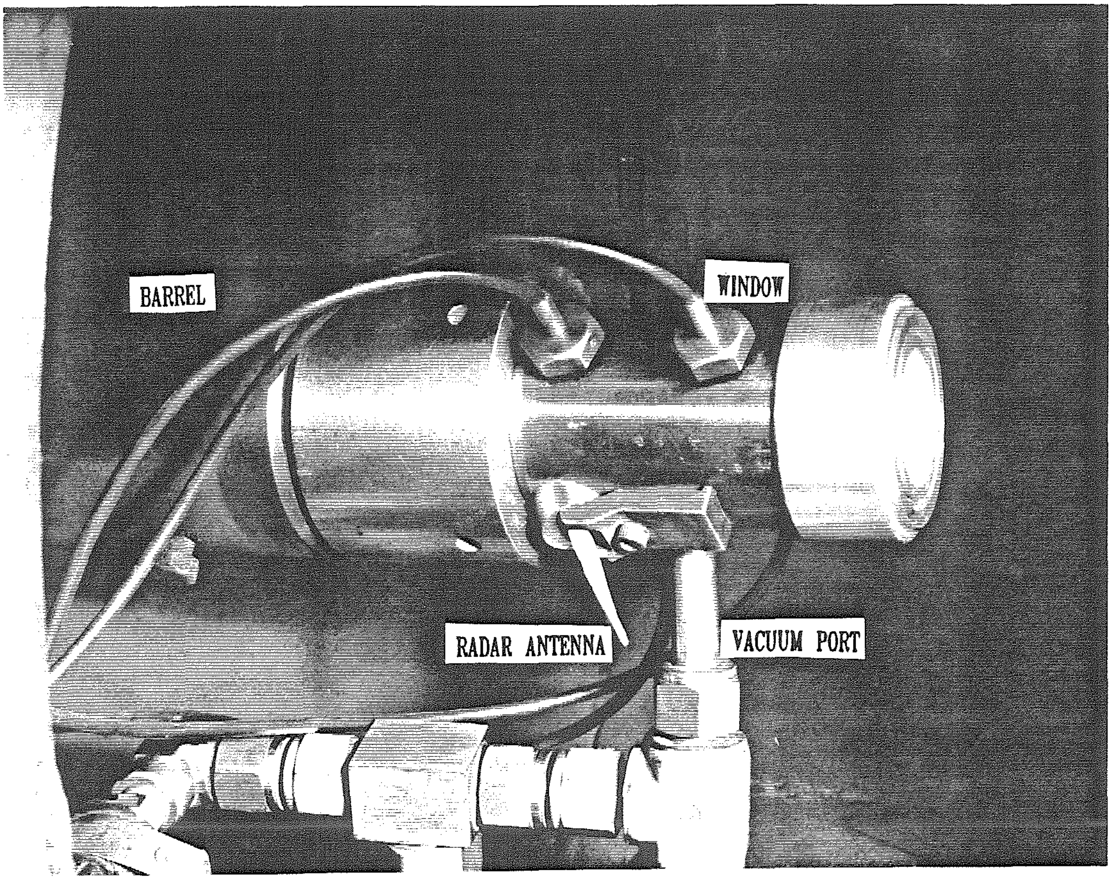

Fig. 2.3. Photograph of the barrel extension attached to the muzzle. The fiber optic connectors and radar antenna are attached to the barrel extension. The vacuum connection to the barrel is also here.

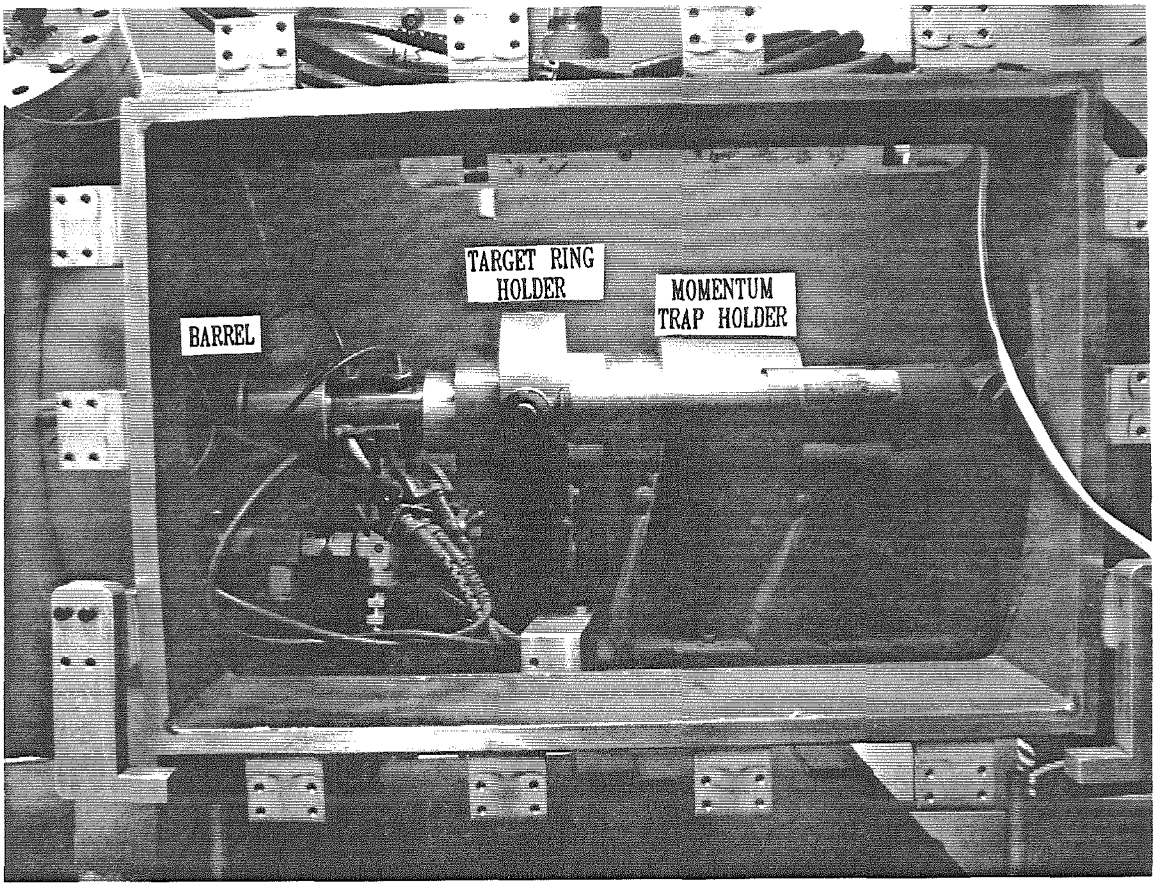

Fig. 2.4. Photograph of the recovery tank interior, showing the recovery system. The leftmost pair of hinges supports the target ring holder, connected to the rear of the tank with automotive shock absorbers. The right hand pair of hinges supports the momentum trap holder. The tank opening is 45 cm wide.

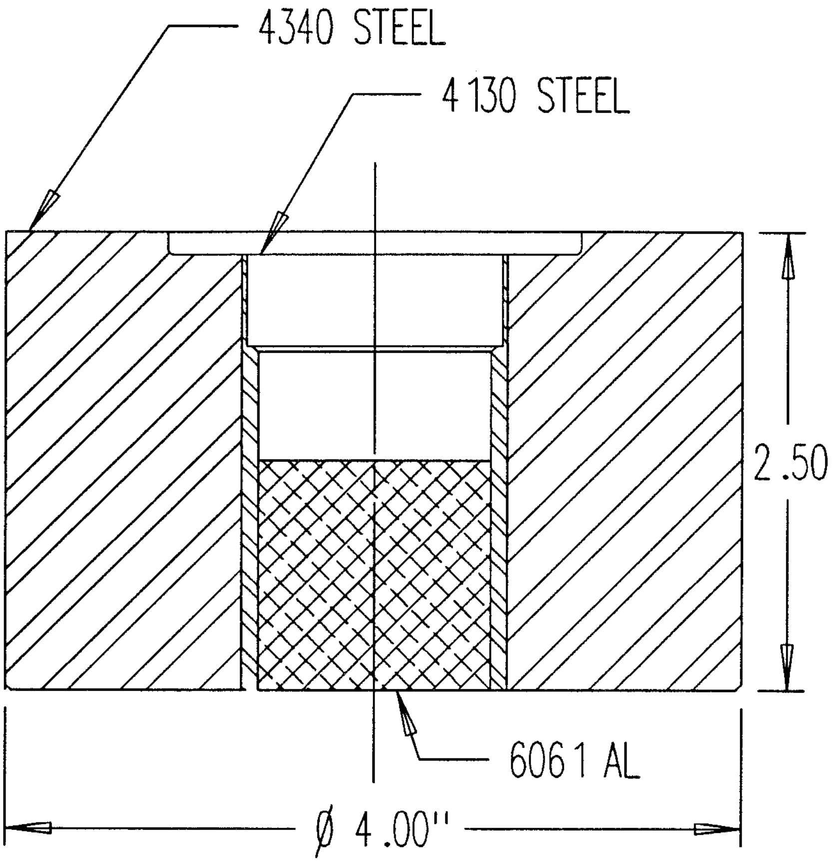

Fig. 2.5. Cross section drawing of the target ring. The powder to be shocked is loaded into the ring on top of the aluminum end plug, and either pressed or sealed into place before being loaded horizontally into the recovery tank.

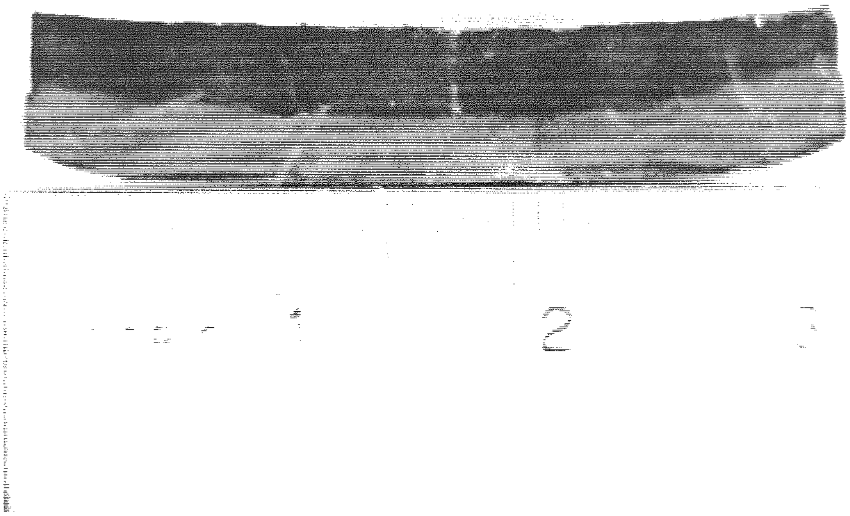

Fig. 2.6. Photograph of the polished and etched Metglas compact. The shock wave traversed the sample from top to bottom.

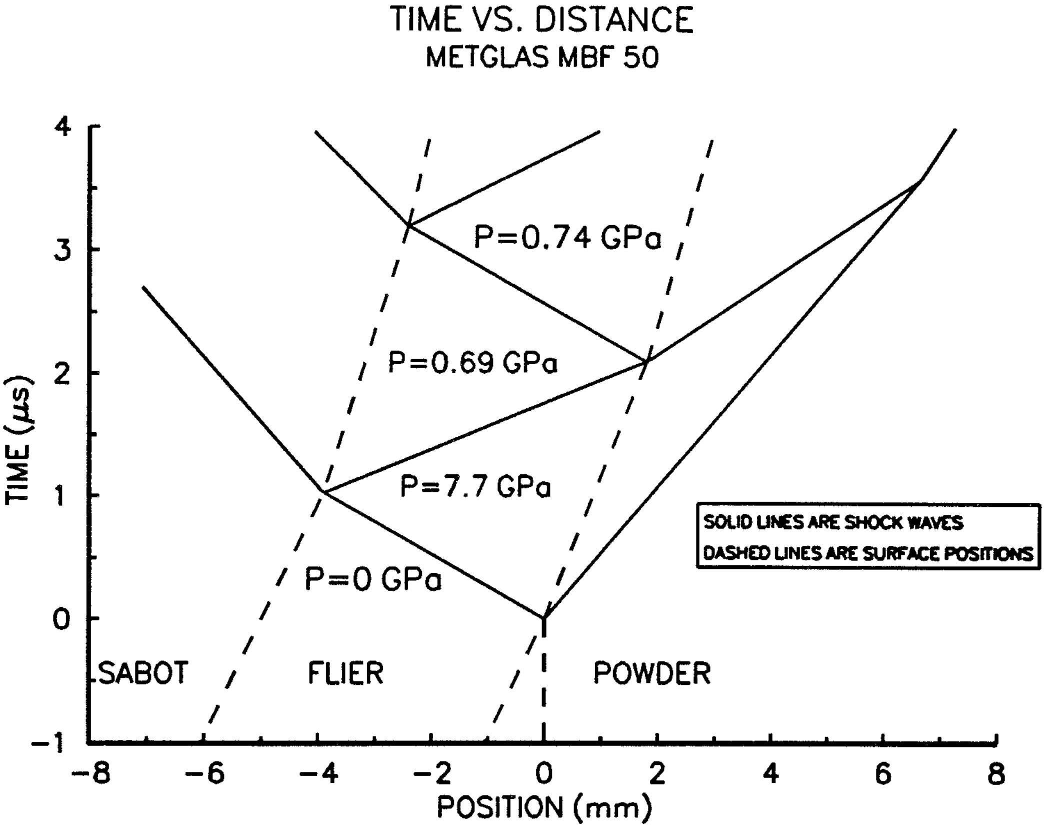

Fig. 2.7. The one–dimensional plane wave time–displacement history calculated for the Metglas consolidation experiment. (Edge effects are not calculated.)

References

1. F. L. Williams, B. Morosin, R. A. Graham, in *Metallurgical Applications of Shock–Wave and High–Strain–Rate Phenomena*, edited by L.E. Murr, K. P. Staudhammer, M. A. Meyers (Dekker Inc, New York, 1986) p. 1013.

2 J. D. Jackson, in *Classical Electrodynamics*, (Wiley, New York, 1975) p. 521.

3. A. Sawaoka, Mat. Res. Soc. Symp. Proc. **24**, 365 (1984).

4. Y. B. Zel'dovich and Y. P. Raiser, *Physics of Shock Waves and High Temperature Hydrodynamic Phenomena* (Academic Press, New York, 1958) p. 747.

5. T. Thomas, P. Bensussan, P. Chatagnac, and Y. Bienveu, in *Metallurgical Applications of Shock–Wave and High–Strain–Rate Phenomena*, edited by M. A. Meyers, L.E. Murr and K. P. Staudhammer (Dekker, New York, 1991).

CHAPTER 3

MELT FRACTION AND ENERGY DISTRIBUTION DURING SHOCK CONSOLIDATION

3.1 Introduction

Many of the publications describing microstructural changes during shock wave consolidation have pointed to microstructural changes as evidence of the melting of material during shock consolidation [1,2,3,4]. Some are less easily established than others; certain structures such as martensite in steel may be created by shear deformation without melt [5]. To clearly establish the presence and extent of melting during a shock consolidation experiment, a metallic glass forming alloy was prepared by ball milling a rapidly solidified ribbon, annealed to crystalline form, and then shock consolidated at a range of shock energies. When samples of this material were polished and etched, amorphous non–etching regions were observed. While many structural changes may accompany rapid plastic deformation, the formation of amorphous material from crystalline material requires either rapid solidification or (in the case of ordered alloys) very extensive plastic deformation. (Researchers have successfully made amorphized material by both mechanically alloying constituent materials via ball milling [6], and by mechanically deforming an ordered intermetallic through ball milling [7]). This mechanical process is distinct from shock consolidation in that average strains greatly exceed unity. For a discussion of solid state amorphization transformations, see Ref. 8. The mechanism may be a factor in the consolidation of ordered alloys. In the Markomet 1064 (FCC structure) discussed below, it will not be considered.

The existence and extent of melting during shock consolidation is of interest here principally in the limits the extent of melting places on energy distribution during shock wave passage. These limits are discussed in section 3.4, and addressed again in Chapter 4. Briefly, the minimum amount of melt during consolidation would appear if shock energy was deposited rather uniformly throughout the powder particles. In this case temperature excursions from equilibrium are minimized. Provided the shock energy is insufficient to raise the bulk temperature to the melting point, no melt would be observed. On the other hand, if energy is deposited very inhomogeneously, material can melt at shock energies far below that required to heat the bulk to the melting point. The maximum amount of melt possible is generated if all energy deposited goes to heating and melting a fraction of the material, leaving the remaining material unheated.

In perfectly clean materials, good bonding via shock consolidation should be achievable merely through full densification and cold welding. The presence of surface contamination on powder surfaces necessitates some amount of surface melting to effect good interparticle bonds. Knowledge of the amount of melt produced as a function of energy applied is therefore important to predict conditions for good bonding. The nature of surface contamination is obviously an important variable also; the presence of hydrated oxides has been observed to interfere with bonding in extremely energetic consolidation experiments [9].

In order to predict the amount of melt produced under several different models of energy deposition during shock consolidation, the spherically symmetric conduction of heat was calculated, including the motion of a solid–liquid interface. The spatial distribution of energy most consistent with the melt observed is inferred to best represent the actual energy distribution during shock consolidation. This simplified model is intended to determine the degree to which energy deposition favors particle exteriors, junctions, and asperities in preference to bulk flow.

Structural examination of the recovered material was performed using transmission electron microscopy by Thadhani et al. [10]. The principal observations of interest here are firstly, the confirmed amorphous nature of the non–etching material and secondly, the presence of retained crystalline metallic borides of large grain size in the amorphous regions. Their presence sets an upper limit on the temperature excursion of the melt in which they were entrained; MoB_2 melts at 2800° C [11].

3.2 Experiments

Irregularly shaped amorphous Markomet 1064 alloy powder ($Ni_{55.8}Mo_{25.7}Cr_{9.7}B_{8.8}$, 50 μm x 50 x 10 μm average platelet size) was prepared by ball–milling melt–spun ribbons. The metallic glass was crystallized by annealing at 900° C for two hours. See Fig. 3.1. (DTA scans revealed crystallization exotherms at 610° C and 825° C, and melting at 1240° C.) The annealed powder was loaded into hardened steel targets, depicted in Fig. 3.2, and pressed to 47% to 52% porosity as listed in Table 3.1.

The targets were mounted to the end of the 20mm inside diameter (ID) propellant driven gas gun in the Caltech Seismology Laboratory. This facility is similar in effect to the 35mm gun described in Chapter 2. The gunpowder charge is loaded into a shotshell. The shotshell is loaded into the breech, and ignited by a primer cap triggered with a solenoid–driven firing pin. The charge provides pressure to accelerate the polycarbonate sabot. The sabot is fitted with an "O"–ring seal to prevent blow–by of propellant gas. Shock consolidation was performed by impact with a 304 SS flyer plate supported by the lexan sabot. The projectile velocity was varied to obtain a variety of energies. The projectile velocities were measured by timing the interruption of two laser beams. The hardened steel targets permitted only small radial strains. Projectile velocities ranged from 0.96 to 1.44 km/s. Table 3.1 lists experimental parameters for the seven shots. The target is described in more detail in Ref. 12.

The recovered samples were sectioned by electric discharge machining, mounted, and mechanically polished. Marble's etch was used to reveal grain boundaries in the crystalline material. Amorphous material did not etch. A typical region is shown in Fig. 3.3. The original particles are flattened by the shock process, and appear to be bounded on some sides with amorphous material in rather large zones typically 10–20 μm in width, and frequently similar in size to the particles in higher energy shots. This implies melting is not limited to a uniform layer of particle surfaces, and may 'jet' into interparticle voids. In explosive welding, 'jetting' of melted material is often observed [13].

The quantity of non–etching material was measured from optical micrographs by tracing the melt pool boundaries on a digitizing tablet. Perpendicular and parallel sections were both analyzed. In the higher energy experiments, some of the larger non–etching regions contain very dark etching regions, indicative of a very fine microcrystalline structure. These regions are presumed to have melted and quenched during the shock process, but at a rate insufficient to prevent crystallization. This material is included in the estimate of material melted in Table 3.1. Selected area diffraction performed during transmission electron microscopy, described elsewhere in detail [10], confirmed the presence of amorphous and microcrystalline material in the shock consolidated samples.

3.3 Discussion

The thermodynamic analysis of these observations begins with a compilation of heat flow and capacity information for the Marko 1064. The parameters listed in Table 3.2 include heat capacity, latent heat of melting, and melting point, derived from DTA measurement. Thermal expansion coefficient and isentropic compressibility are estimated using the values for Ni. Pressure correction for melting temperature is similarly estimated. From this data, upper and lower bounds for material melted can be drawn. Given the shock energies listed in Table 3.1, none of the shots reach an equilibrium temperature close to the melting temperature of the alloy. Therefore, no melted material would be generated by completely homogeneous heating of the target powders. This represents the lower bound of material melted. At the other extreme, all energy could go to heating and melting that fraction of powder which could be melted. This represents an upper bound to the amount of material melted. More exactly, the upper bound of material melted, Mu, can be expressed [14]:

3.1)
$$\mathrm{Mu} = \frac{E_{sh}}{C_v(T_m - T_o) + L}$$

where E_{sh} is the shock energy. C_v is the mean heat capacity, T_m is the melting temperature of the alloy, T_o is the initial temperature of the alloy, and L is latent heat of melting. This upper bound, lower bound, and melt fraction data are displayed in Fig. 3.4.

Two facts are immediately clear. First, the data conforms closely to neither extreme of melt possible, falling squarely between them. Second, no melt at all is observed until the shock energy exceeds a critical minimum between 214 and 333

J/g. Another important observation is the dependence of melt fraction on initial porosity, as well as on (calculated) shock energy. The two experiments with energies of 415 and 419 J/g have quite different amounts of melted material. Either the shock pressure (increasing as porosity decreases at constant energy) has a strong influence on energy deposition, or the very high porosity material is not being shocked via the Raleigh line, and has a lower than calculated shock energy. Insufficient data is present to distinguish between these possibilities, but they must be considered during a more detailed analysis.

3.4 Energy Deposition Modeling

Treating the particle interactions in detail is a prohibitively complex business at best. The irregular particles are driven into one another, mutually shocked and deformed as the shock wave entrains them. Rapid plastic deformation deposits thermal energy. Portions of particles melt while other parts remain relatively cool. Porosity is removed through this disorganized process, and a dense compact is formed. Given sufficient time under load, the compacted material cools and bonds before release waves can knock it apart again.

All of these details are passed by in the following analysis. Only the thermal history of the material is considered. That history is simplified by limiting the geometry to a symmetrically heated sphere. The radius of the sphere is selected to match the areal diameter of the particles. The resulting sphere has a thermal response time similar to that of the original tabular particles. The behavior of the system is now easily amenable to simulation. Assuming the thermal history of the actual material is similar in favoring preferential heating at or near particle exteriors, the results of the simulation will roughly correspond to that seen in the experiments.

Thermal history simulations of this type were first used by Gourdin [14] to examine energy localization in shock consolidation of Cu. The thermal history of a sphere is simulated by integrating the thermal Laplacian,

3.2) $$\frac{\partial T}{\partial t} = \alpha\left[\frac{2}{r}\frac{\partial}{\partial r} + \frac{\partial^2}{\partial r^2}\right]T$$

using a finite element algorithm based on divided differences. The fixed space network method of Murray and Landis [15] was used to treat the moving liquid–solid interface. The motion of the interface is governed by

3.3) $$V_f = \frac{1}{\rho L}\left\{k_s\frac{\partial T_s}{\partial r}\bigg|_{r_m} - k_l\frac{\partial T_l}{\partial r}\bigg|_{r_m}\right\}$$

where V_f is the melt front velocity, ρ is density, L is latent heat, r_m is the melt front position, and T_s and T_l are the solid and liquid temperatures near the interface.

The heat is added to the sphere in several different patterns over the rise time, and these different boundary conditions result in very different maximum melt fractions. The four patterns are a) all heat into the particle surface, b) all heat into the solid–melt interface; no liquid heating beyond Tm, c) all heat into the particle bulk, biased towards the surface like the cube of radius, and d) 30% of the energy into the solid–liquid interface and 70% into the bulk of the sphere as in c). Pattern a) is identical to that used in [14].

To illustrate the effect of these energy flux patterns on the temperature gradients within the sphere, the temperature vs. radius is plotted at the end of the rise time for each case a)–d), in Fig. 3.5. Note the peak temperature in a) is approximately 10,000 ° C, while in case c) it is 900° C. In each case, the mean energy density is 333 J/g. A physical mechanism for heating the liquid phase to stellar temperatures is somewhat difficult to hypothesize, but this is intended as a qualitative rather than mechanistic model.

The more interesting results of these calculations are the predicted melt fraction vs. energy profiles, shown in Fig. 3.6 along with the measured melt data. Both input conditions which heat the sphere via a surface flux predict the onset of melt at 70 J/g. Heating the material through the bulk results in a high melt–onset energy over 500 J/g, even biasing the energy towards the surface. The mixture of surface flux and bulk heating best represents the data. The preferential heating of asperities and inter–particle junctions is seemingly not as localized as a pure surface flux, and the deformation energy is distributed within a significant thickness of material. As shock energy increases, the data is well fit by profile a). From a physical point of view, heating the melted alloy to 10,000° C is unlikely; deforming a low–viscosity liquid is not energetically demanding relative to solid deformation.

If the shock energies in the experiments conducted at 52% porosity are overestimated, as discussed earlier, the melt fraction predicted by pattern d) is a better fit. Also, the melt pools implied by amorphous material in the recovered compacts are large and poorly linked to solid interiors, relative to the melt shell postulated in the model. The melt in the model will quench more rapidly than in the regions observed. The amount of melt in the model is thus likely an underestimate.

3.5 Conclusions

Shock consolidation results in highly inhomogeneous deposition of shock energy. The formation and retention of amorphous Markomet 1064 during shock consolidation of crystallized powder implies the degree to which shock energy is localized. To predict both the onset and quantity of melt produced in a simple heat flux model, energy must be added preferentially at particle surfaces, but with a significant amount of energy expended into bulk deformation as well. In the case of a symmetrically heated sphere, a 70% bulk to 30% surface partition of shock energy provided the best agreement with the data.

Table 3.1. Shock conditions and quenched melt measurements of the Markomet 1064 shock consolidation experiments. Shock conditions are calculated based on the powder Hugoniot calculations discussed in Chapter 1.

Shot #	Powder Porosity	Flyer Vel. m/s	Shock Pressure GPa	Shock Energy J/g	Melt Measured
805	52%	962	5.1	333	0.46
807	52%	1440 *	3.4	214	0.02
808	52%	1090	6.3	414	0.12
813	52%	1340	9.65	592	0.28
814	52%	1188	7.58	481	0.25
815	47%	1220	10.1	467	0.22
816	49%	1124	8.94	419	0.20

* – polycarbonate flyer plate.

Table 3.2. Thermodynamic and physical parameters for Markomet 1064 alloy.

Parameter	Value	Units	Ref.
Density (ρ)	9.05	gm/cc	[16]
Melting temperature (Tm)	1240	°C	[17]
Average specific heat (Cv)	0.60	J/g–°C	[17]
Latent heat of fusion (L)	200	J/g	[18]
Average solid thermal (α) diffusivity	0.055	cm^2/s	[19]
Areal diameter (D)	42	μm	[16]
Pressure correction for melt temperature (for Ni)	27	°C/GPa	[20]
Isentropic compressibility (for Ni)	0.0057	1/GPa	[21]

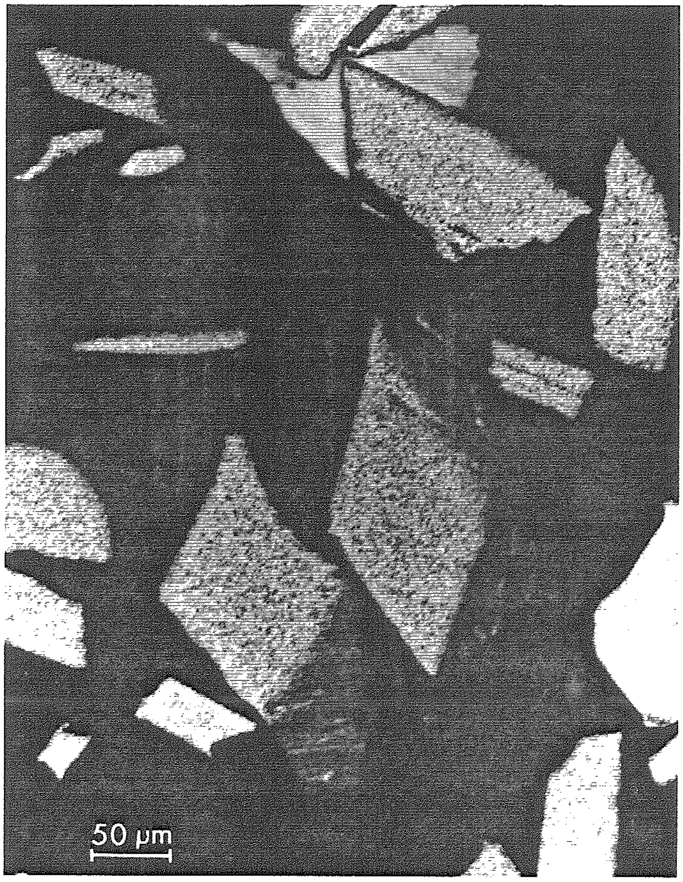

Fig. 3.1 Photograph of polished and etched particles of Markomet 1064 powder.

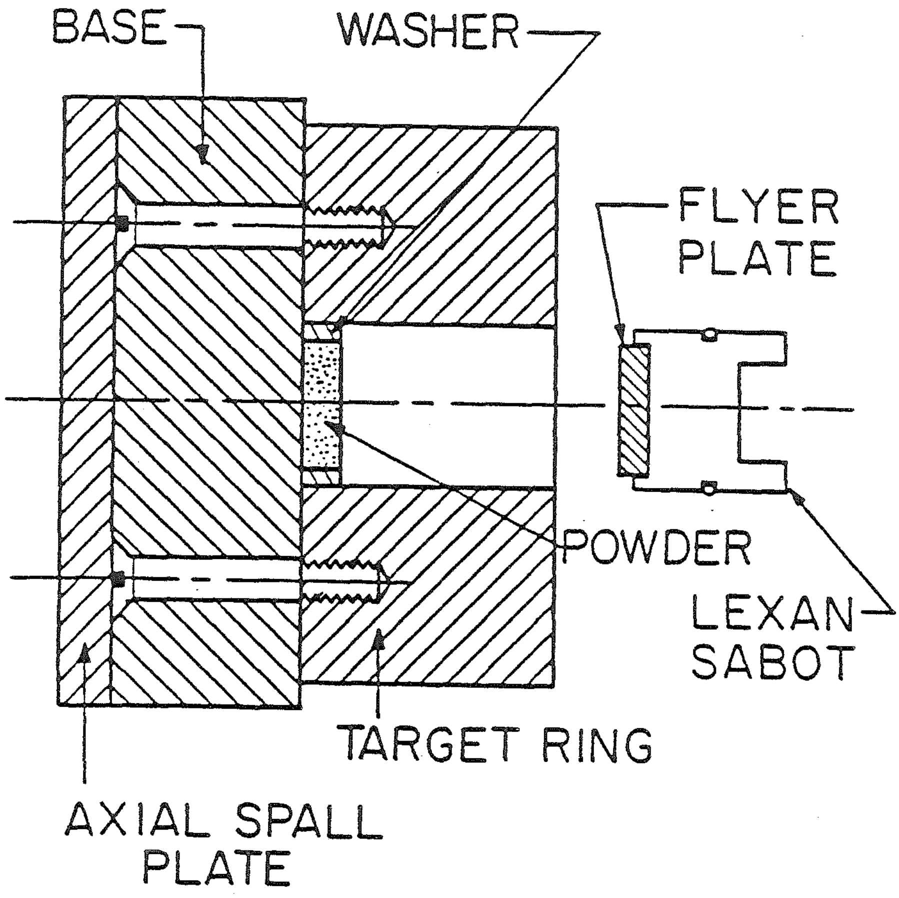

Fig. 3.2 Illustration of the hardened steel target ring used in the shock consolidation experiments of Markomet 1064.

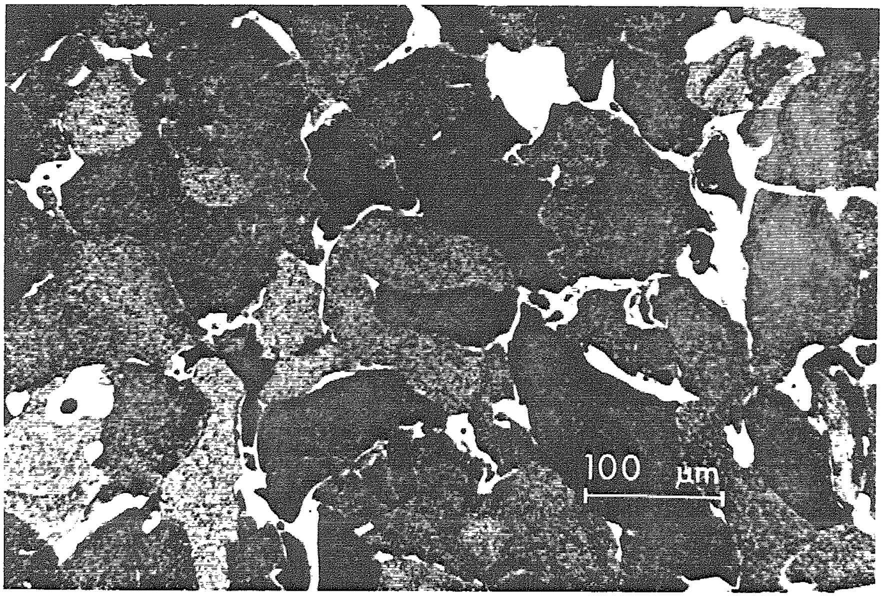

Fig. 3.3 Photograph of the polished and etched Markomet 1064 compact shot #808. Bright areas are amorphous, grey areas crystallized during the pre–shock anneal, and very dark areas in the bright areas crystallized upon rapid quenching during the shock consolidation.

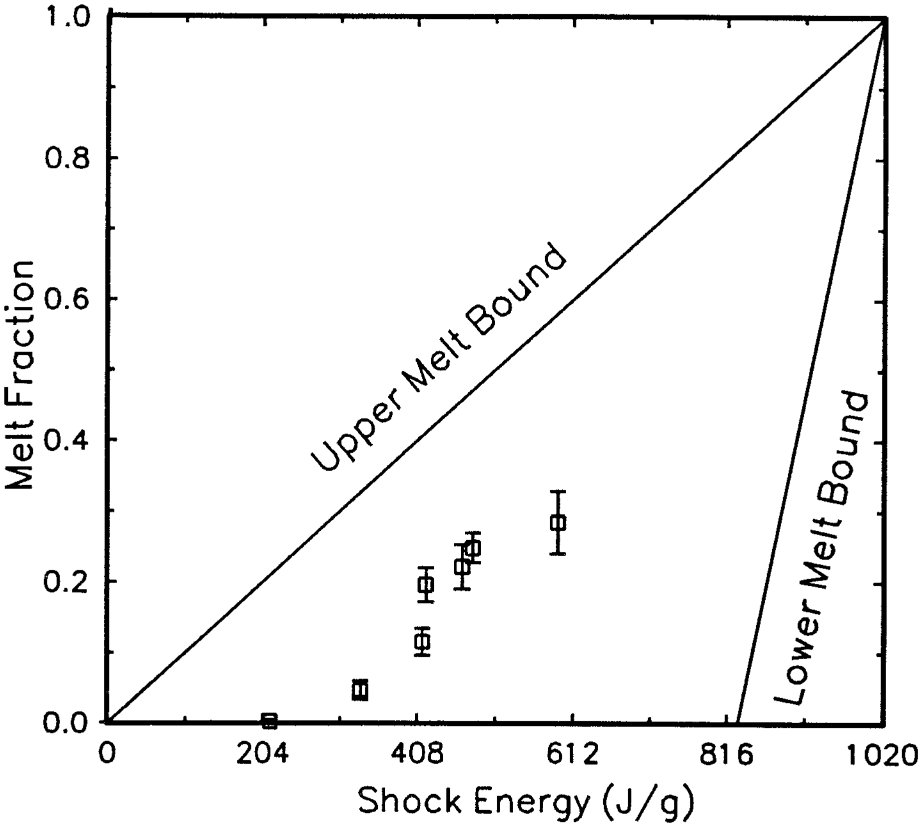

Fig. 3.4 Plot of calculated maximum, calculated minimum, and measured melt fraction vs. shock energy in the Markomet 1064 experiments.

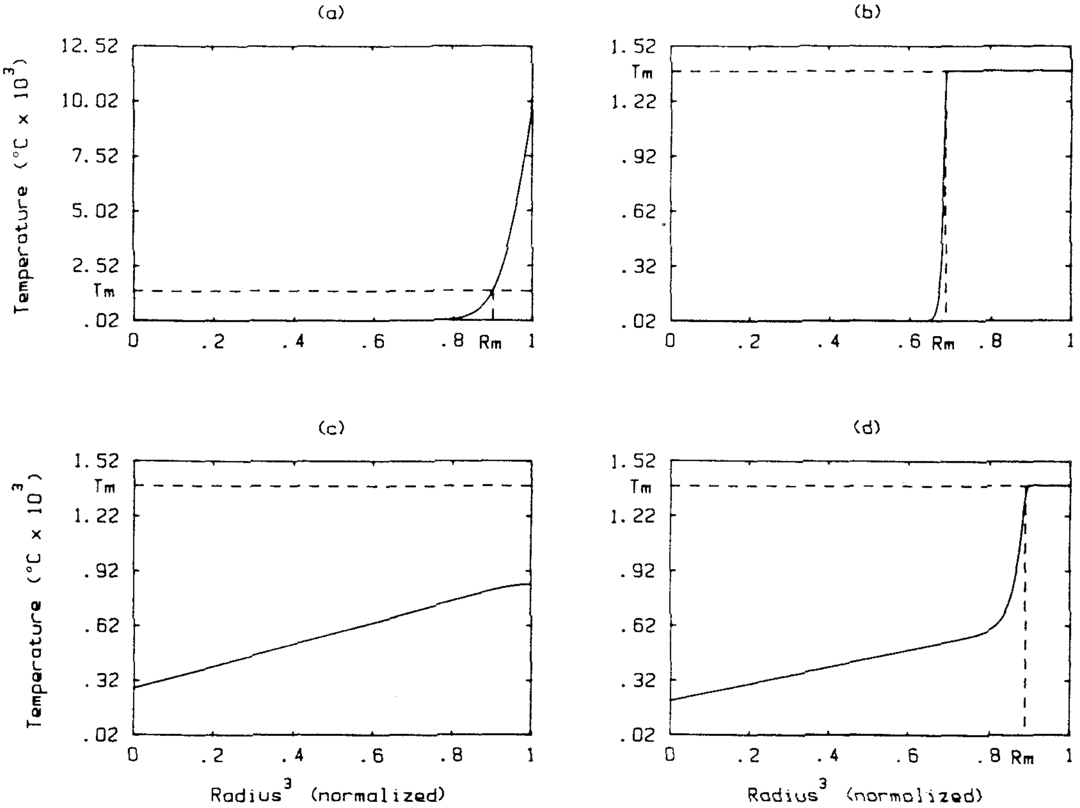

Fig. 3.5 Plot of temperature vs. cubed radius at the end of the shock rise time calculated using four different energy deposition profiles.

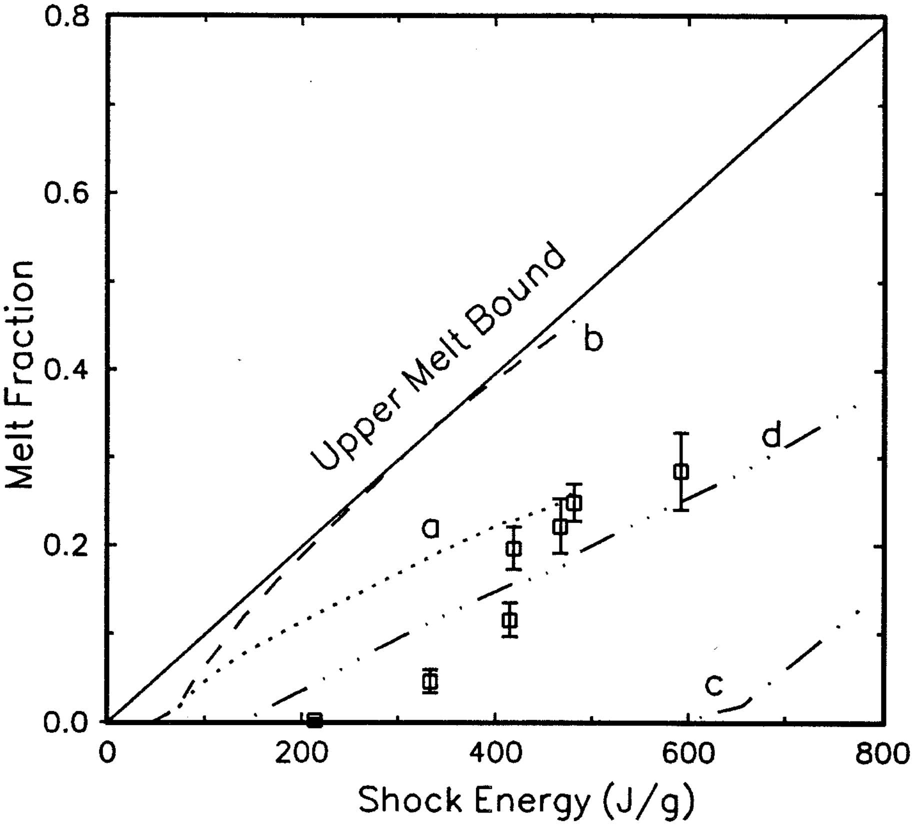

Fig. 3.6 Plot of predicted and experimental melt fraction vs. energy, using four energy deposition profiles. The profiles correspond to: a) All heat into sphere surface, b) All heat into solid–melt boundary (or surface if no melt), d) All heat into the sphere volume, and d) a mixture of 30% b) and 70% c).

References

1. D. Raybould, D. G. Morris, and G. A. Cooper, J. Mat. Sci. **14**, 2523 (1979).
2. D. G. Morris, J. Mat. Sci. **15**, 116 (1981).
3. P. Kasiraj, T. Vreeland Jr., R. B. Schwartz, and T. J. Ahrens, Acta Metall. **32**, 1235 (1984).
4. for example, J. E. Smugersky, in *Metallurgical Applications of Shock–Wave and High–Strain–Rate Phenomena*, edited by L. E. Murr, K. P. Staudhammer, and M. A. Meyers (Dekker, New York, 1986) p. 107.
5. G. B. Olsen and M. Cohen, Metall. Trans. **7A**, 1897 (1976).
6. for example, C. Koch, O. B. Cavin, C. G. McKamey and J. O. Scarbrough, Appl. Phys. Lett. **43**, 1017 (1983).
7. A. Ye. Yermakov, Ye. Ye. Yurchikov, and V. A. Barinov, Phys. Met. Metallogr. **52**, 50 (1981).
8. R. B. Schwarz and W. L. Johnson, ed., *Solid State Amorphization Transformations* (Elsevier, Lausanne, 1988).
9. T. Vreeland Jr., P. Kasiraj, and T. J. Ahrens, in *Mat. Res. Soc. Symp. Proc. Vol 28* (North Holland, New York, 1984) p. 139.
10. N. N. Thadhani, A. H. Mutz, P. Kasiraj, and T. Vreeland Jr., in *Metallurgical Applications of Shock–Wave and High–Strain–Rate Phenomena*, edited by L. E. Murr, K. P. Staudhammer, and M. A. Meyers (Dekker, New York, 1986), p. 247.
11. L. Brewer and A Lamoreaux, in *Molybdenum: Physics and Chemical Properties of its Compounds and Alloys* (Atomic Energy Review, Special Issue #7, 1981) p. 107.
12. T. J. Ahrens, D. Kostka, T. Vreeland Jr., R. B. Schwarz, and P. Kasiraj, in *Shock Waves in Condensed Matter*, edited by J. R. Asay, R. A. Graham, and G. K. Straub (Elsevier, New York, 1984) p. 443.
13. B. Crossland and J. D. Williams, Met. Reviews. **15**, 17 (1970).
14. W. H. Gourdin, J. Appl. Phys. **55**, 172 (1984).
15. W. D. Murray and F. Landis, Trans. of ASME. **81**, 106 (1959).
16. The areal diameter was determined by measuring the specific area of the powder. The major dimensions of several particles were measured from scanning electron micrographs.
17. L. Lowry, private communication based on differential thermal analysis and differential scanning calorimetry of Markomet 1064, Jet Propulsion Laboratory, Pasadena, California, 1985.
18. The latent heat of melting was estimated using Richard's rule. See D. R. Gaskell, *Introduction to Metallurgical Thermodynamics*, (McGraw–Hill, New York, 1981), p. 142. Measurements of the latent heat of melting were attempted, but gave inconsistent results.
19. Estimate based on measured electrical resistivity and behavior of Nichrome:

J. H. Lienhard, *A Heat Transfer Handbook* (Prentice–Hall, Edgewood Cliffs New Jersey, 1981) p. 492.

20. D. A. Young, *Phase Diagrams of the Elements* (Lawrence Livermore, Livermore, 1975).

21. A. B. Pippard, *The Elements of Classical Thermodynamics* (Cambridge, New York, 1964).

CHAPTER 4

SIZE DISTRIBUTION AND ENERGY DEPOSITION: POWDER THERMOCOUPLE EXPERIMENTS

4.1 Introduction

Strain energy localization during shock wave consolidation has been established by evidence of melted and frozen material near particle boundaries [1]. The extent of such localization can be inferred to some extent by measuring the quantity of refrozen material [2]. This type of 'recovery experiment' is productive using the materials which leave readily measurable evidence of rapid solidification but reveals little of the dynamics of the process. A more revealing look into the localization of shock energy requires real time measurement of temperature changes.

There are several constraints on such measurements. First, the characteristic response time of the technique to be employed must be considerably smaller than the shock–wave rise time in a porous medium. As established by Schwarz et al. [3], the rise time of a shock wave, t_{rise},in a porous medium is roughly the particle diameter, D, divided by the shock wave velocity, V_s. For a 6 GPa shock wave in 64μm diameter copper at an initial porosity of 40%, the shock wave velocity is 1.6 km/s, and the rise time is about 40 ns. Second, the measurement must be made without excessively perturbing the shock process itself, and in a region of the sample where the shock state is simple and well–characterized. The optopyrometric measurement of temperature at a powder–window interface, for example, adds powder–window shock interactions to the problem. (It may nonetheless be a highly successful technique for measuring bulk shock effects; continuum effects are well understood, and corrections for the window impedance can be made. This technique was used to determine the effect of pressure on the melting point of iron [4]).

These criteria may be met utilizing the thermoelectric (or Seebeck) effect. Electric potential is generated by a thermal gradient in a conductor. For my purposes, the conductors are metals with electrons as the charge carriers. Roughly speaking, higher temperature metal has higher velocity electrons. They tend to diffuse more readily than the lower velocity electrons in the colder region. This creates a net excess charge in the colder region, and a positive voltage from hot to cold ends of the conductor. More accurately, a higher temperature results in a larger number of electrons occupying energy states above the Fermi level in the metal. These slightly more energetic electrons have a higher mean velocity and their higher mobility creates a net electron current (or net voltage gradient, if the circuit is open). The effect is monotonic and roughly linear over a wide temperature range in many metals. Dissimilar metals generally have different thermoelectric behavior. If two metals with different thermoelectric coefficients are joined, the temperature at the junction may be determined by measuring the electric potential (or EMF) across the ends of the wires, provided the temperature of the ends (the 'reference temperature') is known. A more complete discussion of the thermoelectric effect may be found in *Solid State Physics*, by Ashcroft and Merman [5]. These 'thermocouples', fabricated from standardized alloy pairs such as platinum/platinum with 10% rhodium, and copper/copper with 45% nickel (constantan) are commonly employed to measure temperature.

Embedding a conventional thermocouple in a powder would create impedance mismatches and other problems limiting the validity of the data during the rise time. If, however, the thermocouple is formed by the powder itself, this problem is avoided. More specifically, two powders of very similar shock impedance but different thermoelectric strength are layered parallel to the shock front. The EMF generated by this powder–powder thermocouple is recorded. Copper and constantan were used in these experiments. The effect of varying particle size distribution on thermoelectric output was explored using this technique.

Experiments measuring shock–generated EMF were first made in 1959 by Jacquesson [6]. Thermocouples were imbedded into the material of interest, and EMF recorded. The difficulty lies in the extreme locality of the particle–particle interactions. The shock impedance and thermal response of the powder differed considerably from that of the thermocouple In addition, a host of anomalous voltages can be generated via friction between thermocouple elements, triboelectric effects, and electrical impedance problems. In spite of these difficulties, Bloomquist et al. successfully used a diffusion bonded thermocouple pair imbedded in a shocked media. This resulted in accurate equilibrium temperature measurements as predicted by Hugoniot calculations [7]. Nesterenko first demonstrated that the shocked powders themselves could form the thermocouple [8]. Schwarz et al. used copper and constantan powders to form the thermocouples, and measured the rise–time of the shock wave to be similar to the time required for a shock wave to traverse a single particle [3].

4.2 Thermocouple Experiment Design

Since the object of this work was to explore the effect of size on energy distribution, powder size and shape uniformity was of primary importance. Characterizing the behavior of an irregular powder would be more difficult, since several spatial measurements of the powder would be necessary, so a nearly spherical powder was sought. Truly mono sized spherical powder would be ideal, but powder fabrication processes rarely achieve this ideal. (Polymeric sphere standards are produced, and the carbonyl process can produce highly spherical metal powders.)

Given the required thermocouple alloy compositions, we elected to procure inert–gas atomized copper and constantan powders from Ames Laboratory in Ames, Iowa, and HJE Corporation in Troy, NY, respectively. The copper powder was atomized from pure copper (CDA101), and delivered sieved into size fractions. The constantan was atomized from thermocouple stock ingot from Omega Engineering, Inc. of Stamford, CT. The constantan exhibited poor electrical conductivity, as received, and was treated in wet hydrogen at 400° C for 2 hrs to reduce surface oxides. The constantan powders were sieved using a mechanical sieve shaker and bronze mesh screens into size fractions from 37–44 μm, 44–53μm, etc. Photographs of the powders are presented in Fig. 4.1.

The next step was designing a thermocouple target fixture and loading protocol which would insulate and shield the thermocouple circuit, and allow the thermocouple to be built. By fabricating the target out of copper, thermoelectric potential difference between the target and the copper powder were avoided. This was confirmed in the shock experiments; no EMF was measured as the shock wave traversed the copper plate–copper powder interface. The target consists of a circular plate counterbored to fit onto the barrel extension at the end of the gun muzzle (see Chapter 2), with a short copper tube soldered onto the flat side of the disc. A quartz sleeve is slipped into the copper cylinder, providing electrical isolation within the cylinder. See Fig. 4.2.

First, the copper powder was loaded to a depth of one mm, and leveled with a depth micrometer. Next, an annular disk of ceramic felt was placed onto the copper. The ceramic (Cotronics Corp. Brooklyn, NY) limits the thermocouple contact to the center 5 mm of the disk. The shock wave is planar in this region of the powder; edge interactions originating at the flyer plate edge remain outside the center. The periphery of the disk is covered with 44μm alumina powder to insure insulation at the edge. Three mm of constantan powder is next loaded into the target. The constantan is also leveled. Several mm of irregular copper powder is placed on the constantan to provide an easily compressible contact layer. The porous bronze cap is pressed onto the copper, and epoxied to the quartz sleeve under several hundred pounds of pressure. (The load is increased until the thermocouple resistance is less than one Ω.) See Fig. 4.3. EMF is measured between the bronze plug and the copper cylinder.

The copper sleeve provides enough support to allow light compression of the powder without fracturing the quartz. Since retention of the initial powder shape was desired, I wanted to avoid pressing the green compact strongly. This meant some amount of static compression had to be maintained on the compact to retain a low resistance through the powder junction. The epoxy bond between the bronze plug and the quartz, cured under load, provided this compression.

The electrical circuit had to combine high input impedance and low inductance, to deliver true thermoelectric potential values with nanosecond response time. Initially the thermocouple circuit was simply connected via an RG58 BNC cable to the 50Ω termination of a Tektronix 11302 oscilloscope. The inductance of the BNC cable, combined with the low impedance, pulled the signal down to zero after a few unrevealing oscillations. A high speed op–amp video buffer–follower (National Semiconductor LH0063CK) was used to construct a robust voltage follower capable of supplying the oscilloscope with an accurate signal. A short length of micro–coax cable connected the thermocouple to the voltage follower. This circuit was tested with a 500 MHz triangle wave for frequency response and gain accuracy. The signal was recorded and digitized using a CCD camera attached to the microchannel plate display screen of the oscilloscope.

To trigger the oscilloscope at the proper time, an enameled 0.1 mm dia.

copper wire was glued across the impact face of the copper target plate. The wire was kept at a 750 mV potential, and was broken or shorted to ground by the impact of the flyer plate. The output of the wire was connected to the oscilloscope trigger with a 50Ω termination.

The thermocouple targets were placed on the barrel extension, supported by an aluminum ring against the momentum trap. The aluminum ring also served as a debris containment, and a connector mount for the trigger wire. A 25mm dia. 303 SS flyer plate, mounted on a 35mm nylon sabot, was accelerated down the evacuated barrel into the thermocouple target plate. The shock wave generated by the impact was transmitted through the copper plate and into the powder thermocouple. The targets were, of course, each destroyed by the experiment.

4.3 Experimental Results

The intent of these experiments was to elucidate the degree of energy segregation in a powder mixture as powders of different size are shock–consolidated. If a sizable portion of the powder melts upon impact, the details of the rise time and initial temperature decay are lost in the temperature plateau created at the melting point. The velocities employed were chosen at a level generally inadequate for full interparticle bonding (though sufficient for full densification). The first experiment, with a flyer velocity of 872 m/s, resulted in a 100 ns voltage plateau at 75±2 mV. See Fig. 4.4. The uncertainty is a result of a non–steady zero–level and 8–bit data range. This should correspond to the EMF generated by the copper–constantan couple at the melting point of copper under a pressure of 5.3 GPa, assuming material is not heated beyond its melting point during shock consolidation. (This assumption was discussed in Chapter 3.) At 5.3 GPa, copper melting point is elevated to 1260° C based on interpolation of the results of Akella [9].

Thermocouple calibration was based on data published by Bartels et al. [10], and linearized to 6.5 μV/° C; the data is not quite linear, but the interest here is in the dynamic response rather than the exact temperature value. See Fig. 4.5. 75 mV corresponds to a temperature of 1175° C, without correcting thermoelectric EMF for pressure. Since the thermoelectric signal is an average of the EMF at all points on the copper–constantan interface, a voltage plateau below that corresponding to the melt temperature can still indicate the presence of some liquid.

The thermocouple shots are summarized in Table 4.1. A range of powder size combinations and energies was explored. The digitized traces are displayed in Fig.'s 4 and 6–10. An example of the raw data (captured from the CCD camera) is shown in Fig. 4.11.

4.4 Discussion and Analysis

The analysis of this data (for elucidating the energy deposition in the powders as a function of particle size) requires analysis of the signal during the rise time and subsequent decay during the characteristic temperature relaxation time of the particles involved. Several effects interact to create the output shape. Copper and constantan spheres are in contact, thermally and electrically conducting, and mutually deforming as the shock wave consolidates and heats the powder particles. The thermocouple interface is composed of 25 mm^2 of powder particles in contact. The interface is flat in only the roughest sense; it is approximately parallel to the shock plane. Irregularities characteristic of at least the radius of the larger particles are expected. In addition, a certain amount of mixing is possible, especially when large and small particles are combined. Some amount of average tilt is expected too, though efforts were made to control tilt to within a few degrees.

A realistic simulation of the above phenomena would require a three–dimensional finite element analysis of daunting size. More limiting is the absence of a tested model for material deformation at strain rates over $10^7/s$. This work is limited to an examination of the thermal deposition and conduction which occurs during the shock wave passage. The heat conduction equation,

$$\frac{dT}{dt} = -k\nabla^2 T \tag{4.1}$$

was applied during and after the passage of an energy input front representing the shock wave. Solid density was assumed throughout. Even this problem becomes daunting when the lack of a symmetry direction, change in thermal properties, and melting of particle surfaces are included. Further simplifications render the problem tractable, although the conclusions are necessarily somewhat qualitative as a result.

The simplest dynamic representation of a particle heated preferentially on the outside consists of two thermal masses, the particle core and crust, connected by a thermal resistance giving the system the relaxation time characteristic of a sphere. The core, or inner mass, is an inner sphere concentric with the particle. The crust, or shell, is the remaining hollow sphere formed by subtracting the core from the original particle. Next, the ratio of the shell mass to the core mass, defines the relative sizes of these thermal elements. For the moment, allow the sphere no melting point. If many such spheres are in contact (allow them to flatten to contact one another), then the crusts will conduct to one another while the cores each conduct to only their respective crust. Note there is no net heat conduction parallel to the shock plane; simplify the picture by reducing the model to a line of particles like a string of pearls along the shock direction. Connect them thermally as before. Now 'blur' them (convolve them spatially by at least one particle diameter) to allow for random stacking of the many particles near the interface and the roughness of junction itself. The 'blurring' removes the periodic oscillation of temperature created by the discrete particles, but still allows a net heat flow across the interface. The 'blurred' string can be simulated with relative ease.

The junction was modeled as a one–dimensional string of thermal masses conducting heat to one another and each to a single internal thermal mass. See Fig. 4.12a. The continuum differential equations for this system (not at the junction) are:

4.2) $$\frac{dTo}{dt} = -k\frac{d^2To}{dx^2} + l(Ti-To)$$

4.3) $$\frac{dTi}{dt} = m(To-Ti)$$

with To the particle shell temperature, Ti the particle interior temperature, and k, l, and m the thermal diffusion coefficients linking them. This system of equations is not analytically simple when the coefficients change abruptly and the particle shells start to melt.

The thermal properties change at the junction between copper and constantan. This may be thought of as representing a continuous copper wire butted to a constantan wire. The wire has a core which conducts only radially. The shock wave is reduced to a heat wave traveling at the shock velocity down the wire, depositing energy mainly into the outer wire, as a shock wave deposits energy mainly into the outside of a particle See Fig. 4.12b. In addition, the heat wave can be perturbed to deposit energy preferentially into either of the materials near the junction. Average energy deposition is unchanged.

The final step is to allow for partial melting of the particle crust. The crust here has a mass of half the entire particle. A simple energy sink was chosen to represent the melting transition; at each node a record of melted material is kept. If a node temperature would exceed the melting temperature, the energy is placed into this record. Upon cooling subsequent to shock wave passage, the energy is conducted out of the melted material before any solid is cooled. The simulation stops if any particle crust is entirely melted.

As the simulation runs, the junction temperature is recorded. Following the end of the run, the resulting temperature history of the junction is convolved with a spreading function to simulate the tilt and roughness of the powder junction. The tilt of the junction is represented by a square wave convolution. Mixing is represented by a triangle wave convolution. This system was simulated and run on a PC–compatible computer. The model code, written in Microsoft QuickBasic, is listed in Appendix B.

Averaged thermodynamic values of thermal conductivity, diffusivity, and density are listed in Table 4.2. The melting point of copper was corrected for pressure. The melting point of constantan was fixed to match that of copper. The parameters which can be varied in the model are:

A) the percentages of shock energy into the crust and core of the elements,

B) the relative masses of the crust and core,

C) the degree to which energy is preferentially deposited into the copper and constantan near the powder junction, and

D) the width of the convolution of the thermocouple output with a triangle function representing junction roughness.

These parameters allow sufficient freedom to fit almost any likely thermoelectric output. Varying all of them to achieve a best fit in each case is **not** the intent of this study. Rather, a reasonable determination of each parameter from the collective behavior of the experiments was attempted as follows.

Given the similarity of the experiments carried out, the gross character of the energy deposition was not expected to change. Thus parameters A) and B) were held fixed for all of the simulations. Using the duration of the voltage plateau in shot #77 (Fig. 4.4), and the shock energy required to melt material to form such a plateau as guides, parameters A) and B) were set at 70:30 and 1:2 respectively. If more energy is input into the particle core, material will not melt to form the voltage plateau. If the particle crust is more massive, melting is similarly suppressed.

In each shot, a somewhat different degree of thermocouple planarity existed. The mixing of copper and constantan particles was enhanced when the size difference was very large; small particles fell into the interstices between large particles. Tilting of the thermocouple junction relative to the shock plane varied slightly in each experiment. These effects directly influence the width and shape of the initial voltage rise of the thermocouple signal. In each experiment, parameter D) was determined by fitting this portion of the thermocouple signal. Note that the effect of thermal relaxation during the rise time (approximately 100 ns) is minimal; given a thermal diffusivity of 1 cm^2/s, the characteristic thermal distance is 3 μm.

Finally, parameter C), the shock energy distribution near the thermocouple junction, was varied as shown in Fig. 4.13. The shape of the initial voltage decay from maximum is sensitive to this variable. The energy is biased into the copper or constantan with the saw tooth profile since this conserves average energy as demanded by the Hugoniot. This is the major parameter of interest in this study of the effect of particle size distribution on energy deposition. Parameter C) was varied to provide the best fit, especially to the initial decay slope from the voltage maximum; the accuracy of the absolute value of the maximum voltage is expected to suffer somewhat from the lack of temperature–varying thermodynamic parameters. The model output is displayed with the data in Fig. 4.4, and 4.6–4.10. In Fig. 4.10, note the result of varying parameter C) on the output.

As illustrated by this model, particle size strongly influences energy distribution. The fine powder, copper or constantan, is consistently heated in favor of the larger powder. In the first thermocouple experiment, shot #77, the wider distribution of constantan powder size (and smaller minimum size) results in more energy deposited into the constantan. The effect is not as great as in the more extreme size disparities of shots #108 and #109. Secondarily to particle size, hardness influences energy deposition. The energy bias into the copper for best fit in shot #91 (Mext = 1.0) is larger than the bias into the constantan in shot #109 (Mext = –0.5), though the ratio of sizes is similar; the copper to constantan ratio in shot #91 was 5:9, and in shot #109 was 10:4.

The simulation provides a poor prediction of system behavior when the particle sizes differ by much more than a factor of 2. The behavior of shot #108, with a size ratio of 1:3, was not well predicted. This may be attributed to a high degree of particle intermixing at the interface, which would reduce porosity and total energy deposited near the interface.

The thermocouple simulations of shots #80 and #109 provide somewhat contradictory results; though particle sizes are similar, energy in shot #80 appears to be biased towards the larger copper particles (Mext = 0.25), while in shot #91 energy appear to be preferentially deposited into the constantan (Mext = –0.5). A certain degree of melting in shot #80 (E = 210 J/g) may be masking the detail in shot #80, causing an anomalously slow decay from maximum slope. A voltage plateau in shot #108 (E = 215 J/g) was observed. It would be interesting to repeat several of these experiments at somewhat lower shock energies.

4.5 Conclusions

These experiments have demonstrated (albeit qualitatively) the preferential deposition of energy in small particles in contact with larger powder particles during the shock wave consolidation process. In addition, and to a lesser degree in the hardness range tested, softer particles absorb energy preferentially to harder particles.

The energy deposition process during shock wave consolidation of spherical particles has been modeled with a one–dimensional simulation including preferential energy deposition at particle surfaces, preferential energy deposition into smaller particles, conduction into particle interiors, conduction between particles, and incomplete melting and freezing of particle shells.

Table 4.1. Powder thermocouple experiments summary.

Shot	Cu Size (μm)	Const. Size (μm)	Flyer Vel. (m/s)	Shock Press. (GPa)	Equil. Temp. (°C)	Maximum EMF (mV)	Rise Time (ns)
77	74–88	53–106	872	5.3	680	75	40
80	90–106	53–63	788	5.0	550	59	90
91	44–53	74–106	826	5.5	590	53	110
92	63–74	63–74	818	5.4	580	68	37
106	18–38	74–106	260	0.7	90	5	130
108	18–38	74–106	799	5.2	545	60	90
109	90–106	37–44	726	4.4	470	60	95

Table 4.2. Copper and constantan thermodynamic data used in model.

Property		Copper		Constantan
Density	g/cm^3	8.9		8.9
Thermal Conductivity	W/m–s–K	385		35
Thermal Diffusivity	cm^2/s	1.11		0.101
Thermoelectric Power	μV/°C		6.5	
Melt Temp. at 1 Bar	°C	1083		1083
dTm/dP	°C/kBar	3.36		3.36
Latent Heat of Fusion	J/g	205		205

Table 4.3. Powder thermocouple modeling parameters. Powder sizes, shot energy, and melting point are measured or calculated. The concentration of shock energy in outer vs. inner portions of particles, and relative mass of shell to core of particles are fixed for all cases. Energy bias near junction to copper, tilt convolution width, and mix convolution width are fit to each case.

Shot	Cu Dia. (μm)	Con. Dia. (μm)	Etot J/g	Melt Temp °C	Eext over Eint	Mext over Mint	Ebias to Cu @junc	Tilt Width (μm)	Mix Width (μm)
77	80	80	260	1280	0.7	0.5	–0.25	0	40
80	98	58	210	1250	0.7	0.5	+0.25	37	25
91	50	90	230	1250	0.7	0.5	+1.0	50	12
106	28	90	29	1100	0.7	0.5	+0.5	14	14
108	28	90	215	1250	0.7	0.5	+0.25	0	42
109	98	40	185	1250	0.7	0.5	–0.5	25	25

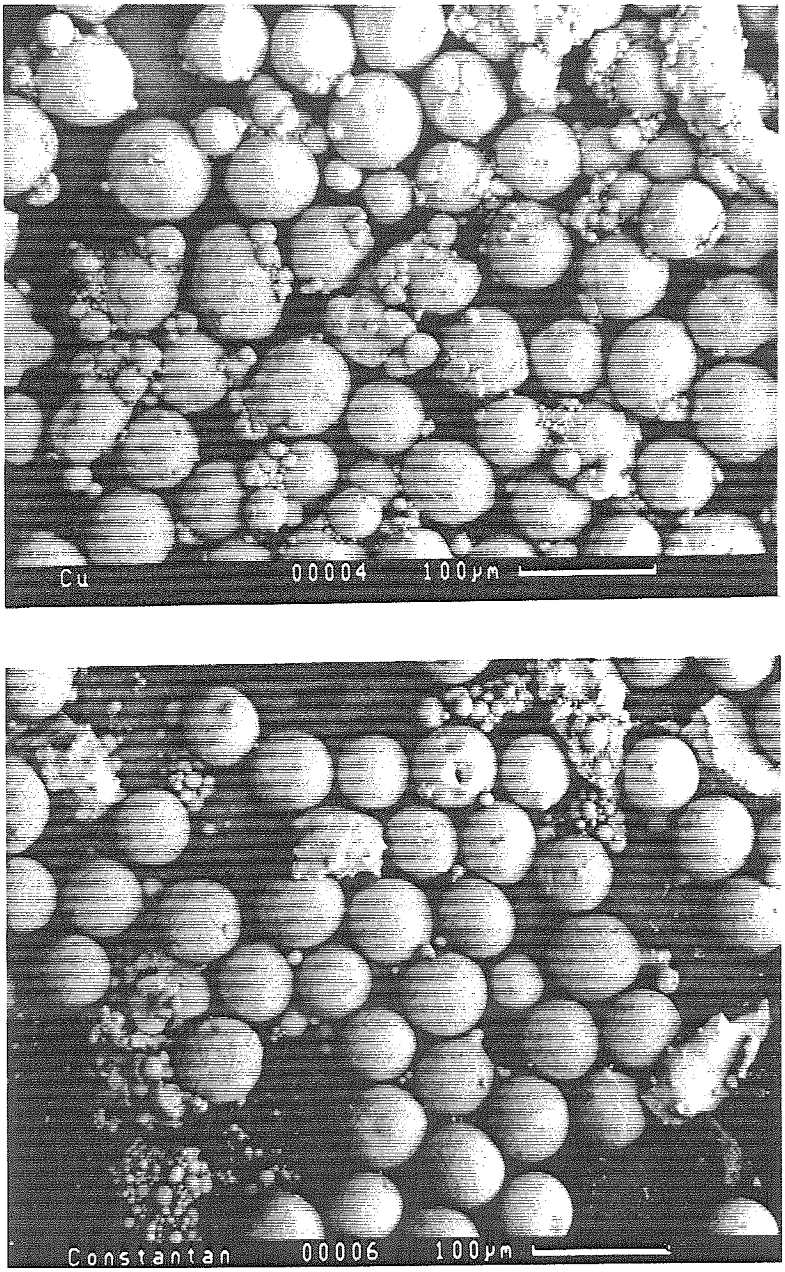

Fig. 4.1 Photographs of the copper and constantan powders, sieved to 63–74μm.

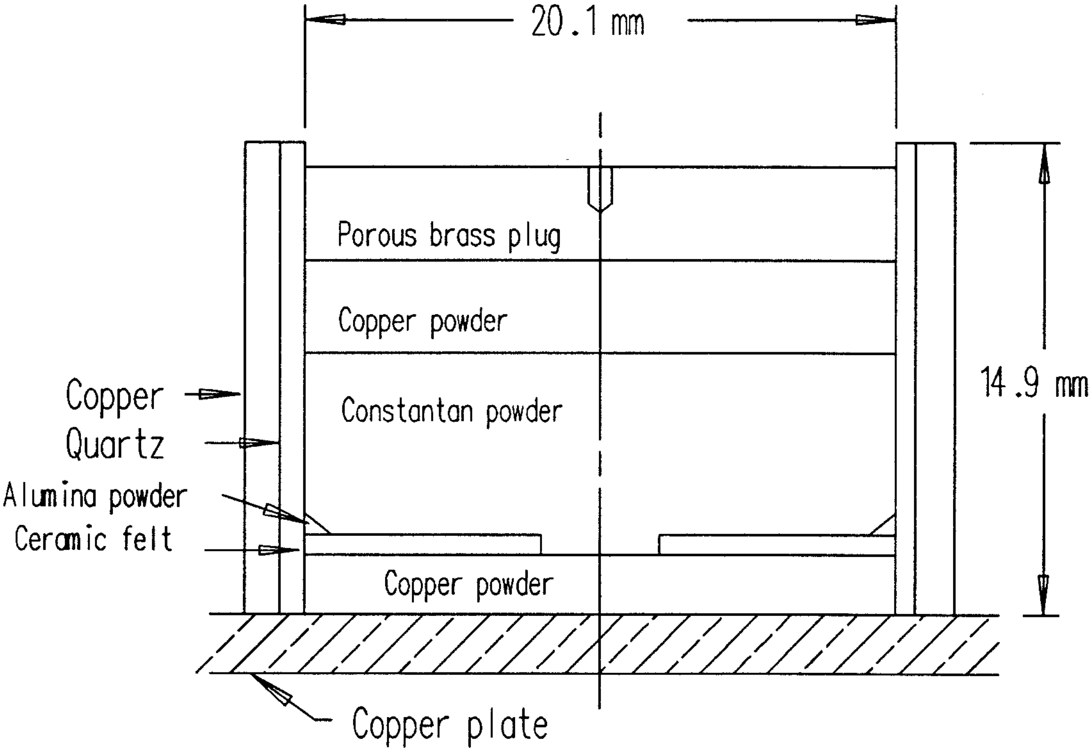

Fig. 4.2 Illustration of the thermocouple target, showing the powder layers.

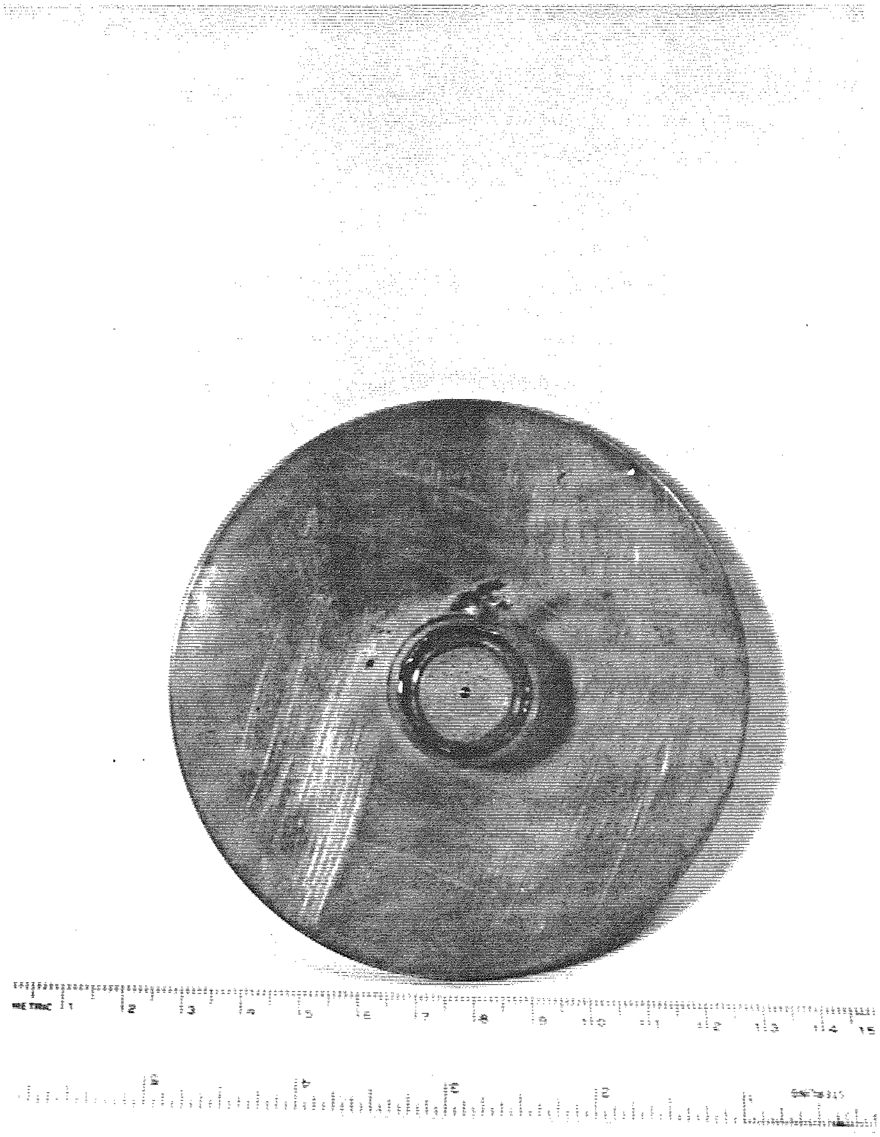

Fig. 4.3 Photograph of the thermocouple target, assembled with a hole in the bronze plug for the signal output wire.

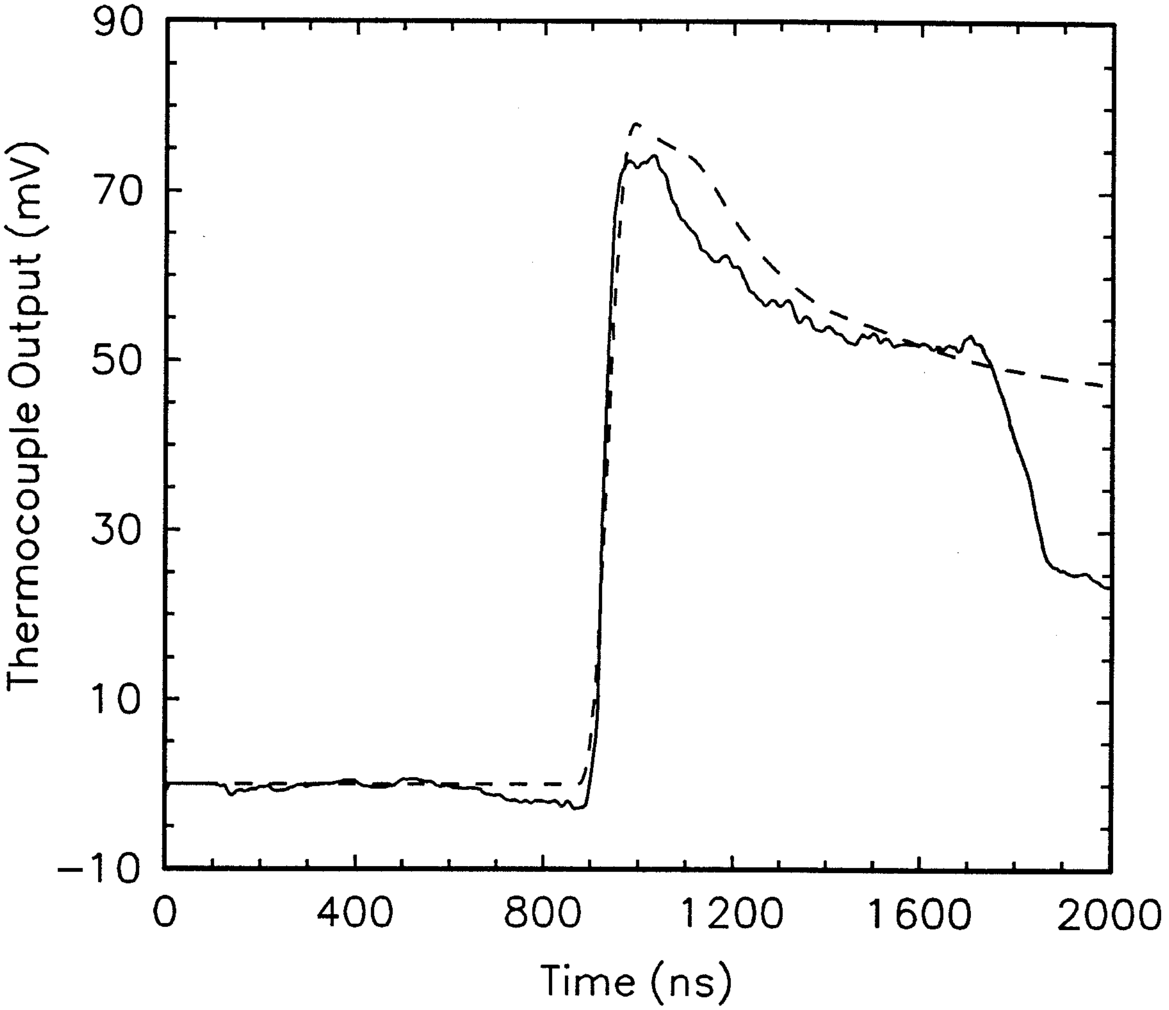

Fig. 4.4 Plot of thermocouple voltage vs. time, from shot #77, and the result of the thermocouple simulation program with parameters listed in Table 4.3. The voltage drop at 1700 ns corresponds to the shock wave arrival at the second copper powder layer; the constantan layer was 1.75 mm thick. (See Fig. 4.2).

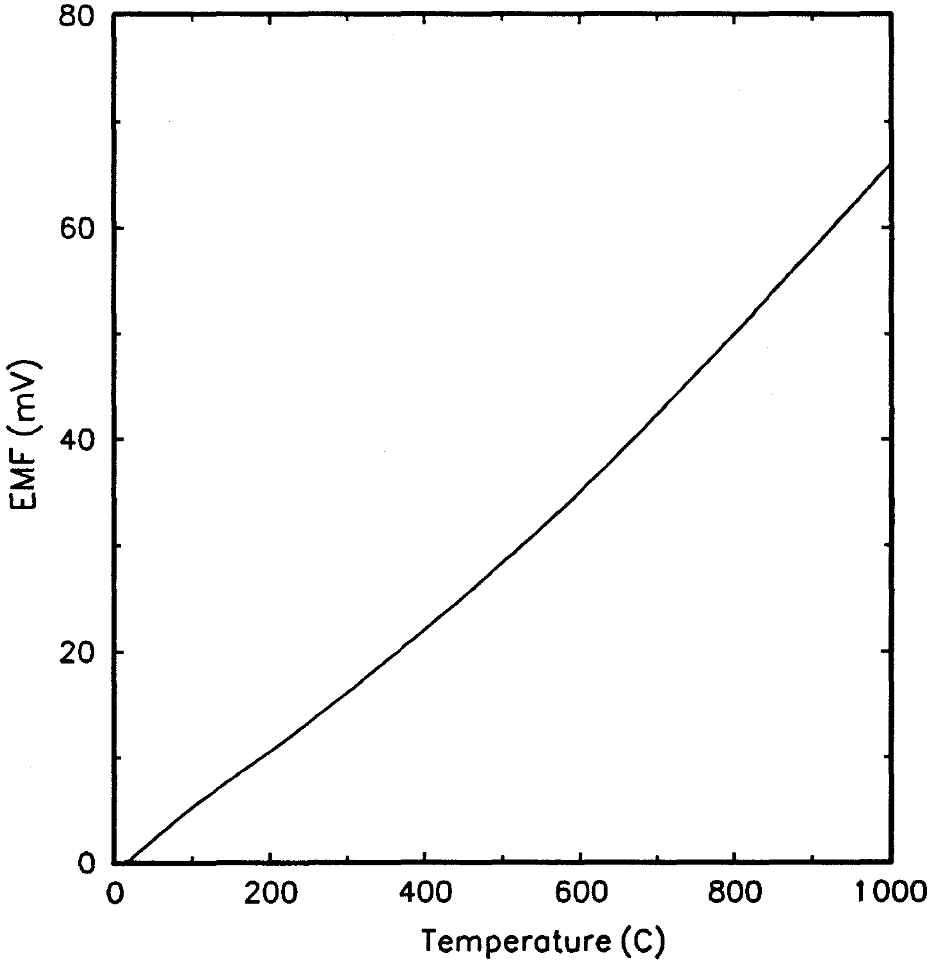

Fig. 4.5 Plot of EMF vs. temperature for a copper–constantan thermocouple with a 20° C reference temperature, from data published by Bartels et al. [10].

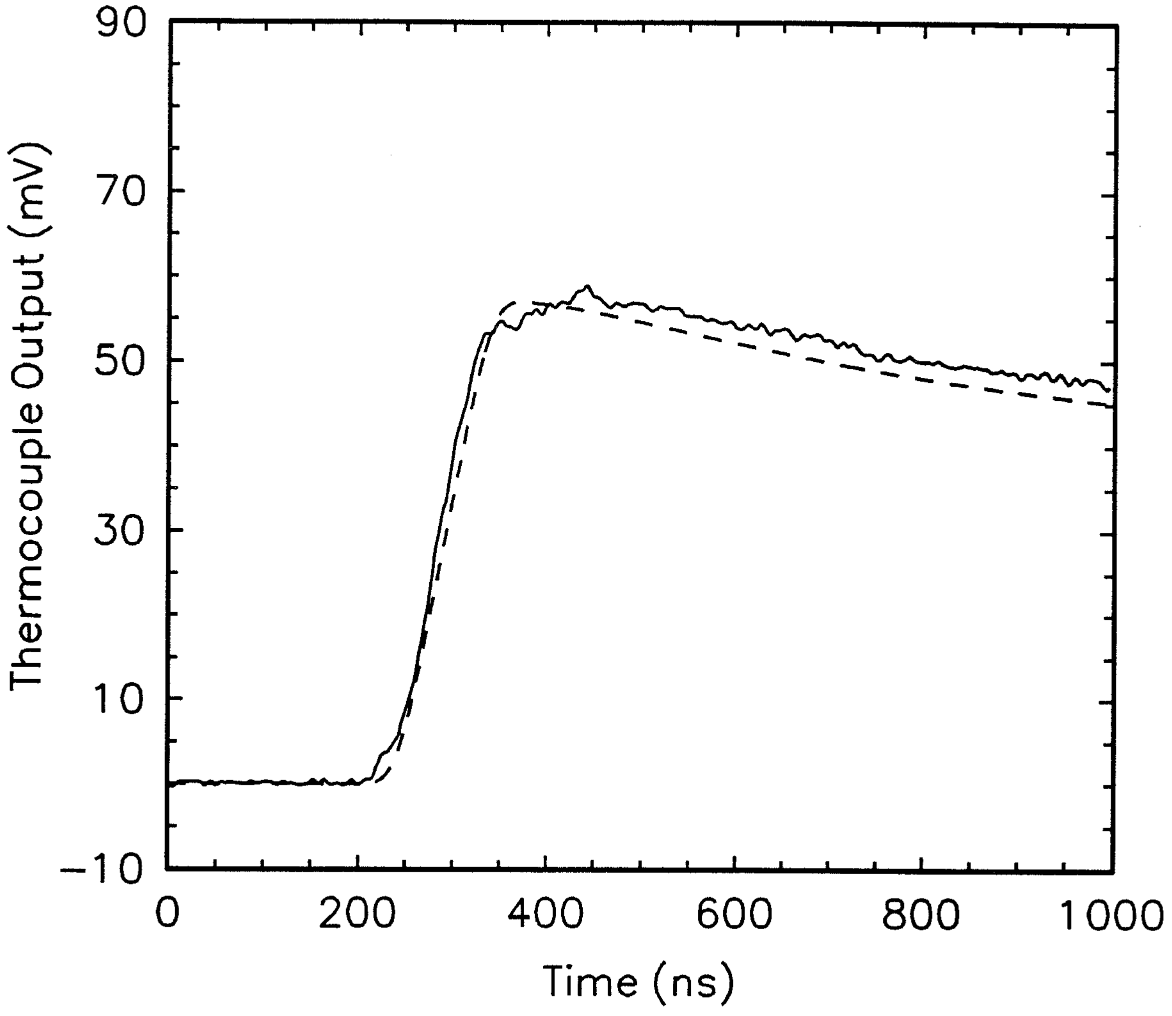

Fig. 4.6 Plot of thermocouple voltage vs. time, from shot #80, and the result of the thermocouple simulation program with parameters listed in Table 4.3.

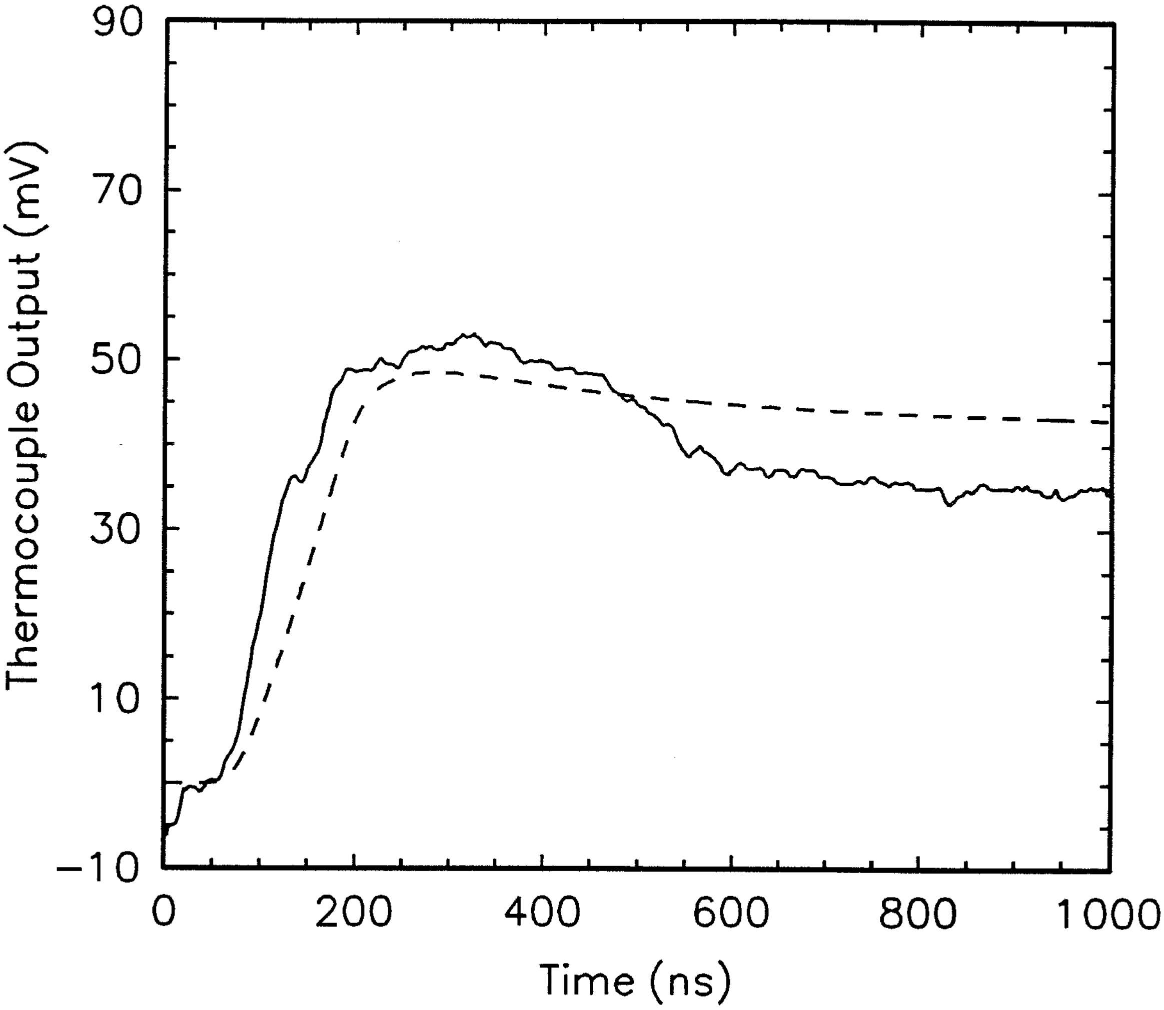

Fig. 4.7 Plot of thermocouple voltage vs. time, from shot #91, and the result of the thermocouple simulation program with parameters listed in Table 4.3.

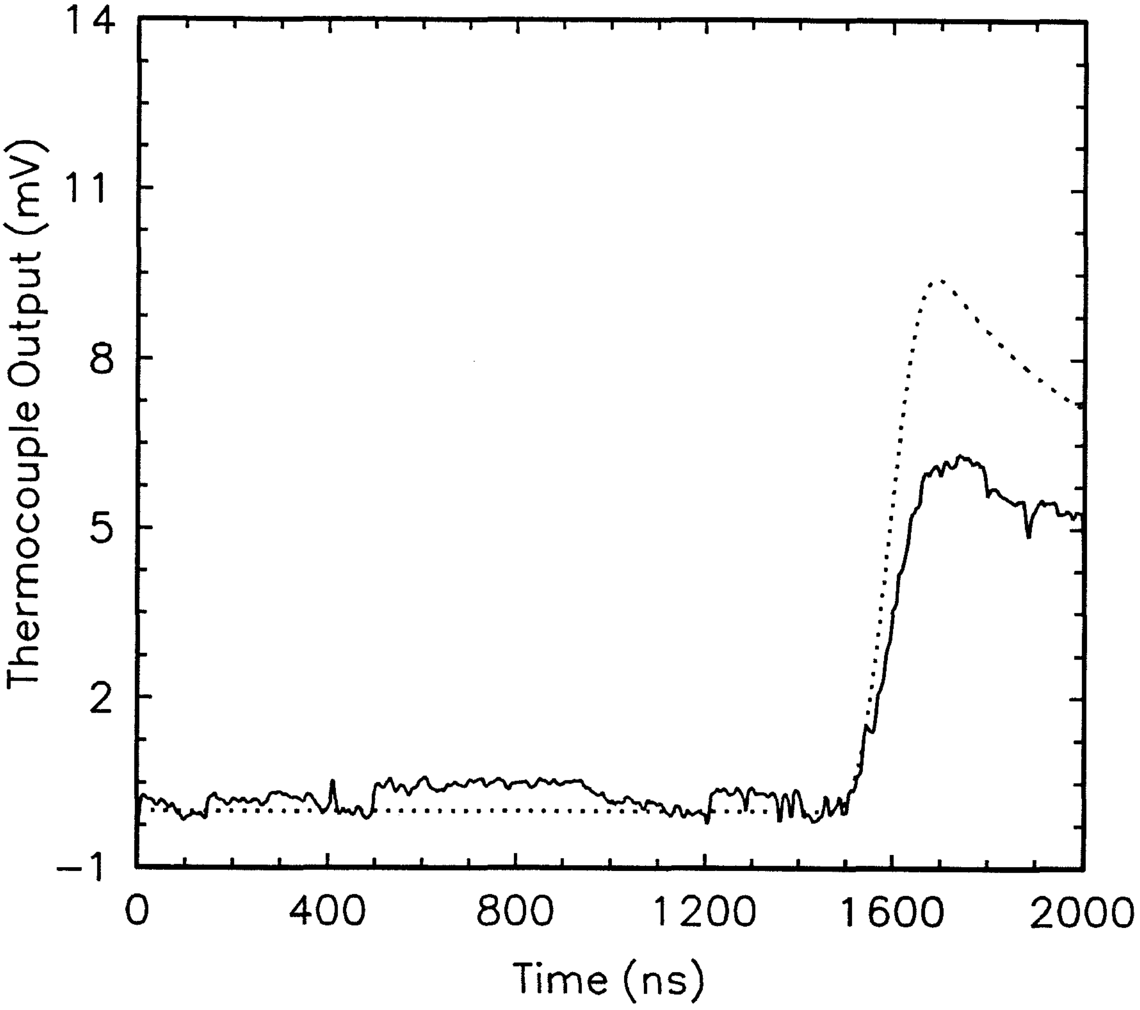

Fig. 4.8 Plot of thermocouple voltage vs. time, from shot #106, and the result of the thermocouple simulation program with parameters listed in Table 4.3.

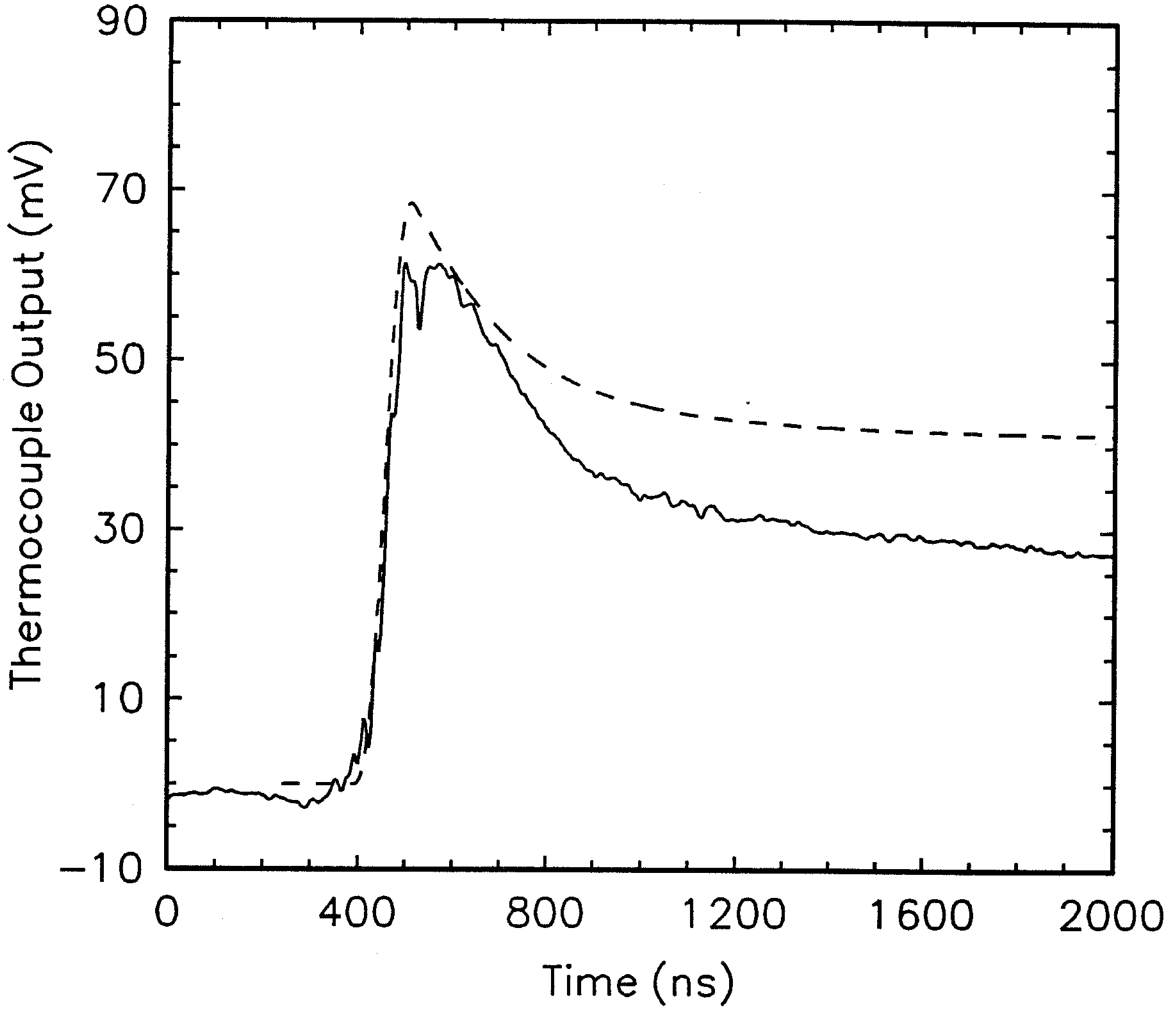

Fig. 4.9 Plot of thermocouple voltage vs. time, from shot #108, and the result of the thermocouple simulation program with parameters listed in Table 4.3.

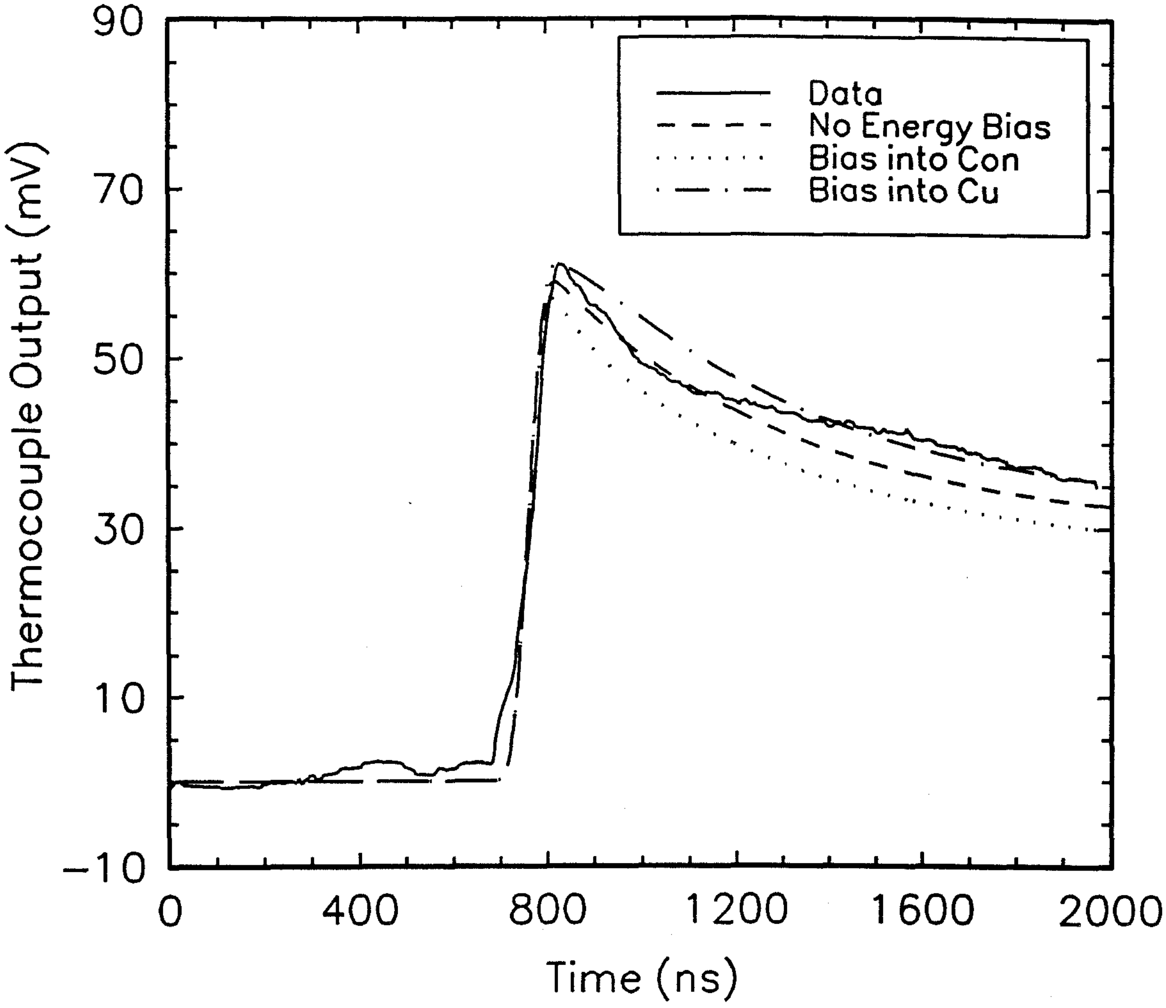

Fig. 4.10 Plot of thermocouple voltage vs. time, from shot #109, and the result of the thermocouple simulation program with parameters listed in Table 4.3 (labeled Bias into Con). In addition, the results of the simulation assuming no energy bias and energy bias into copper are shown.

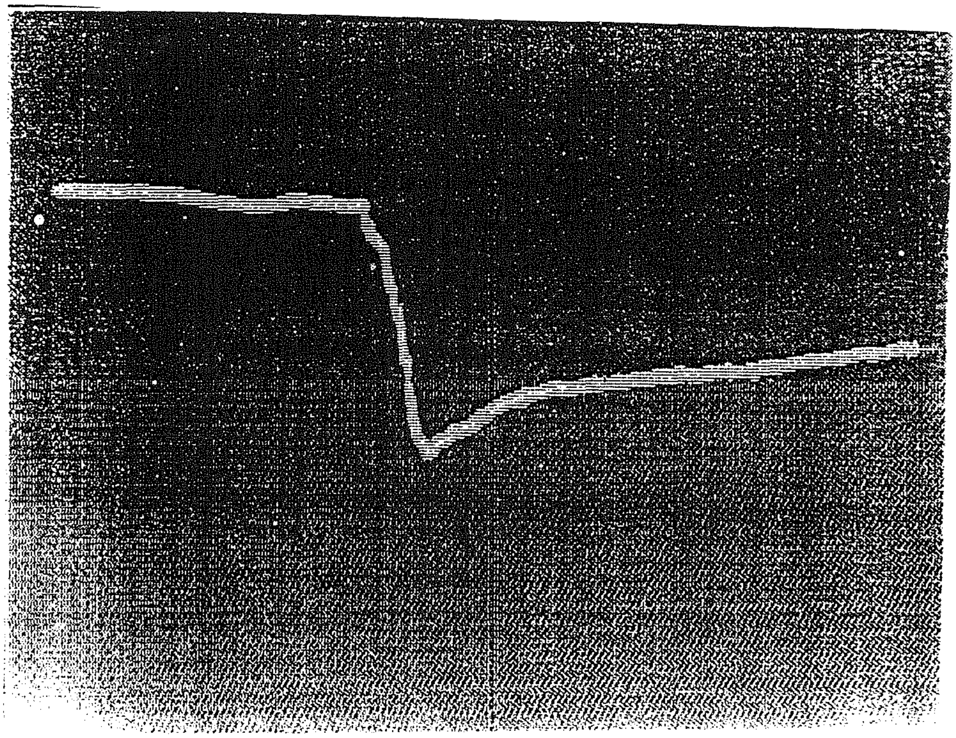

Fig. 4.11 CCD camera image of thermocouple voltage vs. time from shot #109, with thermocouple voltage direction negative.

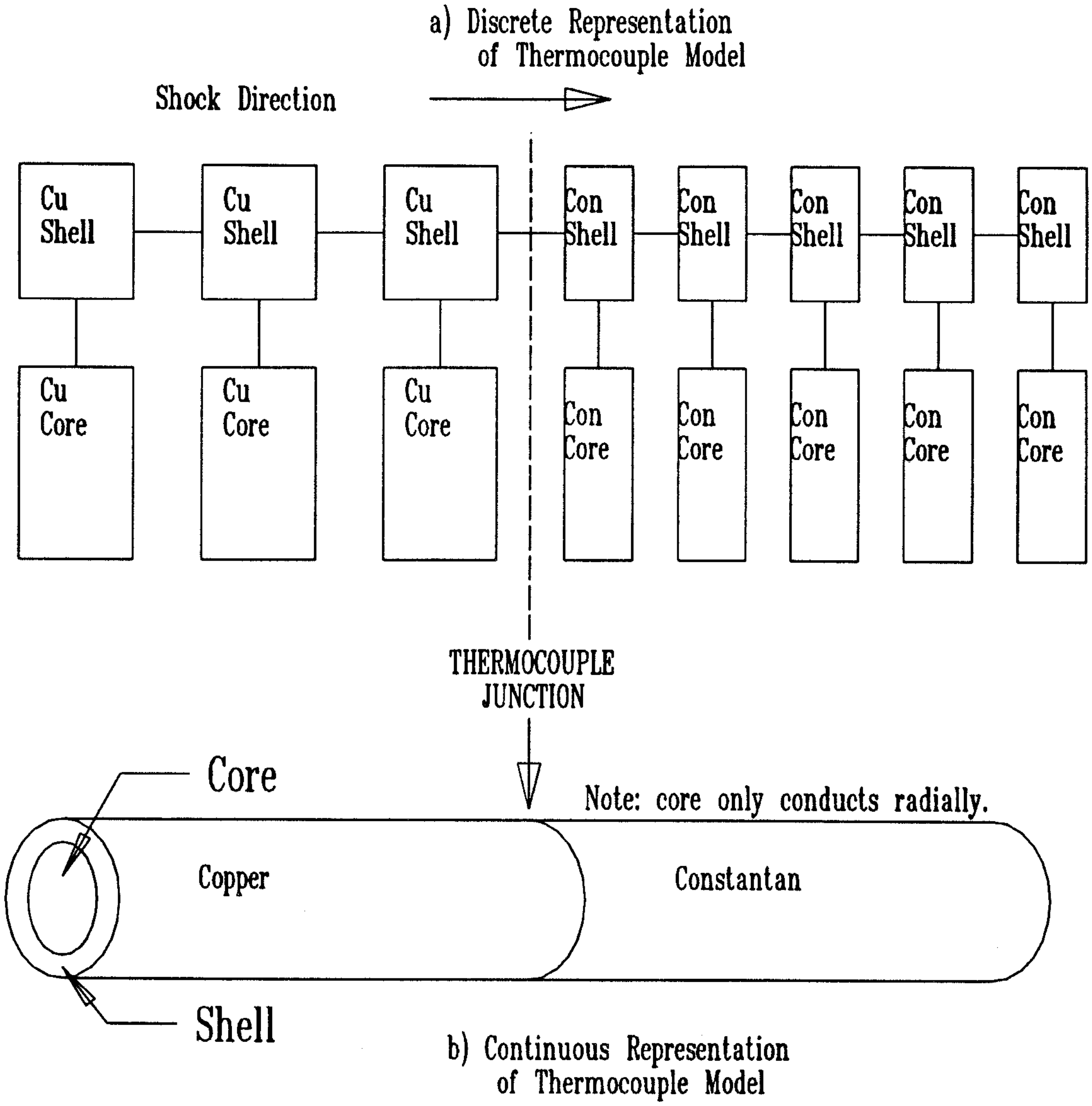

Fig. 4.12 Schematic representation of the thermocouple model. In a), the discrete representation, thermal masses are represented as boxes, and thermal resistances as lines. In b), the continuous representation, the core does not conduct in the axial direction.

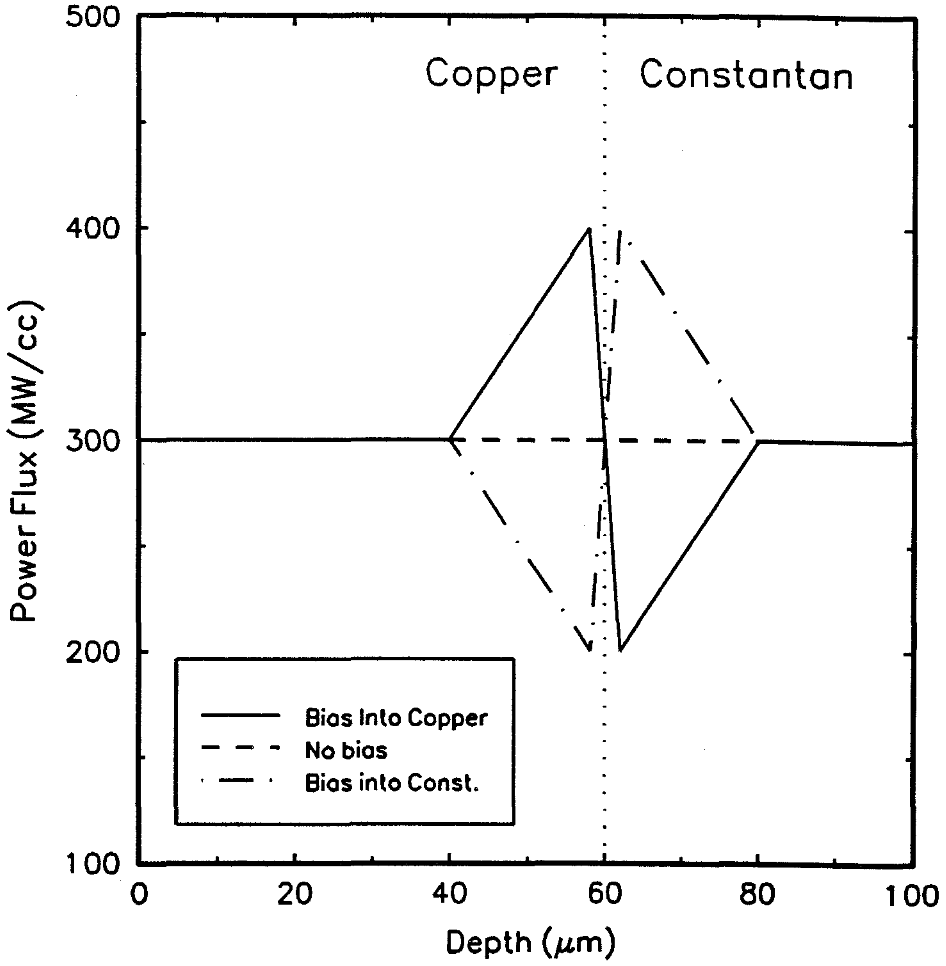

Fig. 4.13 Plot of energy flux vs. position as applied in the thermocouple model, under positive, zero, and negative energy bias into the copper. These correpond to Eext = 1, Eext = 0, and Eext = –1, respectively.

References

1. N. N. Thadhani, A. H. Mutz, P. Kasiraj, and T. Vreeland Jr., in *Metallurgical Applications of Shock–Wave and High–Strain–Rate Phenomena*, edited by L. E. Murr, K. P. Staudhammer, and M. A. Meyers (Dekker, New York, 1986), p. 247.
2. T. Vreeland Jr., P. Kasiraj, A. H. Mutz, and N. N. Thadhani, in *Metallurgical Applications of Shock–Wave and High–Strain–Rate Phenomena*, edited by L. E. Murr, K. P. Staudhammer, and M. A. Meyers (Dekker, New York, 1986), p. 231.
3. R. B. Schwarz, P. Kasiraj, and T. Vreeland Jr., in *Metallurgical Applications of Shock–Wave and High–Strain–Rate Phenomena*, edited by L. E. Murr, K. P. Staudhammer, and M. A. Meyers (Dekker, New York, 1986), p. 313.
4. Williams Q., Jeanloz R., Bass J., Svendsen B., Ahrens T. J., Science. **236**, 4798 (1987).
5. N. W. Ashcroft and N. D. Merman, *Solid State Physics* (Saunders, Philadelphia, 1976) p. 256.
6. J. Jaquesson, Bull. du G.A.M.A.C. IV. **4**, 33 (1959).
7. D. D. Bloomquist, G. E. Duvall, and J. J. Dick, J. Appl. Physics. **50**, 4838 (1979).
8. V. F. Nesterenko, Paper presented at the All–Union School on Explosion Physics in Krasnoyarsk, USSR (1984). English translation by the Berkeley Scientific Transl. Service, #UCRL–TRANS–12054, March 1985.
9. Akella J., J. Geophys. Chemistry. **76**, 4969 (1971).
10. J. Bartels, P. T. Bruggencate, H. Hausen, K. H. Hellwege, K. L. Schafer, and E. Schmidt, ed., *Landolt–Bornstein: Zahlenwerte und Funktionen aus Physik, Chemie, Astronomie, Geophysik, und Technik* (Springer–Verlad, Berlin, 1957) p. 47.

CHAPTER 5

HARDNESS AND DEFORMATION IN SHOCK CONSOLIDATION

5.1 Introduction

Material strength is one of the most obvious fundamental parameters influencing the shock wave consolidation process. The effect of strength on heterogeneous energy deposition is not well established. Another complication is the lack of strain rate hardening data at very high strain rates, as discussed in the introduction. Notwithstanding these limitations, an attempt to investigate the effect of strength on energy localization has been made; will a harder material experience more uniform or less uniform heating during consolidation? The hardness of the material has been used to characterize the strength.

Observations of the effect of hardness on shock wave consolidation can be complicated by differences in particle shock impedance, size, and melting behavior. To isolate the effect of hardness, a highly hardenable steel alloy, M350 maraging steel, was used as a study material. By heat treating for different times at 480° C, the yield strength may be varied from 0.8 GPa to 2.4 GPa [1]. By shock consolidating multiple samples of the powder in the same shot, very similar impact conditions were achieved. The M350 powders were shocked in the hardened and unhardened states, and with hard and soft powders mixed together. The samples were examined metallurgically, tested for post–shock hardness, and tested mechanically in tension using the miniature 'dog bone' tensile test apparatus described in Chapter 6.

5.2 Experimental Design

M350 maraging steel ($Ni_{18}Mo_{4.2}Co_{12.5}Ti_{1.6}Al_{0.1}$) powder, prepared via inert gas atomization, was obtained from United Technologies. The powder particles are roughly spherical, as shown in Fig. 5.1. The powder was sieved into various size fractions, and some of the powder was heat treated in Ar for 6 hours at 480° C. Under this heat treatment, the hardness of M350 steel typically increases from HV 280 to HV 700 [1]. In the first set of experiments, the hardened and unhardened powders were loaded into cavities formed by drilling 10mm holes into porous bronze filter material. See Fig. 5.2. The bronze (from Pacific Sintered Metals) has a solid density of approximately 8.4 gm/cm^3, and the maraging steel has a density of 8 gm/cm^3. The impedance mismatch between the two materials is sufficiently small to retain planar shock conditions over the majority of the consolidated slugs. (A truncated cone of near right angle will be consolidated under the plane wave condition, as discussed in Chapter 2.) Experimental parameters are summarized in Table 5.1. In the second set of experiments, the powders were placed into three 120° sectors of the 32 mm dia. target cavity. The sectors were defined by 0.1 mm thick 304 SS sheets. Since the sheet thickness was comparable to the powder diameter, strong perturbations in the shock state were avoided far from the sheet; the powder 'rings down' to the average shock state. To reduce surface oxides, the powders were treated in H_2 at 350° C for 2 hrs.

Vickers hardness measurements were made using a Leitz Miniload hardness instrument, loading the diamond indenter with 50 gm. The indents were typically 15 μm on the diagonal.

5.3 Results and Discussion

After shock consolidation, the compacts were mounted, polished, and etched with Marbles reagent to reveal grain boundaries. The small compacts produced in the first experiments showed non–etching regions at particle peripheries which appear to correspond to melted and rapidly quenched material. See Fig. 5.3. The larger compacts were shocked at higher energy, and did not exhibit this structure except near the compact edges where quenching by the target ring was most rapid. See Fig. 5.4. A mixture of hardened and unhardened powders was shocked also. The polished and etched structure in shown in Fig. 5.5. The hardened particles etch darker, due to presence of intermetallic precipitates on the boundaries of martensitic laths [1]. Note the greater deformation of soft particles at the intersections of hard and soft particles. When particles of similar hardness interact, they do so as in Fig. 5.3; the local neighborhood of particles determines the deformation pattern.

Vickers hardness, HV, is defined as

$$\mathrm{HV} = \frac{1854}{d^2} * \mathrm{M},$$

where d is the length of the indent diagonal in microns, and M is the indent load in grams. Within a system, the hardness is roughly proportional to strength, but different work hardening behaviors will substantially change this. The ratio of strength to hardness is not exact, and may change from material to material. A more complete discussion of various hardness tests is included in *Smithells Metals Reference Book* [2].

The hardness of the particles was altered during shock wave consolidation. In particular, the softer particles were hardened during the shock consolidation process. Since maraging steels have very little work–hardening behavior [1], the temperature excursion during consolidation is most likely to be responsible. The non–etching regions had a hardness of HV 420 – 570. The thickness of the melt pools is difficult to measure, and the impressions may be of depth comparable to pool thickness in the lower hardness measurement. The hardened particles had HV 400 ±40, and the unhardened particles had a post–shock hardness of HV 320 ± 20. The particles were identified by etching behavior, and etching the grain boundaries of the hardened particles apparently reduced the measured hardness. Wrought M350 maraging steel in the unhardened condition has a typical hardness of HV 280, and upon heat treatment is brought to HV 700. The broken tensile samples were also hardness tested. The tensile samples had hardness of HV 550 ± 40.

Tensile tests conducted on dog bone shaped samples of the shock consolidated and heat treated material were conducted. The sample were machined using an Agietron electric discharge machine. See Chapter 6 for details of the tensile apparatus. A variety of heat treatments were made. See Table 5.2. The samples all exhibited incomplete particle bonding, with ductile failure occurring at well bonded particle junctions, as exhibited in the SEM fractograph, Fig. 5.6. This is in contrast to the complete bonding of Pyromet 718 discussed in Chapter 6. Following these tensile tests, higher energy shots were made to improve interparticle bonding. Neither a reducing treatment in hydrogen nor larger shock energies changed this behavior.

The lack of complete interparticle bonding is puzzling. A variety of other steels, such as 304SS [3] and AISI 9310 [4] have been well–bonded using shock wave consolidation under comparable conditions. The amount of melted and refrozen material, as characterized by the fraction of nonetching material, is similar to that in the successful consolidation of Markomet 1064, as discussed in Chapter 3. The powder surfaces may have been contaminated or oxidized, but the powders as received are bright, and maraging steels are corrosion resistant relative to low–alloy steels. Surface contamination, a traditionally bothersome problem during shock wave consolidation must be considered the most likely culprit, but it is possible that a very high flow strength at high strain rate would tend to delocalize energy deposition during shock wave consolidation and interfere with good interparticle bonds.

5.4 Conclusions

Within the maraging steel system, uniform particle hardness does not measurably change the energy deposition process during shock wave consolidation. Shock pressures well in excess of the material yield strength were employed. The quality of the resulting compacts did not change under a threefold change in initial yield stress.

When hard and soft particles interact under shock conditions, soft particles are significantly deformed relative to neighboring harder particles. Only directly interacting particles are obviously affected; this is consistent with a particle scale width shock front as discussed in Chapter 4. Energy input into soft particle interiors is evidently higher.

Table 5.1. Parameters in M350 maraging steel shock consolidation experiments. Shock pressure and energy are calculated using Hugoniot data from *LASL Shock Hugoniot Data* [5], for Vascomax 300 maraging steel.

Shot	Porosity	Flyer Velocity (m/s)	Shock Pressure (GPa)	Shock Energy (J/g)	Powder Size (μm)	Powder Heat Treat
16–1	31%	990	9.3	260	74–150	as–rec.
16–2	31%	990	9.3	260	75–150	6hr 480° C
16–3	31%	990	9.3	260	75–150	50% as–rec. 50% 6hr 480
17–1	33%	1240	12.7	395	75–150	as–rec.
17–3	33%	1240	12.7	395	75–150	6 hr 480° C

Table 5.2. Results of tensile tests on small 'dog bone' tensile samples of M350 steel, prepared by shock consolidation and by hot isostatic pressing, after various heat treatments.

Shot	Powder Heat Treat	Post–Shock Heat Treat	Failure Stress (not ductile) (GPa)
17–1	none	5 hrs 490° C.	1.11
	none	1 hr 815° C and 5 hrs 490° C	1.25
	none	5 hrs 490° C	1.43
17–3	6 hrs 480° C	5 hrs 490° C	1.21
	6 hrs 480° C	5 hrs 490° C	1.21
	6 hrs 480° C	1 hr 815° C and 5 hrs 490° C	1.25

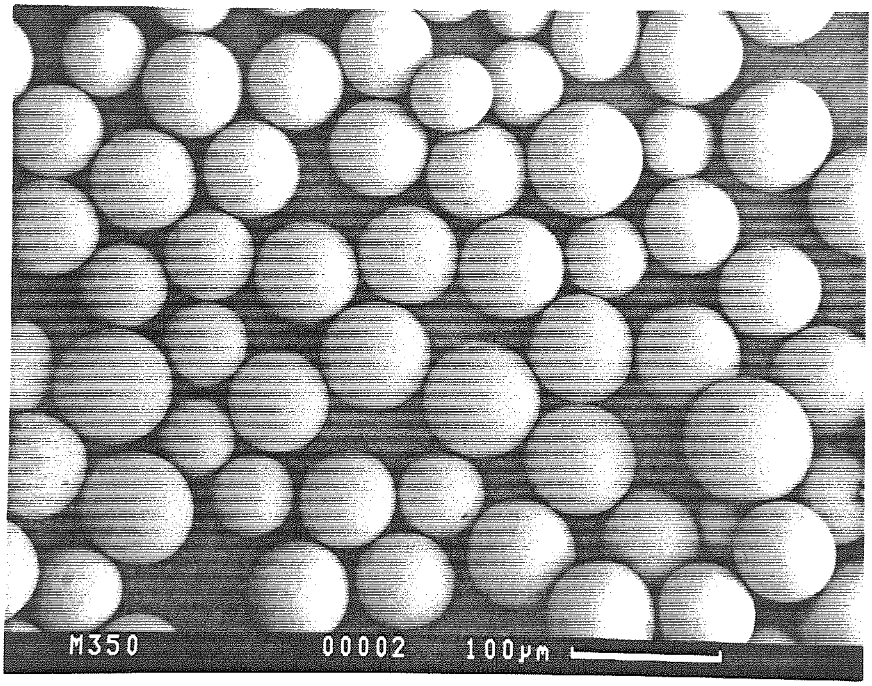

Fig. 5.1 Scanning electron micrograph of M350 maraging steel powder, 63–74μm powder size.

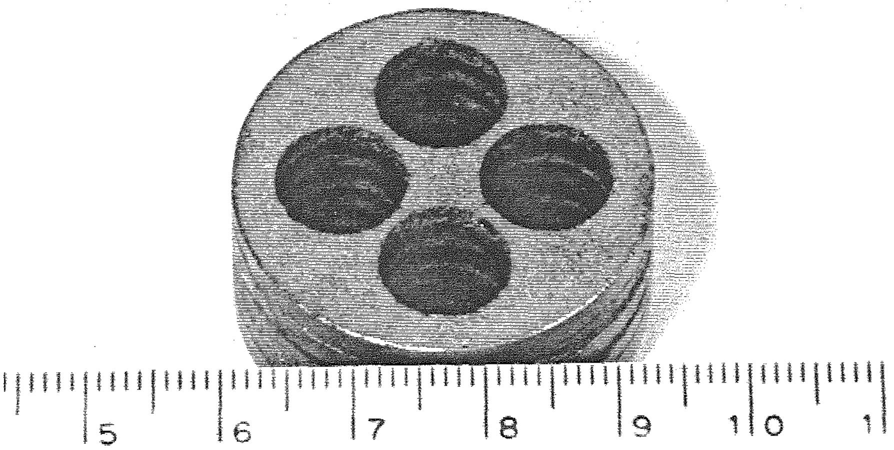

Fig. 5.2 Photograph of porous bronze target insert. Holes are reamed to 10mm dia., thickness is 9.5 mm, and outer diameter is 32.2 mm.

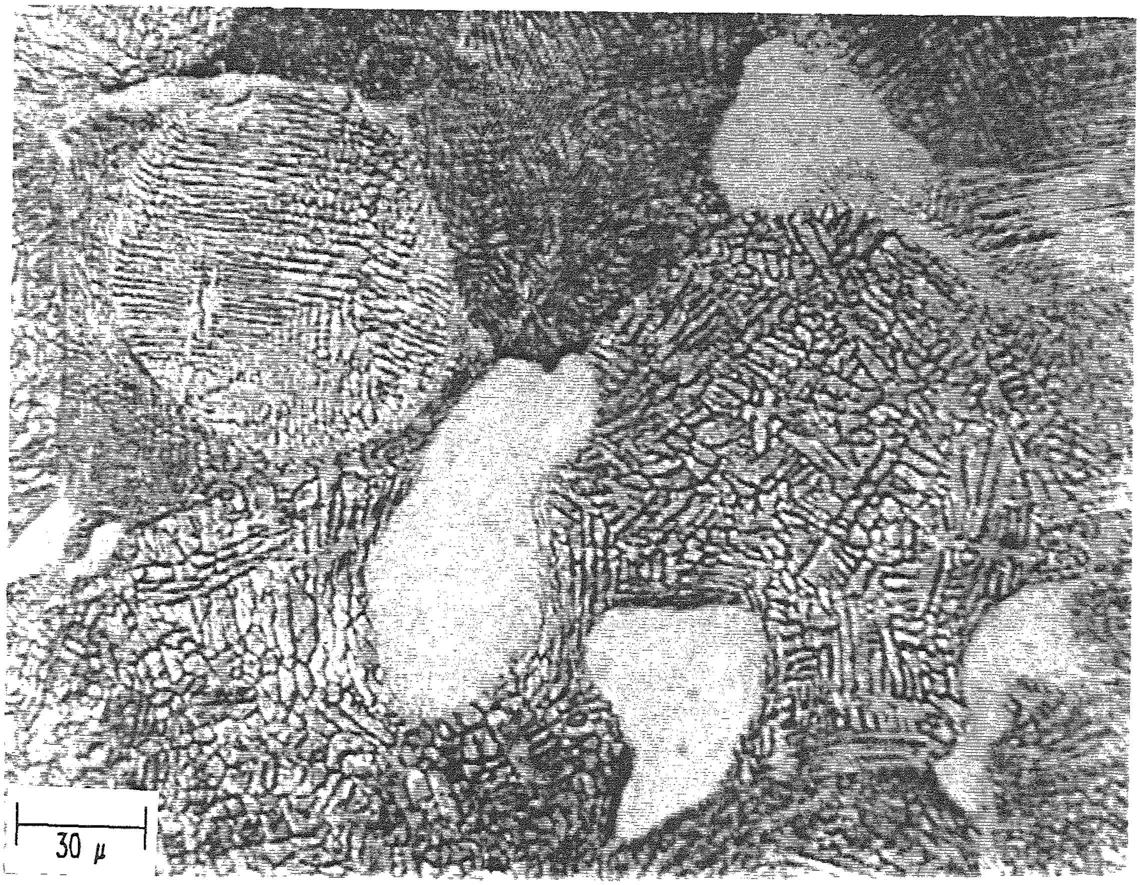

Fig. 5.3 Micrograph of polished and etched shock consolidated M350 maraging steel powder (shot #17–3), heat treated before shock.

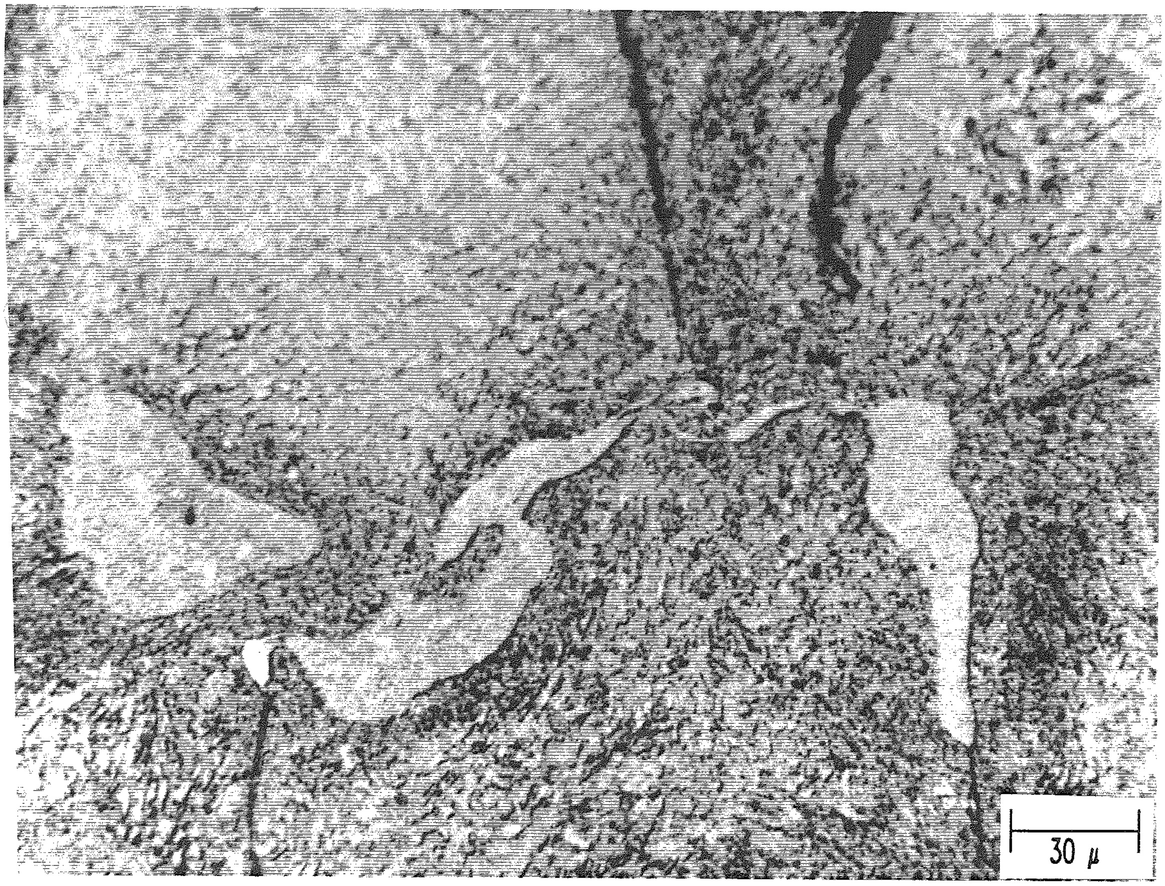

Fig. 5.4 Micrograph of polished and etched shock consolidated M350 maraging steel powder, from near edge of large compact (shot #62).

Fig. 5.5 Micrograph of polished and etched shock consolidated mixture of hardened and unhardened M350 maraging steel powders (shot #16–3)..

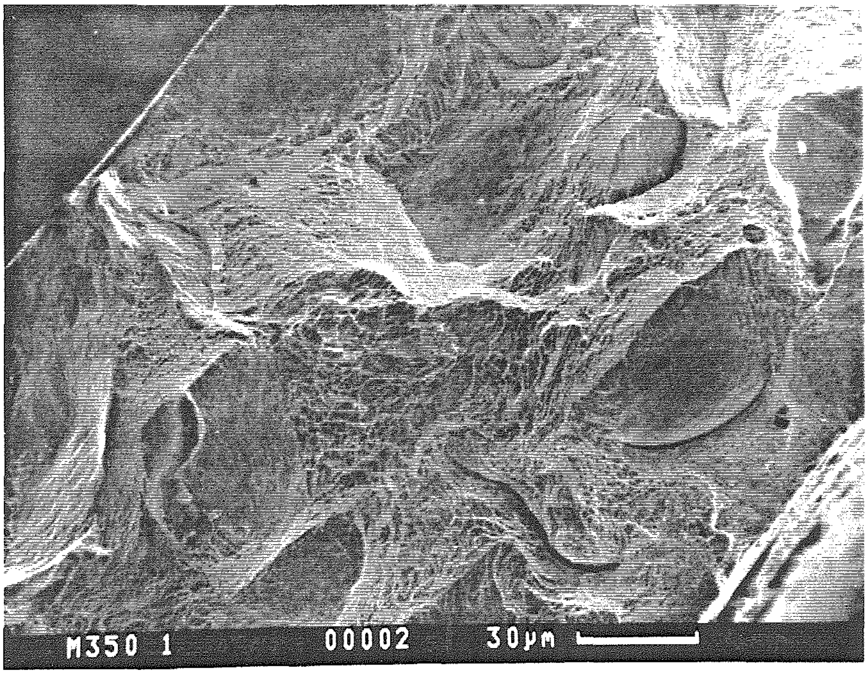

Fig. 5.6 Scanning electron image of fracture surface of tensile sample #1 in Table 5.2, heat treated before and after shock consolidation.

References

1. B. P. Bardels, ed., *Metals Handbook Ninth Edition Vol. 1* (ASM, Metals Park Ohio, 1978) p. 449.
2. E. A. Brandes, ed., *Smithells Metals Reference Book, Sixth Edition* (Butterworths, London, 1983) p. 21–1.
3. G. E. Korth, J. E. Flinn, and R. C. Green, in *Metallurgical Applications of Shock–Wave and High–Strain–Rate Phenomena*, edited by L. E. Murr, K. P. Staudhammer, and M. A. Meyers (Dekker, New York, 1986), p. 129.
4. P. Kasiraj, *Shock Wave Consolidation of Metallic Powders* (Ph. D. Thesis, Caltech, 1984) p 84.
5. S. P. Marsh, ed., *LASL Shock Hugoniot* (University of California, Los Angeles, 1980) p. 221.

CHAPTER 6

TENSILE PROPERTIES OF A SHOCK CONSOLIDATED NI SUPERALLOY

6.1 Introduction

Considerable work involving rapid solidification processing (RSP) and consolidation of Ni–based superalloys has been performed in the last several decades [1,2,3]. Although the advantages of rapid solidification processing, in increased homogeneity and refinement of microstructure have been demonstrated, many of these advantages are lost when the consolidation of superalloy powders is accomplished by conventional methods such as extrusion or hot–isostatic pressing. These processes involve very prolonged thermal excursions during which the temperatures approach the γ' or γ'' solvus. The intermetallic γ'' (Ni_3Nb) precipitates are the principal hardening phase. Consequently, the resulting microstructure is coarser than that of the RSP powder. Furthermore, the distribution of the γ'and γ'' phases is comparable to that developed in the material produced by conventional casting techniques. Therefore, the advantages of rapid solidification processing of Ni–based superalloys can be fully exploited only if the powder is consolidated in the absence of prolonged heating.

Shock wave consolidation fulfills this requirement and can be used for producing bulk solids with metastable structures. The consolidation of the powder to full, solid density occurs by the passage of a shock wave of sufficient amplitude. Within a short time interval (rise time of the shock wave ≈80 ns), the energy of the shock wave is utilized in plastically deforming the powder particles and reducing the void volume to virtually zero. This results in preferential heating of the particle exteriors which can cause melting of particle surfaces and interparticle welding. The heating and melting of the particle surfaces occurs in time durations too small for atomic diffusion to occur over distances comparable to the particle size. The melted interparticle material rapidly solidifies due to the heat flow towards relatively cool particle interiors at rates as high as 10^{10}° C/s [4], thereby retaining the RSP microstructures.

In this investigation, a rapidly solidified Ni–based Pyromet 718 superalloy powder ($Ni_{52.5}Fe_{18.7}Cr_{18.4}Nb_{5.3}Mo_{3.0}Ti_{1.0}Al_{0.6}$ wt%) was shock consolidated. Mechanical (tensile) properties of the shock consolidated material were measured. These were then compared with the properties of similar powder material consolidated by hot–isostatic processing. Metallurgical observations were made to elucidate the mechanical properties.

A comprehensive examination of the defect and precipitate structure of the hot–isostatically pressed and shock–wave consolidated Pyromet 718 was conducted using transmission electron microscopy by Prof. Naresh Thadhani [5]. Some of these observations are presented.

6.2 Experiment

A rapidly solidified nickel–based superalloy powder (10–44 μm diameter) obtained from Carpenter Technology was consolidated by a planar shock front of 9.5 GPa (stainless steel flyer impact velocity of 1.135 km/s). Details of the consolidation technique are described elsewhere [6]. The individual powder particles were microcrystalline with both cellular (0.25 – 0.5 μm) and dendritic (1.0 – 3.0 μm) grains. A scanning electron micrograph of the as–received powder is shown in Fig. 6.1a, and an optical micrograph of the polished and etched powder mounted in lucite is shown in Fig. 6.1b.

The recovered consolidated samples (5 mm thick – 20 mm diameter) were cut parallel and perpendicular to the shock direction. Optical and transmission electron microscopy were performed to analyze the structural changes produced by compaction at the interparticle regions and within particle interiors. For optical microscopy, the sections were mechanically polished and etched with 5% $FeCl_3$ solution. Samples for transmission electron microscopy were prepared by cutting 3.0 mm diameter discs from sections of the compact mechanically polished to 150 μm thickness and final thinning by twin–jet electro–polishing with butyl cellusolve.

For tensile tests, small dog–bone shaped specimens (gage section 2.1 x 0.7 x 0.3 mm) shown in Fig. 6.2a were cut from the planar sections by electric discharge machining. The specimens were pulled to failure in a three–legged frame designed to minimize bending stress in the sample. The tensile sample is one of the three load–bearing legs, shown schematically in Fig. 6.2b. Specimen extension was measured using an LVDT referenced to the holes in the ends of the sample. Tensile tests were conducted on the as–consolidated and heat treated samples of both the hot–isostatically–pressed (hipped, obtained from Carpenter Technology) and shock consolidated samples of Pyromet 718. The shock consolidated and hipped samples were both subject to a standard heat treatment, 1066° C for one hour, followed by initial aging at 740° C for 8 hours, and a final aging at 620° C for a period between 8 and 40 hours.

6.3 Results and Discussion

The rapidly solidified Pyromet 718 powder was dynamically consolidated to full bulk density with a total calculated shock input energy of 400 J/g. The microcrystalline powder particles are bonded together by interparticle regions which appear to have melted and rapidly solidified to a fine microcrystalline structure.

Fig. 6.3a shows an optical micrograph of the shock consolidated Pyromet 718 alloy (sectioned in the plane of the shock). The powder particles have a dendritic structure as observed in the RSP powder (Fig. 6.1), and are surrounded by a featureless microcrystalline phase.

An optical micrograph of the Pyromet 718 alloy powder produced by hot–isostatic pressing is shown in Fig. 6.3b. In the hipping technique, the powder filled containers are placed in an autoclave which is subsequently heated and pressurized normally to 1100–1200° C and 1 kbar, resulting in fully dense compacts. As seen in Fig. 6.3b, a dark oxide layer (indicated by a glyceragia etch) surrounds the particle surfaces.

Tensile Properties

Results from the tension tests, performed on the as–shock–consolidated and hipped samples, revealed that the shock consolidated material had at least a 10% higher yield strength (0.2% yield criterion) than the hipped material, although it had practically zero ductility in the as–consolidated state. The hipped sample showed up to 10% elongation and a higher ultimate tensile strength.

Following solution treating and aging, both the yield strength (YS) and ultimate tensile strength (UTS) of the shock consolidated material showed a significant increase over that of the hipped material. The tensile test results for shock consolidated material and the hipped material are shown as plots of yield strength vs. aging time (Fig. 6.4a) and ultimate tensile strength vs. aging time (Fig. 6.4b). Error bars in the figures show estimated experimental uncertainty based primarily on irregularities in gauge section dimensions. It is clear from the two plots that following heat treatment the properties of the shock consolidated material are superior to those of the hipped alloy; UTS of the shocked alloy is 20% greater, YS is 40% greater than the hipped alloy, and ductility is comparable. The tensile properties measured in the hipped material are consistent with full–size tensile samples of commercially produced superalloy 718 [7].

This improvement in the mechanical properties is attributed to microstructural differences in the shock consolidated and hipped materials. As indicated in the optical micrographs in Fig. 6.3a and 6.3b, the shock consolidated sample has an extremely fine grain size in the interparticle regions created by the rapid cooling of the interparticle melt formed during the passage of the shock wave. In contrast, the hipped sample has a layer of oxidized material surrounding the particles.

Transmission Electron Microscopy

In the process of shock consolidation, the energy of the shock is inhomogeneously deposited at particle surfaces and within the particle interiors. As discussed in Chapters 2 and 4, a non–negligible amount of energy is utilized in plastic deformation of powder particle interiors. The remaining energy is deposited near powder particle surfaces and results in local heating and melting.

The material melted during shock consolidation of Pyromet 718 rapidly solidifies to a fine microcrystalline structure. Fig. 6.5 is a bright field TEM micrograph of an interparticle region in shock consolidated Pyromet 718. The grain size of the interparticle material is 0.05 – 0.1 μm, at least three times smaller than the grain size in the particle interiors.

Evidence of extensive plastic deformation within powder particle interiors was also observed. The deformation results in the formation of twins and dislocation pile–ups and tangles within the individual grains. See Fig. 6.6

Shear localization bands, resulting from inhomogeneous plastic deformation during shock consolidation, are also observed within the particle interiors of the Pyromet 718. Shear deformation is localized in narrow bands spanning over several microcrystalline grains, but confined to individual powder particles. The shear bands appear either as several isolated bands or as a packet of bands parallel and nearly equidistant from one another. Fig. 6.7 is a TEM micrograph showing shear bands in the shocked powder. These bands are 0.005 – 0.010 μm thick and 1.0 μm long in a microcrystalline (0.25 – 0.5 μm grain size) matrix. Contrast changes are revealed as the bands cross grain boundaries. The material within the shear bands reveals somewhat periodic fringe contrast, characteristic of micro–twinning.

Observations of fully heat treated samples of both the hipped and shock consolidated samples showed considerably smaller precipitates present in larger numbers in the particle interiors of shock consolidated material [5]. The higher density of finer precipitates is expected to increase the strength of the material.

6.4 Conclusions

Shock consolidated Pyromet 718 superalloy powder shows mechanical strength superior to the hipped material, and comparable ductility, after heat treatment. This is attributed to improved interparticle bonding and grain size refinement in interparticle regions of the shock alloy, and increased density of precipitates.

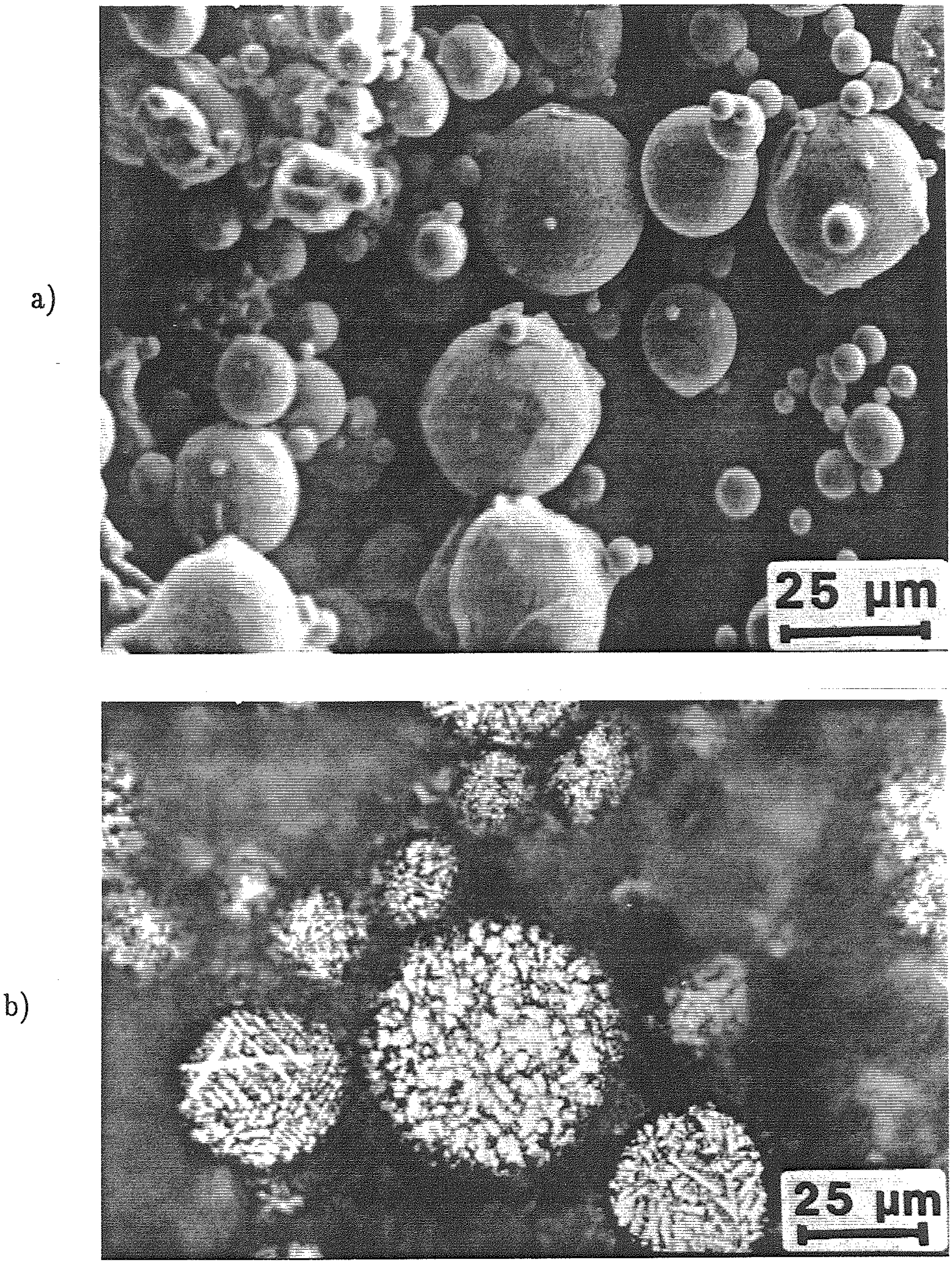

Fig. 6.1 a) Scanning electron micrograph of as–received Pyromet 718 powder, and b) optical micrograph of the powder after mounting, polishing, and etching.

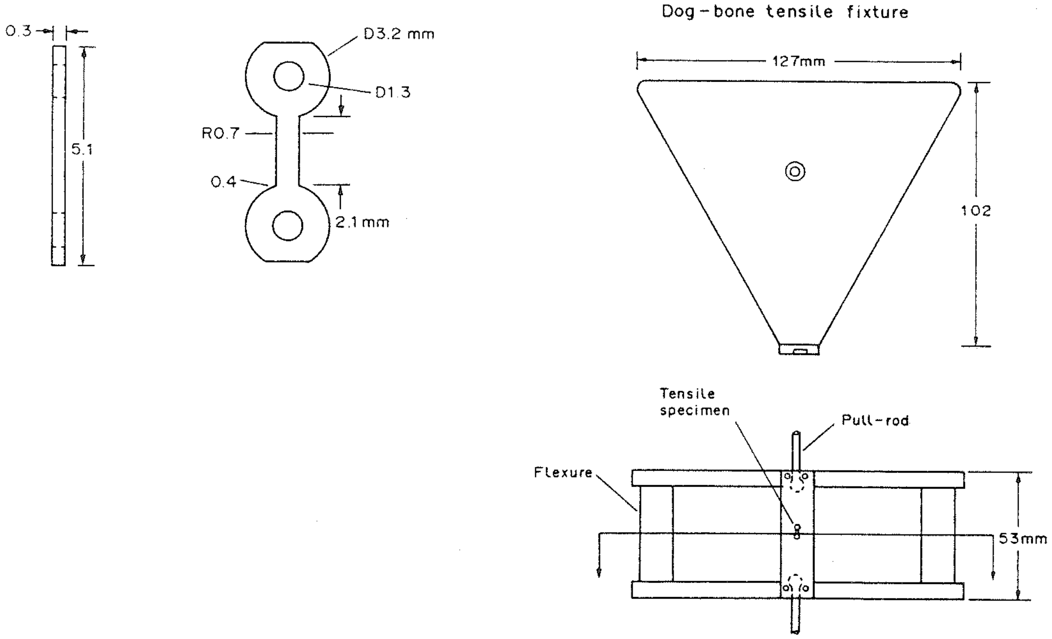

Fig. 6.2 Illustration of the tensile sample and tensile frame. The sample is scaled up to show detail.

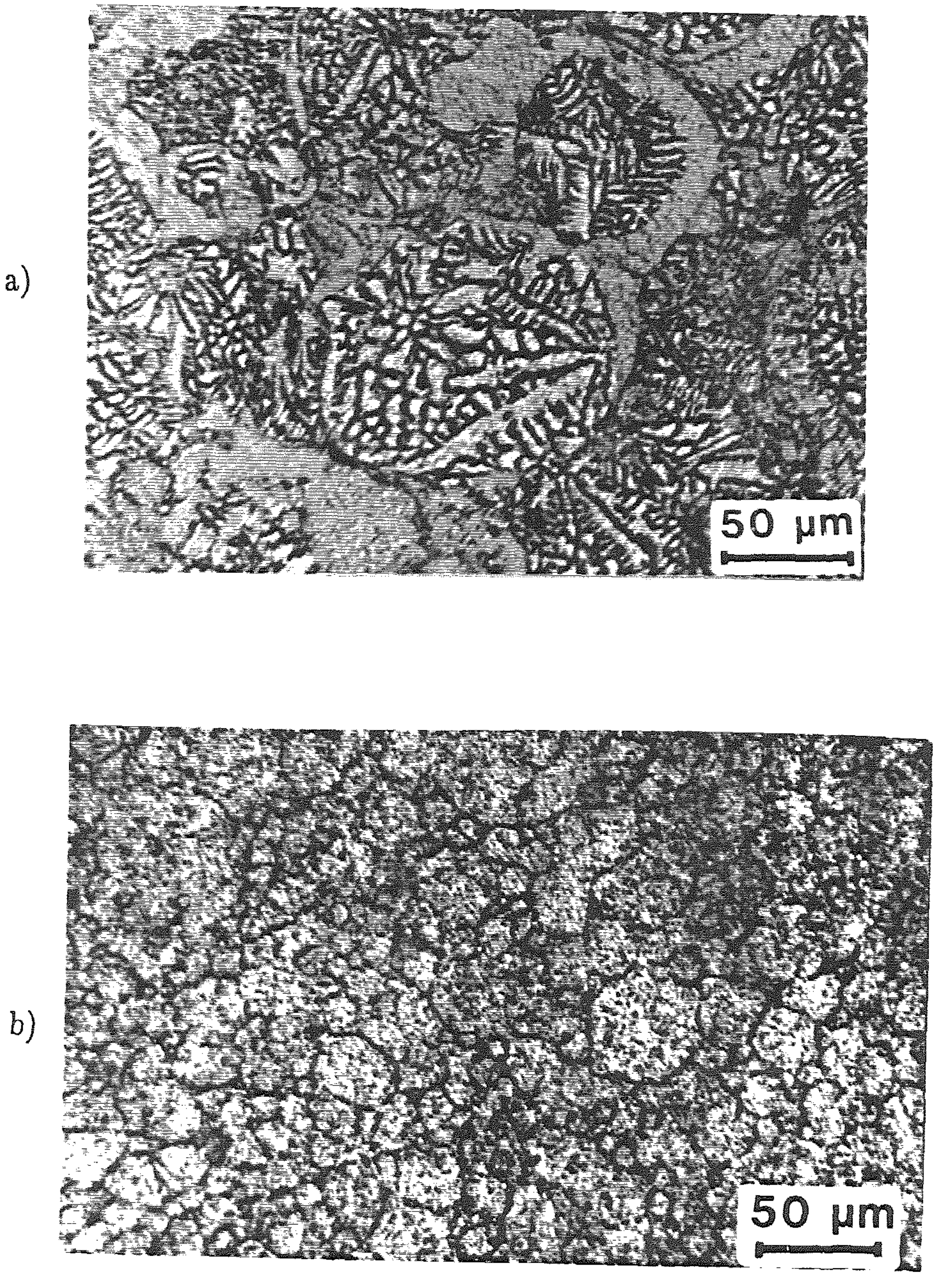

Fig. 6.3 Optical micrographs of a) shock consolidated and b) hot isostatically pressed samples of Pyromet 718.

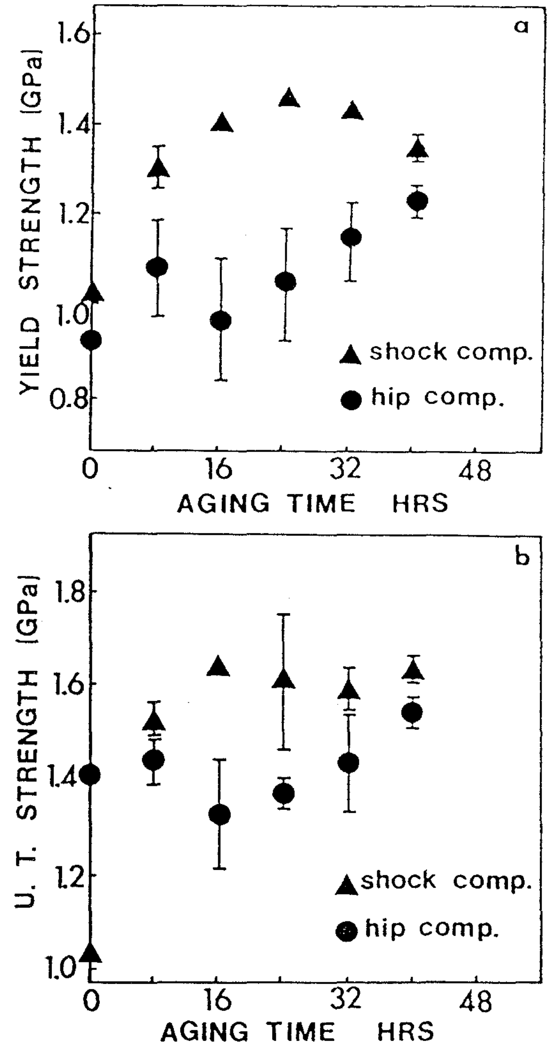

Fig. 6.4 Plots of a) yield strength (YS) and b) ultimate tensile strength (UTS) vs. aging time for shock consolidated and hot isostatically pressed Pyromet 718.

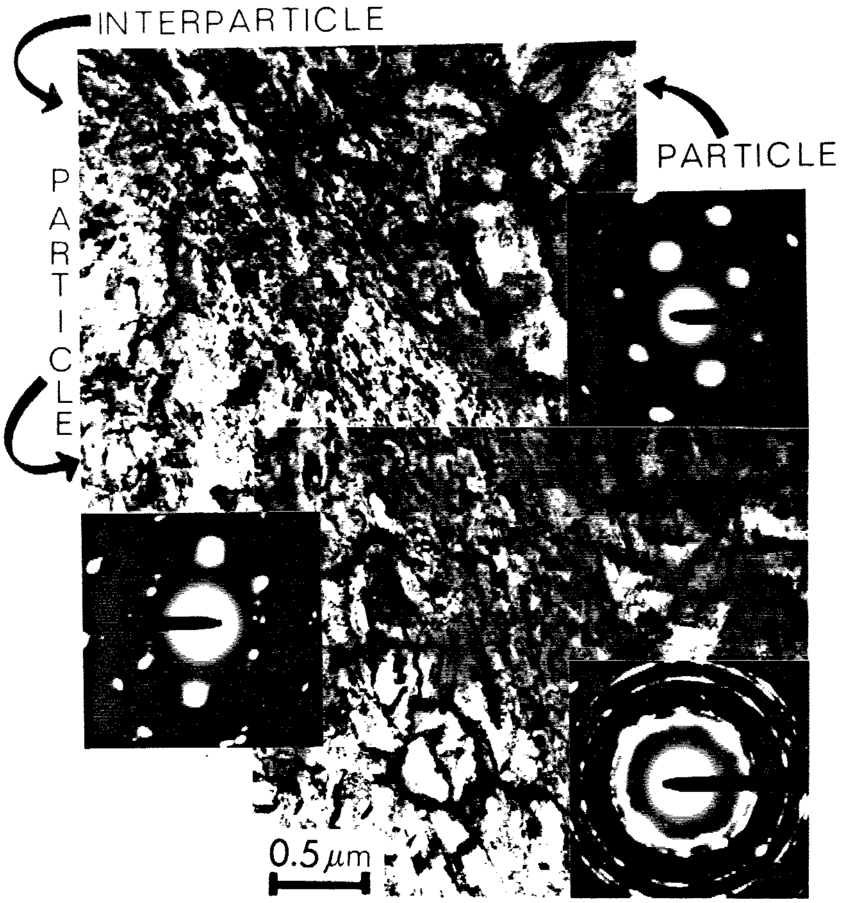

Fig. 6.5 Bright field TEM micrograph of an interparticle region of shock consolidated Pyromet 718, revealing grain size decrease at particle interfaces.

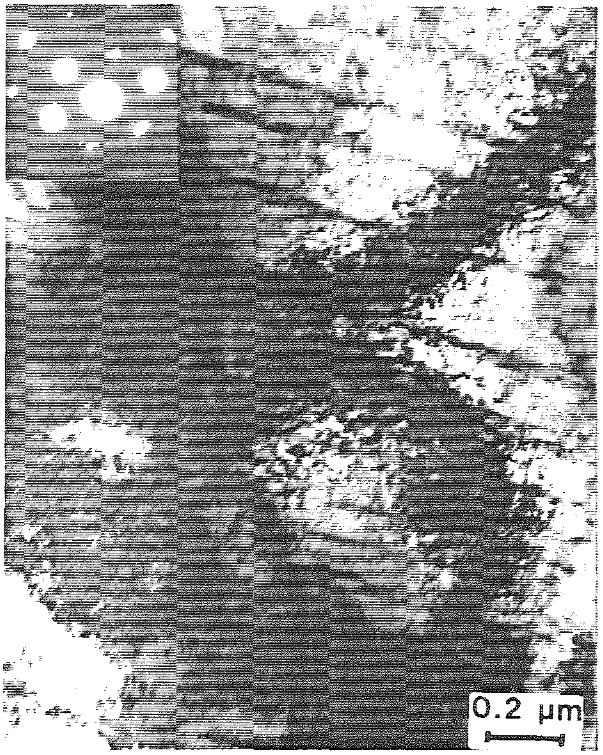

Fig. 6.6 Bright field TEM micrograph of an intraparticle region of shock consolidated Pyromet 718, revealing dislocation structures and twins.

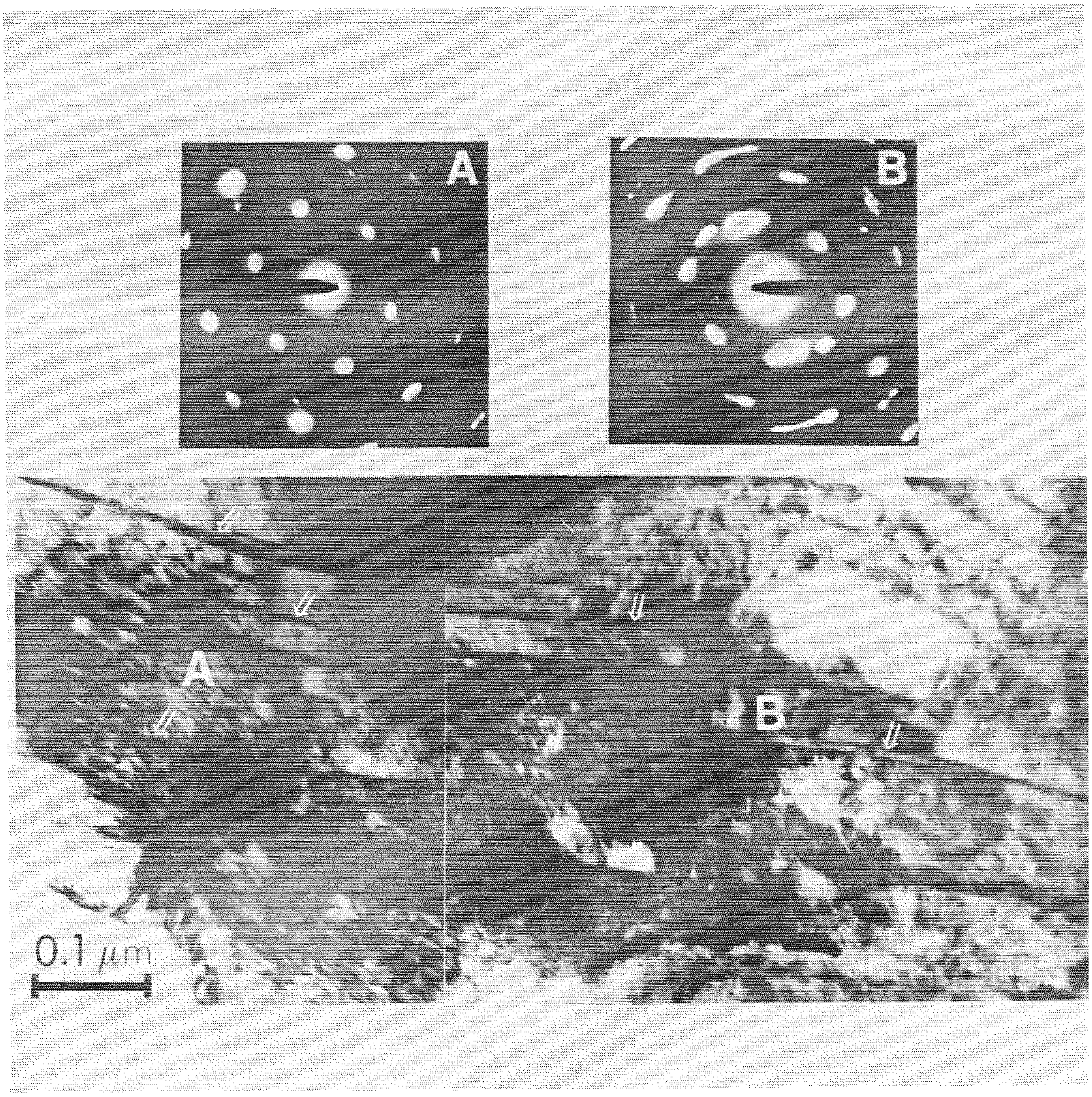

Fig. 6.7 Bright field TEM micrograph of shear bands in shock consolidated Pyromet 718. The bands cross several grains.

References

1. C. Hammond and J. Nutting, Metal Sci. **11**, 474 (1977).
2. D. F. Paulonis, J. M. Oblak, and D. S. Duvall, Trans. Am. Soc. Metals. **62**, 611 (1969).
3. A. R. Cox, J. B. Moore, E. C. Van Reuth, *Proc. 3rd Int. Symp. on Superalloys* (Claitors, Baton Rouge, 1976) p. 45.
4. D. G. Morris, J. Mater. Sci. **16**, 457 (1982)
5. N. N. Thadhani, A. H. Mutz, and T. Vreeland Jr., Acta Met. **37**, 897 (1986).
6. N. N. Thadhani and T. Vreeland Jr., Acta Met. **34**, 2323 (1986).
7. B. P. Bardels, ed., *Metals Handbook Ninth Edition Vol. 1* (ASM, Metals Park Ohio, 1978) p. 219.

CHAPTER 7

MULTIPLE CAVITY AND NEAR NET SHAPE CONSOLIDATION

7.1 Introduction

Multiple cavity experiments are usually done by encapsulating samples of powder in a solid, rigid fixture, and subjecting the entire assembly to a flyer plate impact or an explosive pressure pulse. The samples undergo equivalent pressure and energy conditions (if the samples are themselves similar) but the shock history of each is fairly complex; waves traveling through the target wrap around the capsules and subject different portions of a cavity to widely varying pressures [1]. Extensive numerical simulations have facilitated interpretation of resulting compacts but are not easily performed for every compact and geometry [2]. Simplifying the shock conditions facilitates interpretation of the experiments.

Striking only porous materials of similar impedance to the encapsulated samples creates samples subject to nearly one–dimensional shock conditions if the shock geometry is one–dimensional; the waves in the porous media do not 'wrap around', but proceed at approximately the same velocity as the shock wave in the sample. A similar line of reasoning led to the embedded off–center tube technique used in a cylindrical geometry [3].

Using this design philosophy, three types of plane wave experiments have been conducted: powders were loaded into cavities drilled into sintered bronze foam, thin stainless steel dividers were used to separate three sectors of powders of differing particle size distribution, and a pressed 'green' compact of discontinuously reinforced metal matrix composite material was embedded in a ceramic powder of similar shock impedance. Each of these target geometries was shocked by a flyer plate impact. The specific geometries and procedures are somewhat different, but the idea is consistently the same. The advantages in analytic experimentation are paralleled by possible technological advantages.

7.2 Experiments

Porous sintered bronze fixture

Commercially made porous bronze filter material (Pacific Sintered Metals F–100) was machined into 32mm dia. x 9.5mm thick disks with four 10 mm holes. The sintered bronze has a mean density of 4.7 g/cm^3 corresponding to a porosity of 46%. (See Fig. 7.1.) The cavities were separately loaded with carbonyl Ni powders of differing morphologies and pressed to 46% porosity. The carbonyl process nickel powders, obtained from Inco Metals, were 7–10μm spheres, 5.5–6.5 μm spiked spheres, 1 μm thick x 30 μm flakes, and 2μm thick x 10 μm long filaments. Shot 25 was performed using the Keck Dynamic Compactor, a propellant–charged gas gun accelerating a 5mm 303 SS flyer plate to 1.17 km/s. This impact shocked the Ni powders to a calculated pressure of 9.1 GPa and deposited approximately 430 J/g of thermal energy into the powder. Three well–bonded pills were recovered. A micrograph of the compacted spiked spherical powder is shown in Fig. 7.2. The flaky powder did not bond well, and was apparently contaminated by the roller lubricant used in manufacturing.

Stainless steel dividers

We surmised that cavity partitions with thicknesses on the order of a particle diameter or less would have minimal effect on the shock loading conditions of the material in the fixture. If the materials themselves were nearly the same, the shock conditions in each would not interfere with the others, thus each would be subject to the same uniaxial shock conditions. The 304 stainless steel (SS) shim stock used was 0.13 mm thick. The C350 maraging steel powder was sieved into various fractions from 44–300 μm dia. The first cavity was loaded with 9.5g 125–150μm plus 9.5g 53–74μm powder. The second cavity had 9.5g 180–300μm and 9.5g 44–53μm powder. The third cavity was filled with 19g of 180–300 μm powder. The powders were consolidated by a 5mm thick 303 SS flyer plate accelerated to 1.28 km/s. The effect of particle size on energy distribution and bond quality is being explored. The shot resulted in three sectors of seemingly well–bonded material (See Fig. 7.3). Uniform consolidation is demonstrated by the lack of flyer plate deformation, divider buckling, and retention of compact shape. Further examination showed incomplete interparticle bonding throughout the compacts, unrelated to the cavity dividers.

Zirconia powder shock transmitting media

A mixture of 10% Vol. 90 μm irregular SiC powder (Electro Abrasives 180 grit) and balance 10 μm Ti 6Al 4V alloy (Powder Metals Inc.) was pressed to a green shape shown in Fig. 7.4a under a static load of 150 MPa. The green compact was sufficiently strong to retain shape during careful handling. It was placed flat side up on a bed of –325 mesh zirconia powder (Cerac Z–1041), and more ZrO_2 powder was added to completely embed the green. The loaded target was covered with a 0.13mm thick 304 SS cover plate to retain the powder and then evacuated and impacted by a 5mm thick 303 SS plate at 1.0 km/s (Shot #59). The impact was sufficient to densify and bond the compact but not the zirconia. The resulting compact (Fig. 7.4b) is strained nearly uniaxially with 6% of uniform radial expansion. The radial expansion is caused by an insufficient packing density of the zirconia of only 47% (53% porosity), relative to the Ti + SiC, which is pressed to 59% of solid density.

7.3 Discussion

The three experiments described above each rely on a combination of rigid radial confinement and uniform strain in the shock direction to retain a one dimensional shock front. The effects of edge wave interactions at the rigid target and flyer plate edges are therefore of critical interest. Determining the extent of inter–cavity interactions is also important.

When a flyer plate strikes a porous media contained in a rigid fixture (and not the fixture itself), a plane shock wave is generated in the media, as well as a radial compression wave in the fixture at the powder–fixture interface. The pressure of the wave in the fixture at the interface is determined by the shock impedance match between the shocked powder and the fixture material and the geometric boundary conditions. It may be a considerable fraction of the shock pressure in the powder. Note that the pressure in the shocked powder is now being released to an intermediate level. The wave in the cylinder attenuates in both radial and longitudinal directions, and results in minimal (1%) expansion of the fixture in our experiments. The three–element interactions of the flyer plate, powder, and rigid cylinder have not been simulated in precisely the configuration used; however, flyer plate experiments conducted using a metallic glass powder have confirmed the retention of a well–defined, nearly planar consolidation front across the entire compact surface as discussed in Chapter 2. This suggests the edge wave dissipation is relatively minor in the geometry used.

The cavity to cavity interactions are more easily understood. Edge wave interactions between neighboring shocked regions proceed at an angle determined by Al'tshuler et al. [4]. Given a comparable shock speed and pressure, the angle is quite small and the interaction minor. In the case of rigid dividers, the shock impedance mismatch is large very close to the divider, but the shock state difference will dissipate over a length of several divider thicknesses as the shock waves in the divider ring down to the powder shock pressure.

The ceramic–composite shock impedance match affected the condition of the MMC part fabricated. Matching the shock properties of a ceramic and metal precisely proved quite difficult. We compromised by matching solid density and shock speed as closely as possible. The resulting compact has not been mechanically tested, but shows no signs of macroscopic cracking, buckling or bending. A careful porosity match would result in a uniform strain in the shock direction. The shock speed match prevents 'wrap–around' waves.

7.4 Conclusions

Three techniques have been demonstrated which maintain the plane wave condition in the shock wave used to consolidate powders. They are useful for the simultaneous consolidation of multiple samples. Valuable benefits of one dimensional consolidation include nearly uniform processing conditions for the compacts, and a simplified design and recovery of complex, near net shape parts from a single cylindrical target design. These techniques are also useful in the study of shock initiated chemical reactions in powder mixtures [5].

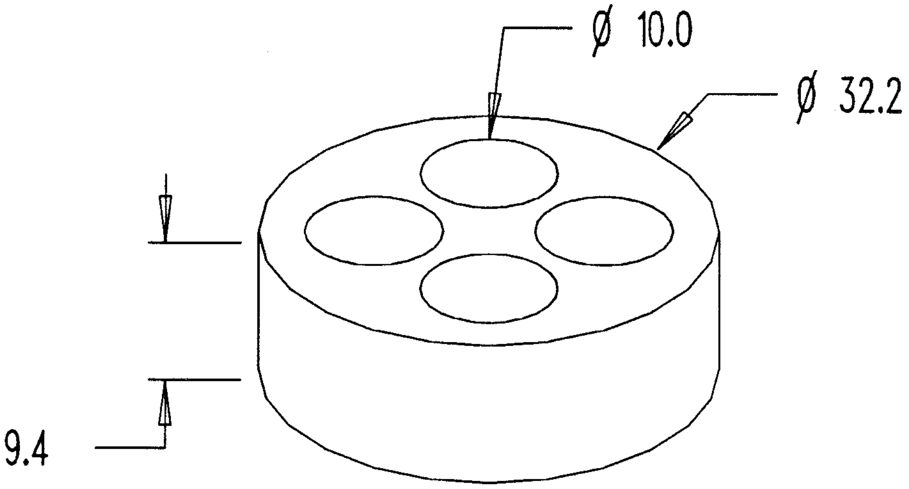

Fig. 7.1 Illustration of a four–cavity porous bronze target insert. The target ring used is illustrated in Fig. 2.5. All dimensions are in mm.

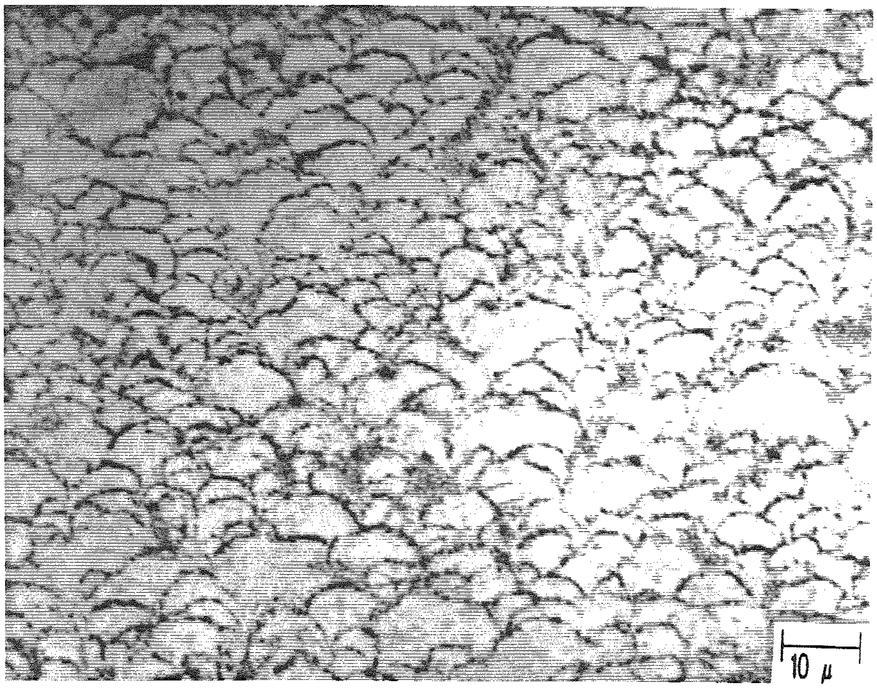

Fig. 7.2 Optical micrograph of polished and etched shock consolidated spiky spherical nickel powder, 5.5–6.5 μm particle size.

Fig. 7.3 Photograph of recovered M350 maraging steel sectors of shot #63. The three pieces did not bond strongly to the stainless steel divider sheets.

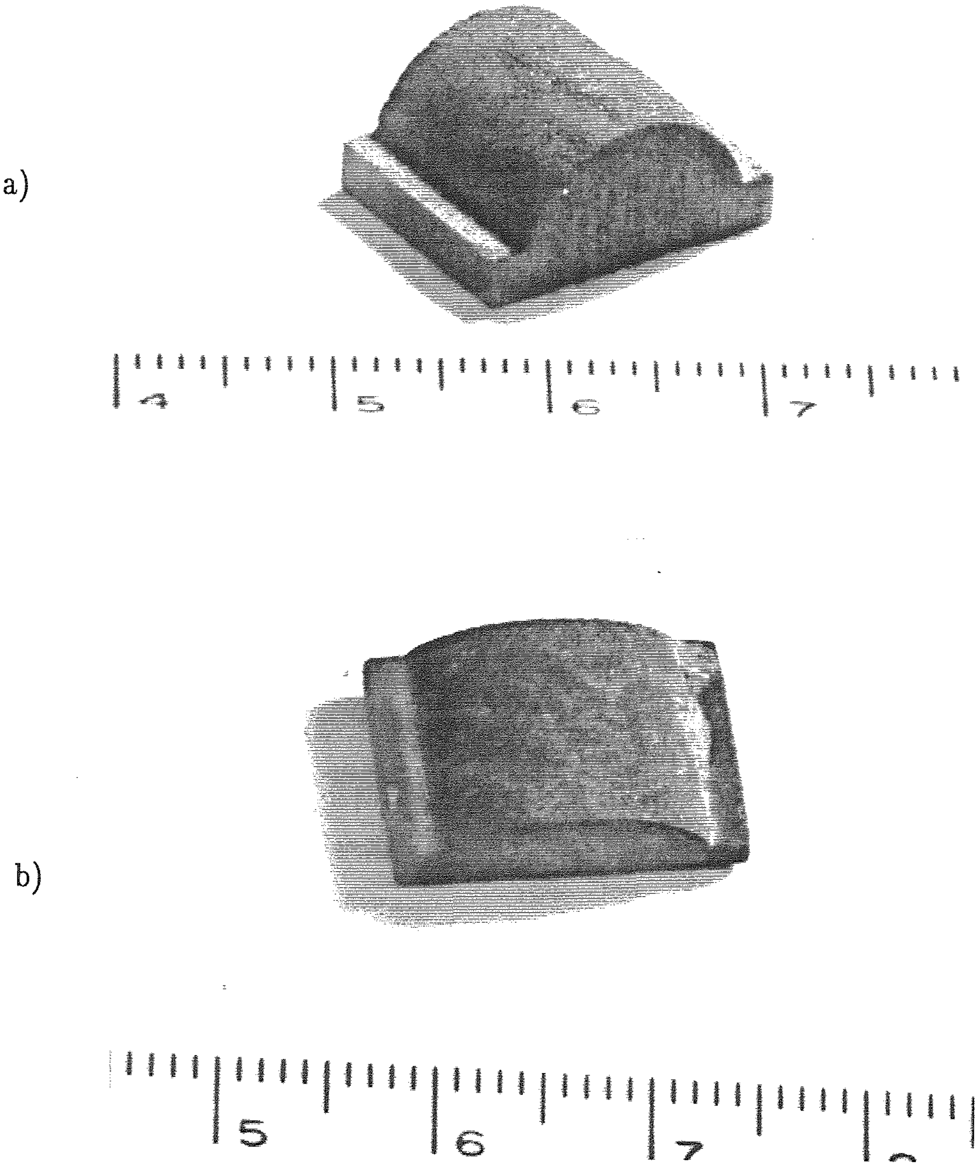

Fig. 7.4 Photograph of a) the pressed green compact of Ti + SiC, and b) the shock consolidated compact.

References

1. G. E. Korth, J. E. Flinn, and R. C. Green, in *Metallurgical Applications of Shock–Wave and High–Strain–Rate Phenomena*, edited by L. E. Murr, K. P. Staudhammer, and M. A. Meyers (Dekker, New York, 1986), p. 129.
2. R. A. Berry and R. L. Williamson, in *Metallurgical Applications of Shock Wave and High Strain Rate Phenomena* (Dekker, New York, 1986) p. 167.
3. P. S. Decarli and M. A. Meyers, *Shock Waves and High Strain Rate Phenomena in Metals*, edited by M. A. Meyers and L. E. Murr (Plenum, New York, 1981) p. 341.
4. L. V. Al'tschuler, S. B. Kormer, M. I. Brazhnik, L. A. Vladimirov, M. P. Speranskaya, and A. I. Funtikov, Sov. Phys. JETP. 11, 766 (1960).
5. B. R. Krueger and T. Vreeland Jr., in *Metallurgical Applications of Shock Wave and High Strain Rate Phenomena* (Dekker, New York, 1991 in press).

CHAPTER 8

CONCLUSIONS AND REMAINING ISSUES

Several diverse and disparate systems of materials and experimental techniques have been used to survey the effects of particle properties on energy deposition during shock consolidation. These efforts have born fruit in several quantitatively and qualitatively observed effects. The influence of particle size distribution in the case of spherical powders has been well established in the copper–constantan system. The influence of hardness in the mutual deformation of hardened and unhardened maraging steel has been observed. The localization of energy during the shock consolidation of a glass–forming alloy has been analyzed. Several interesting developments in the consolidation of multiple samples with uniaxial shock waves were made in the process of designing these experiments. Observing the success of these designs led to the development of a useful technique for consolidating a green compact to near net shape using a non–bonding pressure transmitting media.

Placing all of these experiments, conducted over an extended time, in a tightly organized framework (if possible) would create the illusion that a complete understanding of the shock consolidation process at the particle scale has been achieved, and the shock process rendered an accessible, reliable technology. This is a bit off the mark. Shock consolidation as a manufacturing process remains an uncertain proposition. In elemental metals and (most notably) in the nickel based superalloy Pyromet 718, considerable success has been achieved in shock consolidating well–bonded strong material. In seemingly similar systems, such as M350 maraging steel, good consolidation has been very difficult. The metallurgical root of this contrast is not clear.

On the other hand, several rays of light are visible. The Pyromet 718 not only bonded well, but showed enhancement over conventionally processed material. Post–shock annealing to remove residual stresses (and possible micro–cracks) proved highly effective. Irregular powders seem to bond more regularly; minimizing the non–deforming contact areas available during shock consolidation will aid bonding. A 'morning star' shaped spiked sphere is likely to be a nearly optimal shape for shock consolidation. A nickel powder produced using the carbonyl process has this morphology, and was consolidated easily. The built–in asperities are very highly deformed in consolidation. The use of a non–binding media, such as the zirconia powder used to embed the titanium + silicon carbide, showed the benefit of having a library of media which do not easily consolidate; it is likely to be a large library! Extending this concept is a highly viable path for scale–up of shock experiments.

This work leaves many issues open. Higher strain rate stress–strain experiments are needed to create an accurate thermal and deformation model. The relationship between particle shape and energy deposition is not resolved within a single material; producing a metallic glass forming alloy in spherical and irregular forms, and consolidating them in a multicavity planar shock target would facilitate such an experimental series. The role of surface contamination in stifling bonding has been noted [1], but quantitative analysis of the effect is not abundant. Given sufficient research in these areas, shock wave consolidation may prove to be a reliable manufacturing technique. It remains a very interesting method for exposing material to the extreme of deformation rates and pressures, and observing the unique results of these conditions.

References

1. T. Vreeland Jr., P. Kasiraj, and T. J. Ahrens, in *Mat. Res. Soc. Symp. Proc. Vol 28* (North Holland, New York, 1984) p. 139.

APPENDIX A

HUGONIOT: A PROGRAM FOR CALCULATING SHOCK CONDITIONS

```
OPTION BASE 0
DIM MATL(6, 14), NAM$(14), XX(30), YY(30), VAR$(2)
CLS
REM HUGONIOT; ANDREW MUTZ, 1984-90
REM   HUGONIOT INTERSECTION PROGRAM NOW WITH POWDER METAL CAPABILITY
REM
PRINT "   HUGONIOT INTERSECTION"
PRINT " PROGRAM TO DETERMINE THE IMPACT PARAMETERS IN A TARGET."
PRINT
DATA  8.9394, 3.933, 1.5, 3.94, 1.98, 7.3e-3
DATA  8.902, 4.59, 1.44, 4.523, 1.73, 5.7e-3
DATA 16.6786, 3.293, 1.307, 3.41, 1.6, .002
DATA 19.224, 4.029, 1.237, 4.03, 1.54, 3.2e-3
DATA 7.896, 4.569, 1.49,4.51, 2.17, .006
DATA 7.85, 3.574, 1.92, 4.57, 2.17, 6.0E-3
DATA 2.7069, 5.386, 1.339, 5.33,2.0, .013
DATA 2.785, 5.328, 1.338, 5.33,2.0, 1.3E-2
DATA 2.833, 5.041, 1.4200, 5.04, 2.1, 1.37E-2
DATA 2.48,5.22, 1.32, 5.22, 2.12, .0149
DATA 10.206, 5.124, 1.233, 5.12, 1.7, 3.5E-3
DATA 2.15, 1.84, 1.71, 2, 1.6, .0962
DATA 4.34, 4.94, .95, 6.16, 1.3, .00607
DATA 1.146, 2.201, .716, 2.53, 1.0, .13
DATA Copper, Nickel, Tantalum, Tungsten, 304 Stainless
DATA 1018 Iron, 1100 Aluminum, 2024 Aluminum, 921-T Aluminum
DATA Aluminum - 3% Li, Molybdenum, Teflon, Titanium, Nylon

FOR I = 1 TO 14
  FOR j = 1 TO 6
     READ MATL(j, I)
  NEXT j
NEXT I
LD = MATL(1, 14): LWS = MATL(2, 14): LCOEF = MATL(3, 14) 'Nylon BACKING
FOR I = 1 TO 14: READ NAM$(I): NEXT I
REM J=1 -- DENSITY, J=2 -- WAVE SPEED, J=3 -- COEFFICIENT OF PARTICLE VEL.
REM J=4 -- SOUND SPEED, J=5 -- GRUNEISON'S COEF., J=6 -- ISENTROPIC COMP.
Main: DO

  PRINT "THE FOLLOWING MATERIALS' PROPERTIES ARE BUILT IN:"
  PRINT "1:Cu, 2:Ni, 3:Ta, 4:W, 5:304 SS, 6:1018 Fe, 7:1100 Al, 8:2024 Al,";
  PRINT " 9: 921-T Al "
  PRINT "10: 3% Li Al , 11: Mo , 12:Teflon, 13:Titanium, 14:Nylon"
  PRINT
  PRINT " Of the materials listed, powder data is available for all but";
```

```
  PRINT " 3,5,7, and 11."
  PRINT "TO INPUT A MAT'L NOT LISTED, SPECIFY A "; 0; ", INSTEAD OF 1 - 13. "
   PRINT "TO INPUT A MAT'L from file MAT.DAT, SPECIFY 15 INSTEAD OF 0 - 14. "
  PRINT : PRINT
  INPUT "TARGET MATERIAL :  ", A
  IF A = 0 THEN
        INPUT " SPECIFY NAME OF TARGET MATERIAL : ", NAM$(0)
        INPUT " DENSITY OF MATL (g/cm3) : ", MATL(1, 0)
        INPUT " INTERCEPT OF SHOCK SPEED IN MATL (KM/S) : ", MATL(2, 0)
        INPUT " COEF OF SHOCK SPEED : ", MATL(3, 0)
        INPUT " GRUNEISON'S COEFFICIENT  : ", MATL(5, 0)
        INPUT "ISENTROPIC COMPRESSIBILITY  (GPa-1) : ", MATL(6, 0)
   END IF
   IF A = 15 THEN
            OPEN "mat.dat" FOR INPUT AS #1
            FOR j = 1 TO 6
                INPUT #1, MATL(j, 0)
            NEXT j
            INPUT #1, NAM$(0)
            CLOSE #1
            A = 0
   END IF
   IF A <= 15 THEN
        INPUT "Powder or Solid (P/S) : ", N$: M = 1
        IF N$ = "P" OR N$ = "p" THEN M$ = "powdered" ELSE M$ = "  solid"
   END IF

 LOOP WHILE A > 15

 TNAME$ = NAM$(A): PRINT "Target mat'l is "; M$; " "; TNAME$: PRINT
 TD = MATL(1, A): TWS = MATL(2, A): TCOEF = MATL(3, A)
 TSS = MATL(4, A): TG = MATL(5, A): TISE = MATL(6, A)
 IF N$ = "P" OR N$ = "p" THEN
  INPUT "Distension of powder, = (final density/initial density) = ", M
 END IF
FLYER: INPUT "FLYER  MATERIAL :  ", A
 IF A > 14 OR A < 0 THEN GOTO FLYER:
 IF A = 0 THEN
      INPUT " SPECIFY NAME OF FLYER  MATERIAL : ", BNAM$
      INPUT " DENSITY OF MATL (KG/M3) : ", FD
      INPUT " INTERCEPT OF SHOCK SPEED IN MATL (KM/S) : ", FWS
      INPUT " COEF OF SHOCK SPEED : ", FCOEF
      INPUT " SPEED OF SOUND IN MATL (KM/S) :", FSS
 ELSE
      BNAM$ = NAM$(A)
      PRINT "FLYER  MAT'L IS  "; BNAM$: PRINT
      FD = MATL(1, A): FWS = MATL(2, A): FCOEF = MATL(3, A)
      FSS = MATL(4, A)
 END IF

 INPUT "Flyer thickness in mm is : ", L
VelInput: INPUT "FLYER VELOCITY UPON IMPACT (KM/S) : ", VELFLY: PRINT
'hugoniot calc. function definitions
  DEF FNFLYHUG (U) = FD * (VELFLY - U) * (FWS + FCOEF * (VELFLY - U))
```

```
 DEF FNHUGINT (U)
  hugint1 = M * (1 + FNFLYHUG(U) * TISE) - 1
  hugint2 = 1 + (1 + TG / 2) * FNFLYHUG(U) * TISE
  FNHUGINT = U ^ 2 - FNFLYHUG(U) / TD * hugint1 / hugint2
 END DEF

500 IF N$ = "s" OR N$ = "S" THEN

 REM CALCULATE  PARTICLE VELOCITY IN TARGET for solid-solid collision
 A = FCOEF * FD - TCOEF * TD
 IF A = 0 THEN
   VELTAR = VELFLY / 2
 ELSE
   B = -FWS * FD - 2 * FCOEF * FD * VELFLY - TD * TWS
   C = VELFLY * (FWS * FD + FCOEF * FD * VELFLY)
   VELTAR = (-B - SQR(B * B - 4 * A * C)) / 2 / A
 END IF
 SHOCKVELT = TWS + TCOEF * VELTAR
 PRESS = VELTAR * SHOCKVELT * TD

ELSE 'Powder - Solid interaction

 REM iterate for the intersection of the flyer and target hugoniots
 U1 = VELFLY / 2: U2 = VELFLY * 5 / 6: F1 = FNHUGINT(U1): F2 = FNHUGINT(U2)
 FOR I = 1 TO 500
 ML = (F2 - F1) / (U2 - U1)
 UNEW = U2 - F2 / ML
 IF ABS(UNEW - U2) / U2 < VELFLY / 10000 THEN EXIT FOR
 U1 = U2: U2 = UNEW: F1 = F2: F2 = FNHUGINT(UNEW)
 NEXT I
 PRESS = FNFLYHUG(U2): VELTAR = U2
 SHOCKVELT1 = M ^ 2 * PRESS / TD * (1 + (1 + TG / 2) * PRESS * TISE)
 SHOCKVELT = SQR(SHOCKVELT1 / (M * (1 + PRESS * TISE) - 1))
 SHENERGY = PRESS * 1 / TD * (M - 1) / 2 * 1000'KJ/KG
END IF

 SHOCKVELF = PRESS / FD / (VELFLY - VELTAR)
 a2 = FD * FCOEF - LD * LCOEF
 IF a2 = 0 THEN a2 = 10 ^ -6
 B21 = FD * (FWS - 2 * (2 * VELTAR - VELFLY) * FCOEF)
 B2 = B21 + LD * (LWS + 2 * VELFLY * LCOEF)
 C21 = -FD * (2 * VELTAR - VELFLY) * (FWS - FCOEF * (2 * VELTAR - VELFLY))
 C2 = C21 - LD * (VELFLY * (LWS + VELFLY * LCOEF))
 VFLY2 = (-B2 + SQR(B2 ^ 2 - 4 * a2 * C2)) / 2 / a2
 VF3INT = 2 * VFLY2 - (2 * VELTAR - VELFLY)
 AI = TCOEF
 BI = -TSS - 2 * TCOEF * VELTAR
 CI = -PRESS / TD + VELTAR * (TSS + VELTAR * TCOEF)
 VT2INT = (-BI - SQR(BI ^ 2 - 4 * AI * CI)) / 2 / AI
 TIMEB = L / (SHOCKVELF * FSS) * (FSS + SHOCKVELF + VELTAR - VELFLY)
 A3 = FCOEF * FD - TCOEF * TD
 IF A3 = 0 THEN
   VTAR2 = VFLY2
 ELSE
```

```
        B31 = -FWS * FD - 2 * FCOEF * FD * VF3INT
        B3 = B31 - TD * TWS + 2 * TD * VT2INT * TCOEF
        C31 = VF3INT * FD * (FWS + FCOEF * VF3INT)
        C3 = C31 + TD * VT2INT * (TWS - TCOEF * VT2INT)
        VTAR2 = (-B3 - SQR(B3 * B3 - 4 * A3 * C3)) / 2 / A3
    END IF
    SVELT2 = TWS + TCOEF * (VELTAR - VTAR2)
    LSHOCKED1 = (SVELT2 + 2 * VELTAR) / (SVELT2 + VELTAR - SHOCKVELT)
    LSHOCKED = LSHOCKED1 * TIMEB * SHOCKVELT / M
    SVELF2 = FSS + (VFLY2 - VTAR2) * FCOEF
    PRESS2 = FD * (VF3INT - VTAR2) * (FWS + FCOEF * (VF3INT - VTAR2))

'Output Results
    CLS
    PRINT "    TARGET "; M$; " "; TNAME$, "     FLYER "; BNAM$
    PRINT
    IF N$ = "p" OR N$ = "P" THEN
        PRINT "DISTENSION  "; M, "           "; "1"
    END IF
    PRINT "DENSITY     "; TD, "           "; FD
    PRINT "WAVE SPEED  "; TWS, "           "; FWS
    PRINT "SHOCK COEFF."; TCOEF, "           "; FCOEF
    IF N$ = "P" OR N$ = "p" THEN
        PRINT "ISENTR. COM."; TISE, "           "; "--"
        PRINT "GRUN. COEFF."; TG, "           "; "--"
    END IF
    PRINT : PRINT "FLYER VELOCITY AT IMPACT   "; VELFLY; "KM/S"
    PRINT "FLYER THICKNESS  "; L; " mm.": PRINT
    PRINT " PARTICLE VELOCITY IN THE TARGET   "; VELTAR; "KM/S"
    PRINT " SHOCK VELOCITY IN THE TARGET      "; SHOCKVELT; "KM/S"
    PRINT " PRESSURE OF THE SHOCK WAVE        "; PRESS; "GPa"
    PRINT " PRESSURE OF THE RELEASE WAVE      "; PRESS2; "GPa"
    IF N$ = "P" OR N$ = "p" THEN
        PRINT " SHOCK ENERGY IN THE TARGET        "; SHENERGY; "kJ/kG"
        PRINT " RELEASE WAVE CATCHES SHOCK WAVE AT "; LSHOCKED;
        PRINT "mm IN SHOCKED TARGET."
    END IF
    PRINT : PRINT
    IF N$ = "P" OR N$ = "p" THEN
        INPUT "Display the Time-Displacement diagram? (Y/N) :", YD$
        IF YD$ = "Y" OR YD$ = "y" THEN GOSUB 1300 ELSE PRINT
    END IF
    IF N$ = "P" OR N$ = "p" THEN
        INPUT "Display the Pressure - Particle Velocity diagram? (Y/N) :", YD$
        IF YD$ = "Y" OR YD$ = "y" THEN GOSUB 1500 ELSE PRINT
    END IF
    INPUT " Calculate with same materials and new velocity? (Y/N) ", Y$
    IF Y$ = "Y" OR Y$ = "y" THEN GOTO VelInput
    INPUT " Calculate with new matls? (Y/N) ", Y$
    IF Y$ = "Y" OR Y$ = "y" THEN
        CLS
        GOTO Main
    END IF
END
```

```
1300 '******** DISPLACEMENT VS. TIME GRAPHICS ************
     'CALCULATE THE X-T  PAIRS TO BE GRAPHED
     XA = (VELFLY - SHOCKVELF) * L / SHOCKVELF: TA = L / SHOCKVELF
     TB = L / SHOCKVELF / SVELF2 * (SVELF2 + SHOCKVELF + VELTAR - VELFLY)
     XB = TB * VELTAR
     XC1 = (SVELT2 + 2 * VELTAR) / (SVELT2 + VELTAR - SHOCKVELT)
     XC = XC1 * TB * SHOCKVELT
     TC = XC / SHOCKVELT
     XD1 = 1 / (1 / (-SVELF2 + VFLY2) - 1 / VFLY2)
     XD = XD1 * (TA - TB + XB / (-SVELF2 + VFLY2) - XA / VFLY2)
     TID = (XD - XA) / VFLY2 + TA
     XMIN = -INT(.5 * (L + VELFLY + 2.5)) * 2
     YMAX = INT((TID + TC) / 2 + ABS(TID - TC) / 2 + 1.5) + 1
     YMIN = -1: XMAX = INT(.5 * (XC + 1.5)) * 2
     DLTX = INT((XMAX - XMIN) / 8 + 1)
     XMAX = XMAX + DLTX - (XMAX - XMIN) MOD DLTX: DLTPX = DLTX
     IF YMAX < 3 THEN DLTY = .5 ELSE DLTY = INT((YMAX - YMIN) / 6 + 1)
     YMAX = YMAX + DLTY - (YMAX - YMIN) MOD DLTY: DLTPY = DLTY
     TIT$ = "COLLISION OF FLYER WITH  TARGET"
     VAR$(0) = "DISTANCE (mm) ": VAR$(1) = "TIME (microsec)"
     XX(1) = XD: XX(2) = XB: XX(3) = XC: XX(4) = 0: XX(5) = XA: XX(6) = XB
     YY(1) = TID: YY(2) = TB: YY(3) = TC: YY(4) = 0: YY(5) = TA: YY(6) = TB
     NNVAR = 2: NAX = 6: ITICK = 1: IDASH = 0
    GOSUB 10000
    GOSUB 10760
     XX(1) = XD: XX(2) = XA: XX(3) = -L - VELFLY: YY(1) = TID: YY(2) = TA
     YY(3) = -1: NAX = 3: IDASH = 20
    GOSUB 10760
     XX(1) = XB + VTAR2 * (TID - TB): XX(2) = XB: XX(3) = 0: XX(4) = -VELFLY
     YY(1) = TID: YY(2) = TB: YY(3) = 0: YY(4) = -1
     NAX = 4: IDASH = 20
    GOSUB 10760
     INPUT " ", NONS$
     SCREEN 0: CLS
     RETURN
1500 '******** PRESSURE VS. VELOCITY GRAPHICS ************
    'CALCULATE THIRTY POINTS FOR THE POWDER COMPRESSION HUGONIOT
    FOR I = 1 TO 30  'PRESSURE = (I-1)/20 * PRESS
    PR = (I - 1) / 20 * PRESS: YY(I) = PR
    XX1 = PR / TD * (M * (1 + PR * TISE) - 1)
    XX(I) = SQR(XX1 / (1 + (1 + TG / 2) * PR * TISE))
    NEXT I
    'SPECIFY GRAPHICS PARAMETERS FOR LLPLOT
    XMIN = 0: XMAX = INT(VELFLY + 1)
    IF XMAX > 4 THEN DLTX = 1 ELSE DLTX = .5
    YMIN = 0: YMAX = INT((PRESS * 1.5 + 1.5)): DLTY = INT((YMAX + 6) / 6)
    YMAX = YMAX + DLTY - YMAX MOD DLTY
    DLTPX = DLTX: DLTPY = DLTY: NNVAR = 2: NAX = 30: ITICK = 0: IDASH = 0
    TIT$ = "COLLISION OF FLYER WITH TARGET"
    VAR$(0) = "VELOCITY (km/s) ": VAR$(1) = "PRESSURE (GPa) "
  GOSUB 10000
  GOSUB 10760
    'CALCULATE POINTS FOR FLYER HUGONIOT
    FOR I = 1 TO 9
```

```
    PR = (I - 1) / 6 * PRESS: YY(I) = PR
    XX1 = (-FWS + SQR(FWS ^ 2 + 4 * PR / FD * FCOEF)) / 2 / FCOEF
    XX(I) = VELFLY - XX1
  NEXT I
  NAX = 9
GOSUB 10760
  'CALCULATE POINTS FOR RELEASE OF FLYER TO LEXAN BACKING
  FOR I = 1 TO 7
    XX(I) = VFLY2 + (I - 1) / 6 * (VELTAR - VFLY2)
    YY1 = FD * (XX(I) - 2 * VELTAR + VELFLY)
    YY(I) = YY1 * (FWS + FCOEF * (XX(I) - 2 * VELTAR + VELFLY))
  NEXT I
  NAX = 7
GOSUB 10760
  'Calculate points for arrival of flyer release wave on compacted powder
  'parametrize on velocity this time
  FOR I = 1 TO 5
  VEL = (I - 1) * (VTAR2 - VFLY2) / 4 + VFLY2: XX(I) = VEL
  YY(I) = FD * (VF3INT - VEL) * (FWS + FCOEF * (VF3INT - VEL))
  NEXT I
  NAX = 5
GOSUB 10760
  FOR I = 1 TO 7
  VEL = (I - 1) * (VELTAR - VTAR2) / 6 + VTAR2: XX(I) = VEL
  YY(I) = TD * (VEL - VT2INT) * (TWS + TCOEF * (VEL - VT2INT))
  NEXT I
  NAX = 7
GOSUB 10760
  'CALCULATE POINTS FOR LEXAN HUGONIOT
  FOR I = 1 TO 9
  VEL = (I - 1) / 6 * (VFLY2 - VELFLY) + VELFLY: XX(I) = VEL
  YY(I) = LD * (VELFLY - VEL) * (LWS + LCOEF * (VELFLY - VEL))
  NEXT I
  NAX = 9
GOSUB 10760
  INPUT " ", NON$: CLS
RETURN

10000 '*********************** SUBROUTINES "LLPLOT" ***********************
     '
     '     Log or Linear Diagram, Plotting, & Screen Printout Subroutines
     '
     'Nomenclature
     'X           Horizontal Axis Variable
     'Y           Vertical Axis Variable
     '
     'The Following Variables Must be defined when the subroutines are called:
     '
     'DLTX & DLTY          Scale intervals between printed values along the
     '              X & Y axes
     'DLTPX & DLTPY          Scale intervals between scale points along the
     '              X & Y axes
     'XMIN & XMAX          Minimum & maximum values of the x axis variable
     'YMIN & YMAX          Minimum & maximum values of the Y axis variable
```

```
'NAX+1              No. of computed points of the diagram
'XX(NAX+1),YY(NAX+1)  Arrays where computed points of the diagram
'                  are stored
'TIT$              String variable containing the diagram title
'VAR$(NVAR)             String variable containing the variable names
'NNVAR              Dimension of the array VAR$
'VAR$(0)            X axis variable name
'VAR$(i)            Y axis variable name, for i=1 to NNVAR
'ILOG               =1 for a log (base 10) plot, YMAX & YMIN
'                  must be input as logs of the max and min Y's
'                  and YY values are logs (LOG(YMAX)/LOG(10),etc)
'ITICK              =1 for internal grid of ticks
'IDASH               =0 FOR Continuous line, 8 - 50 for dashed lines
'
'**************** Diagram Frame & Axes Subroutine ********************
'
'Read Visualization Parameters & Plotting Data
NPX = 525           'No. of pixels in the diagram along the X axis
NSX = 50            'No. of pixels of the side edge
NPY = 280           'No. of pixels in the diagram along the Y axis
NSY = 60            'No. of pixels of the lower edge
'
SCREEN 9
'...Draw figure frame & axes...
CLS : LINE (NSX, 350 - NSY - NPY)-(NSX, 350 - NSY)
LINE (NSX + NPX, 350 - NSY)-(NSX + NPX, 350 - NSY - NPY)
LINE (NSX, 350 - NSY)-(NPX + NSX, 350 - NSY)
LINE (NSX, 350 - NSY - NPY)-(NSX + NPX, 350 - NSY - NPY)
'
'...Set unit points on the x axis...
IHMAX = 5: JHMAX = 5
IMAX = INT((XMAX - XMIN) / DLTPX + .5)
JMAX = INT((YMAX - YMIN) / DLTPY + .5)
FOR I = 0 TO IMAX
 IX = INT(I * DLTPX * NPX / (XMAX - XMIN) + .5)
 FOR JY = 1 TO 3: PSET (NSX + IX, 350 - NSY - JY): NEXT
NEXT
FOR j = 0 TO JMAX
  JY = INT(j * DLTPY * NPY / (YMAX - YMIN) + .5)
  FOR IX = 1 TO 5: PSET (NSX + IX, 350 - NSY - JY): NEXT
NEXT
IMAX = INT((XMAX - XMIN) / DLTX + .5)
JMAX = INT((YMAX - YMIN) / DLTY + .5)
FOR I = 0 TO IMAX
 IX = INT(I * DLTX * NPX / (XMAX - XMIN) + .5)
 XVAL = XMIN + I * DLTX
 YROW = INT((350 - NSY) / 8 + 2.5)
 XCOL = INT((NSX + IX) / 8 - LEN(CHR$(ABS(XVAL))) / 2 + .5)
 LOCATE YROW, XCOL: PRINT XVAL;
NEXT

YVAL = RMNP / 10          'TO BE CHANGED FOR LOG AND LINEAR PLOTS
FOR j = 0 TO JMAX
 JY = INT(j * DLTY * NPY / (YMAX - YMIN) + .5)
```

```
      IF ILOG = 1 THEN YVAL = 10 * YVAL ELSE YVAL = YMIN + j * DLTY
      YROW = INT((350 - NSY - JY) / 9 + 1): XCOL = 1
      LOCATE YROW, XCOL
      PRINT YVAL
    NEXT
    IMAX = INT((XMAX - XMIN) / DLTPX + .5)
    JMAX = INT((YMAX - YMIN) / DLTPY + .5)
'Ticks on the axes if itick < >0
    IF ITICK < > 0 THEN
      FOR j = 0 TO JMAX - 1
        JY = INT(j * DLTPY * NPY / (YMAX - YMIN) + .5)
        FOR I = 0 TO IMAX - 1
          FOR IH = 0 TO IHMAX
            IX = INT((I + IH / IHMAX) * DLTPX * NPX / (XMAX - XMIN) + .5)
                      PSET (NSX + IX, 350 - NSY - JY)
          NEXT
        NEXT
      NEXT
      FOR I = 0 TO IMAX - 1
        IX = INT(I * DLTPX * NPX / (XMAX - XMIN) + .5)
        FOR j = 0 TO JMAX - 1
          FOR JH = 0 TO JHMAX
            JY = INT((j + JH / JHMAX) * DLTPY * NPY / (YMAX - YMIN) + .5)
            PSET (NSX + IX, 350 - NSY - JY)
          NEXT
        NEXT
      NEXT
    END IF

    FOR j = 0 TO JMAX - 1
      JY = INT(j * DLTPY * NPY / (YMAX - YMIN) + .5)
      PSET (NSX + NPX, 350 - NSY - JY): DRAW "L8":
    NEXT j
    FOR I = 0 TO IMAX - 1
      IX = INT(I * DLTPX * NPX / (XMAX - XMIN) + .5)
      PSET (NSX + IX, 350 - NSY - NPY): DRAW "D3":
    NEXT I
    '         2         4         6         8         10
    '...Print the title & variable names...
    LOCATE 43, 10: PRINT TIT$;
    YROW = INT((350 - NSY) / 8 + 3.5)
    XCOL = INT((NSX + NPX * .9) / 8 + .5)
    LOCATE YROW, XCOL: PRINT VAR$(0);
    FOR I = 1 TO NNVAR
      LOCATE INT((350 - NSY - NPY) / 9 + 3 + 2 * (I - 1)), 1
      PRINT VAR$(I);
    NEXT
    RETURN

10760 '********************** Plotting Subroutine *****************************
    '
    'Can be called more than once to plot several curves in the same diagram
    '
    'Set points in the diagram
```

```
 I = 1
 IXO = INT((XX(I) - XMIN) * NPX / (XMAX - XMIN) + .5)
 JYO = INT((YY(I) - YMIN) * NPY / (YMAX - YMIN) + .5)
FOR I = 2 TO NAX
 IX = INT((XX(I) - XMIN) * NPX / (XMAX - XMIN) + .5)
 JY = INT((YY(I) - YMIN) * NPY / (YMAX - YMIN) + .5)
 IF JY >= 0 AND JY <= NPY AND JYO >= 0 AND JYO <= NPY THEN
  LINE (NSX + IX, 350 - NSY - JY)-(NSX + IXO, 350 - NSY - JYO)
  IF IDASH <> 0 THEN
      XBEG = NSX + IX: YBEG = 350 - NSY - JY: XEND = NSX + IXO
      YEND = 350 - NSY - JYO
      GOSUB 11370
  END IF

 ELSEIF JYO >= 0 AND JY < 0 THEN
  JYB = 0: IXB = IXO + INT((JYB - JYO) * (IX - IXO) / (JY - JYO) + .5)
  LINE (NSX + IXO, 350 - NSY - JYO)-(NSX + IXB, 350 - NSY - JYB)
  IF IDASH <> 0 THEN
      XBEG = NSX + IXO: YBEG = 350 - NSY - JYO
      XEND = NSX + IXB: YEND = 350 - NSY - JYB
      GOSUB 11370
  END IF

 ELSEIF JYO > NPY AND JY <= NPY THEN
  JYB = NPY: IXB = IXO + INT((JYB - JYO) * (IX - IXO) / (JY - JYO) + .5)
  LINE (NSX + IXB, 350 - NSY - JYB)-(NSX + IX, 350 - NSY - JY)
  IF IDASH <> 0 THEN
      XBEG = NSX + IXB: YBEG = 350 - NSY - JYB
      XEND = NSX + IX: YEND = 350 - NSY - JY
      GOSUB 11370
  END IF


 ELSEIF JYO < 0 AND JY >= 0 THEN
  JYB = 0: IXB = IXO + INT((JYB - JYO) * (IX - IXO) / (JY - JYO) + .5)
  LINE (NSX + IX, 350 - NSY - JY)-(NSX + IXB, 350 - NSY - JYB)
  IF IDASH <> 0 THEN
      XBEG = NSX + IX: YBEG = 350 - NSY - JY
      XEND = NSX + IXB: YEND = 350 - NSY - JYB
      GOSUB 11370
  END IF


 ELSEIF JYO <= NPY AND JY > NPY THEN
  JYB = NPY: IXB = IXO + INT((JYB - JYO) * (IX - IXO) / (JY - JYO) + .5)
  LINE (NSX + IXO, 350 - NSY - JYO)-(NSX + IXB, 350 - NSY - JYB)
  IF IDASH <> 0 THEN
      XBEG = NSX + IXO: YBEG = 350 - NSY - JYO
      XEND = NSX + IXB: YEND = 350 - NSY - JYB
      GOSUB 11370
  END IF

 ELSEIF JYO < 0 AND JY > NPY THEN
  JYB = 0: IXB1 = IXO + INT((JYB - JYO) * (IX - IXO) / (JY - JYO) + .5)
```

```
      JYB = NPY
      IXB2 = IXO + INT((JYB - JYO) * (IX - IXO) / (JY - JYO) + .5)
      LINE (NSX + IXB1, 350 - NSY)-(NSX + IXB2, 350 - NSY - NPY)
      IF IDASH < > 0 THEN
            XBEG = NSX + IXB1: YBEG = 350 - NSY
            XEND = NSX + IXB2: YEND = 350 - NSY - NPY
            GOSUB 11370
      END IF

    ELSEIF JYO > NPY AND JY < 0 THEN
      JYB = NPY
      IXB1 = IXO + INT((JYB - JYO) * (IX - IXO) / (JY - JYO) + .5)
      JYB = 0
      IXB2 = IXO + INT(((JYB - JYO) * (IX - IXO) / (JY - JYO) + .5))
      LINE (NSX + IXB1, 350 - NSY - NPY)-(NSX + IXB2, 350 - NSY)
      IF IDASH < > 0 THEN
             XBEG = NSX + IXB1: YBEG = 350 - NSY - NPY
             XEND = NSX + IXB2: YEND = 350 - NSY
             GOSUB 11370
      END IF
    END IF
    IXO = IX: JYO = JY
  NEXT I
  RETURN
    '
    '
    '***************** Plot data points as CROSSES subroutine *************
11250 '
    FOR I = 1 TO NAX
          IX = INT((XX(I) - XMIN) * NPX / (XMAX - XMIN) + .5)
          JY = INT((YY(I) - YMIN) * NPY / (YMAX - YMIN) + .5)
     IF XX(I) > = XMIN AND XX(I) < = XMAX THEN
      IF YY(I) > = YMIN AND YY(I) < = YMAX THEN
        PSET (NSX + IX, 350 - NSY - JY): AAA$ = "R2L4R2U1D2": DRAW AAA$
      END IF
     END IF
    NEXT I
    RETURN
    '
    '
    '************** Convert solid lines to dashed lines (from line routine)
11370 ' Dashes a line from (XBEG,YBEG) TO (XEND,YEND)
    IF XBEG - XEND = 0 THEN
     LLEN = 16 / 7 * ABS(YEND - YBEG)
     XPROP = 0: YPROP = 7 / 16
    ELSE
     SLOPE = (YBEG - YEND) / (XBEG - XEND)
     LLEN = SQR((XBEG - XEND) ^ 2 + ((YBEG - YEND) * 16 / 7) ^ 2)
     XPROP = SQR(1 / (1 + SLOPE ^ 2 * (16 / 7) ^ 2))
     IF SLOPE = 0 THEN YPROP = 0
     IF SLOPE < > 0 THEN
         YPROP = SQR(1 / (1 + (SLOPE * 16 / 7) ^ -2)) * 7 / 16
     END IF
    END IF
```

```
IF XBEG > XEND THEN XPROP = -XPROP
IF YEND < YBEG THEN YPROP = -YPROP
FOR j = 1 TO LLEN STEP IDASH
 CIRCLE (INT(XBEG + j * XPROP + .5), INT(YBEG + j * YPROP + .5)), 2, 0
 CIRCLE (INT(XBEG + j * XPROP + .5), INT(YBEG + j * YPROP + .5)), 1
 PAINT (INT(XBEG + j * XPROP + .5), INT(YBEG + j * YPROP + .5)), 0
NEXT j
RETURN
```

APPENDIX B

THERCO: A PROGRAM FOR 1–D SIMULATION OF A THERMOCOUPLE

```
'A one dimensional shock wave thermal model simulation with two solid materials
'heat is deposited into a discretized system of masses w/connected interiors
' A. Mutz      10-2-90
DECLARE SUB TEXTPRINT (text$, X!, Y!, iflag%)
DECLARE SUB AXES (xmin!, xmax!, DLTX!, DLTPX!, ymin!, ymax!, DLTY!, DLTPY!, ITICK%,
            JLOG%, TIT$, VAR$())
DECLARE SUB PLOT (iplot%, nax%, xmin!, xmax!, ymin!, ymax!, X!(), Y!())
DECLARE SUB MIX (bwidth, nax%, TC!())
DECLARE SUB TILT (bwidtht, nax%, TC!())
 SCREEN 9
DEFINT I-J, M-N
 DIM T(102), TC(2002), Ti(102), TP(102)'TEMPERATURE ARRAY
 DIM xx(2003), yy(2003), a(2), B(2), VAR$(2)'GRAPHICS ARRAYS
 PRINT "MATERIAL 1 NAME  : "; "Copper"; " Material 2 Name  :"; "Constantan"
 x0$ = "75."  'Material 1 Thickness in microns
 x1$ = "25."  'Material 2 Thickness in microns
 x2$ = "185000."  'Shock energy in J/kg
 x3$ = "20."  'initial temperature of material 1
 x4$ = "20." 'initial temperature of material 2
 x5$ = "8.9"
 x6$ = "8.9"
 T0 = VAL(x3$)
 T1 = VAL(x4$)
 Energy = VAL(x2$)
 ETHE = Energy / 1000
 Roel = VAL(x5$) * 1000
 ROES = VAL(x6$) * 1000
 'L = 204 J/g, Cp = 0.35 J/gK, delTMelt = 588 K
 delTMelt = 588
 'CONVERT ALL TO STANDARD K,M,S,J UNITS, AFTER PRINTING
 PRINT "Material 1 Thickness (um)             ("; VAL(x0$); ") : "
 r0 = VAL(x0$) * .000001
 PRINT "Material 2 Thickness (um)             ("; VAL(x1$); ") : "
 r1 = VAL(x1$) * .000001
 x1$ = "1.11"    'Material 1 diffusivity  cm2/s
 x2$ = ".101     Material 2 thermal diffusivity"
 x3$ = ".385"    'Material 1 conductivity kJ/msK
 x4$ = ".035 "    'Material 2 conductivity
 x5$ = "20."
 x6$ = "1250."
 PRINT "Material 1 THERMAL DIFFUSIVITY (CM2/S)   ("; VAL(x1$); ") : "
 ALL = VAL(x1$) * .0001
 PRINT "Material 2 THERMAL DIFFUSIVITY (CM2/S)   ("; VAL(x2$); ") : "
 ALR = VAL(x2$) * .0001
```

```
PRINT "Material 1 THERMAL CONDUCTIVITY (KJ/MSK)  ("; VAL(x3$); ") :"
Kl = VAL(x3$) * 1000
PRINT "Material 2 THERMAL CONDUCTIVITY (KJ/MSK) ("; VAL(x4$); ") : "
KR = VAL(x4$) * 1000
TM = VAL(x6$)
nmax = 60
nmid = CINT(r0 / (r0 + r1) * nmax + 1)'THE FIRST NODE OF MATERIAL 2
RM = 0: rm1 = 0: rm2 = 0
rpart = .000049 'particle radius in material 0
rpart1 = .00002
Vsh = 1500 ' shock velocity in MKS
dr = (r0 + r1) / nmax'INCREMENT OF Thickness, WITH Fixed temp  ON THE ENDS.
DT = .0000000005# 'TIME INCREMENT IN S
RS = ALR / dr ^ 2 * DT
LS = ALL / dr ^ 2 * DT
po = .5    'relative mass of outer shell to inner shell
fract = 1 - (1 / (1 + po)) ^ .33333333#' fraction of distance from
                                    'outer rad. to inner shell rad.
Lbeta = ALL / fract ^ 2 / rpart ^ 2 / po * DT / 4
Lgamma = ALL / fract ^ 2 / rpart ^ 2 * DT / 4
Rbeta = ALR / fract ^ 2 / rpart1 ^ 2 / po * DT / 4
Rgamma = ALR / fract ^ 2 / rpart1 ^ 2 * DT / 4
ShWidth = rpart / Vsh 'rise time of shock wave in material
ShWidth1 = rpart1 / Vsh
iwidth = CINT(ShWidth / DT) 'number of time steps in shock rise time
iwidth1 = CINT(ShWidth1 / DT)
ivel = CINT(1 / Vsh / DT * dr)' number of distance steps per time step Sh Vel.
delt = Energy / Kl * ALL * Roel * (po + 1) / po / iwidth
IF rpart > rpart1 THEN ipart = CINT(rpart / dr) ELSE ipart = CINT(rpart1 / dr)

'initialize temperature  profile--  **.*****.**.*****;**.*****.**.*****

FOR i = 0 TO nmax
    T(i) = 20
    Ti(i) = 20 ' TEMPERATURES at t = 0
NEXT i

REM SET UP GRAPHICS

xmax = 1000000 * (r1 + r0): ymin = 0: ymax = 1400: DLTY = 100: DLTPY = DLTY
nax = 60: NNVAR = 2: DLTX = xmax / 5: DLTPX = DLTX: xmin = 0:
TIT$ = "INITIAL CONDITION": VAR$(0) = "DEPTH": VAR$(1) = "TEMP": ITICK = 1
i$ = ""    'pause for keystroke
a(1) = 1000000! * r0: a(2) = 1000000! * r0
B(1) = ymin + .9 * (ymax - ymin): B(2) = ymin

CALL AXES(xmin, xmax, DLTX, DLTPX, ymin, ymax, DLTY, DLTPY, ITICK, JLOG, TIT$, VAR$())

FOR ii = 1 TO nax: xx(ii) = dr * (ii - 1) * 1000000: NEXT ii
FOR c = DT TO .0000018 STEP DT' TIME in 1 ns steps
     nc = CINT(c / DT)

    IF c < = (r0 + r1 + rpart) / Vsh THEN 'add heat
        ShPosnF = Vsh * c
```

```
        iShPosnF = CINT(ShPosnF / dr)
        ShPosnR = Vsh * c - rpart
        iShPosnR = CINT(ShPosnR / dr)
        OutC = .7
        KinC = (1 - OutC)
        FOR i = 0 TO nmid - ipart - 1
           IF i > iShPosnR AND i <= iShPosnF THEN
              T(i) = T(i) + delt * OutC
              Ti(i) = Ti(i) + delt * po * KinC
           END IF
        NEXT i
        IF nmid - ipart < 0 THEN incr = nmid ELSE incr = ipart
        FOR i = nmid - incr TO nmid - 1
           IF i > iShPosnR AND i <= iShPosnF THEN
              Conc = -CSNG(i - nmid + ipart) / ipart / 2
              T(i) = T(i) + delt * OutC * (1 + .5 * Conc)
              Ti(i) = Ti(i) + delt * po * KinC * (1 + .5 * Conc)
           END IF
        NEXT i
        IF ipart > nmax - nmid THEN incr = nmax - nmid ELSE incr = ipart
        FOR i = nmid TO nmid + incr
           IF i > iShPosnR AND i <= iShPosnF THEN
              Conc = -CSNG(i - nmid - ipart) / ipart / 2
              T(i) = T(i) + delt * OutC * (1 + .5 * Conc)
              Ti(i) = Ti(i) + delt * po * KinC * (1 + .5 * Conc)
           END IF
        NEXT i
        FOR i = nmid + incr + 1 TO nmax
           IF i > iShPosnR AND i <= iShPosnF THEN
              T(i) = T(i) + delt * OutC
              Ti(i) = Ti(i) + delt * po * KinC
              END IF
        NEXT i

     END IF

     IF nc MOD 20 = 1 THEN
       GOSUB 1440 ' CALCULATE TOTAL ENERGY IN PARTICLE
       LINE (xmin + .002 * (xmax - xmin), ymax * .998)-
           (xmax * .998, ymin + .002 * (ymax - ymin)), 0, BF
       LOCATE 4, 40: PRINT "Time "; c; : LOCATE 5, 40
       PRINT "ECALC "; ETOT; : LOCATE 6, 40
       PRINT "ETOT  "; ETHE; : LOCATE 7, 40:
       LOCATE 4, 20: PRINT "Cu": LOCATE 4, 60: PRINT "Co"
       FOR ii = 1 TO nax: yy(ii) = T(ii - 1): NEXT ii
       CALL PLOT(iplot, nax - 1, xmin, xmax, ymin, ymax, xx(), yy())
       CALL PLOT(0, 1, xmin, xmax, ymin, ymax, a(), B())
     END IF
WHILE i$ = ""
   i$ = INKEY$
WEND
     'Boundary conditions with half lumps on the ends and no flow
     Told = T(0)
     T(0) = Told + 2! * LS * (T(1) - Told) + Lbeta * (Ti(0) - Told)'LEFT BC
```

```
        Ti(0) = Ti(0) + Lgamma * (Told - Ti(0))
        Told = T(nmax)
        ' right bc
        T(nmax) = Told + 2! * (T(nmax - 1) - Told) * RS + Rbeta * (Ti(nmax) - Told)
        Ti(nmax) = Ti(nmax) + Rgamma * (Told - Ti(nmax))

        GOSUB 960      'DIFFEQ PUSHER
        IF nc MOD 2 = 0 THEN
            Tnmid = T(nmid) + .5 * (T(nmid) - T(nmid + 1))
            Tnm1 = T(nmid - 1) + .5 * (T(nmid - 1) - T(nmid - 2))
            TC(nc / 2) = (Tnm1 + Tnmid) / 2
        END IF
    NEXT c
  bwidth = CINT(.5 * iwidth)
  bwidtht = CINT(.75 * iwidth)

  DLTX = .1: DLTY = 200: DLTPX = DLTX: DLTPY = DLTY: xmin = 0:
  xmax = 1: ymin = 0: ymax = 2000
  nax = 1800: NNVAR = 2
  TIT$ = "COUPLE TEMPERATURE VS. TIME": VAR$(0) = "TIME": VAR$(1) = "TEMP": ITICK = 1

  xmin = 0: xmax = 1.8
  ymin = 0: ymax = 1400
CALL MIX(bwidth, nax, TC())  'convolve TC
CALL TILT(bwidtht, nax, TC()) 'Convolve TC
OPEN "tcsi109.dat" FOR OUTPUT AS #1
  FOR ii = 1 TO nax
      yy(ii) = TC(ii - 1)
      xx(ii) = (ii - 1) / 1000
      WRITE #1, .065 * (yy(ii) - 20), xx(ii) * 1000 + 420 'EMF, Time in ns
   NEXT ii
CALL AXES(xmin, xmax, DLTX, DLTPX, ymin, ymax, DLTY, DLTPY, ITICK, JLOG, TIT$, VAR$())
CALL PLOT(iplot, nax - 1, xmin, xmax, ymin, ymax, xx(), yy())
CLOSE

STOP

960 REM DIFFEQ PUSHER,
 'TSM = TEMP EXTRAPOLATION OF Material 0 NEAR Interface
 'TLM = TEMP  EXTRAPOLATION OF Material 1 NEAR Interface
 'LSLOP= DT/Dx ON Material 0 SIDE OF INTERFACE
 'RSLOP= DT/Dx ON Material 1 SIDE OF INTERFACE

 FOR N = 1 TO nmax
     IF T(N) > TM THEN
          TP(N) = TP(N) + T(N) - TM
          T(N) = TM
          IF TP(N) > delTMelt THEN STOP
     END IF
 NEXT N

 Told = T(0)        'simplIFY calc.
 FOR N = 1 TO nmid - 1
    TNEW = T(N) + LS * (T(N - 1) - 2 * T(N) + T(N + 1)) + Lbeta * (Ti(N) - T(N))
```

```
   IF TP(N) > 0 THEN
     TP(N) = TP(N) + TNEW - T(N)
     IF TP(N) < 0 THEN
          TNEW = TNEW - TP(N)
          TP(N) = 0
     END IF
     TNEW = T(N)
   END IF
   Ti(N) = Ti(N) + Lgamma * (T(N) - Ti(N))
     IF Told = T0 THEN RETURN
     T(N - 1) = Told
   Told = TNEW
NEXT N

'INTERFACE TEMPERATURE CHANGE
N = nmid - 1
Told = T(N) + LS * (T(N - 1) - T(N)) - (T(N) - T(N + 1)) / (1 / 2 / LS + 1 / 2 / RS)
Told = Told + Lbeta * (Ti(N) - T(N))
N = nmid
TNEW = T(N) + RS * (T(N + 1) - T(N)) - (T(N) - T(N - 1)) / (1 / 2 / LS + 1 / 2 / RS)
TNEW = TNEW + Rbeta * (Ti(N) - T(N))
   IF TP(N) > 0 THEN
     TP(N) = TP(N) + TNEW - T(N)
     IF TP(N) < 0 THEN
          TNEW = TNEW - TP(N)
          TP(N) = 0
     END IF
     TNEW = T(N)
   END IF
Ti(N) = Ti(N) + Rgamma * (T(N) - Ti(N))
T(N - 1) = Told
Told = TNEW


FOR N = nmid + 1 TO nmax - 1
   TNEW = T(N) + RS * (T(N - 1) - 2 * T(N) + T(N + 1)) + Rbeta * (Ti(N) - T(N))
   IF TP(N) > 0 THEN
     TP(N) = TP(N) + TNEW - T(N)
     IF TP(N) < 0 THEN
          TNEW = TNEW - TP(N)
          TP(N) = 0
     END IF
     TNEW = T(N)
   END IF
   Ti(N) = Ti(N) + Rgamma * (T(N) - Ti(N))
   T(N - 1) = Told
   Told = TNEW
NEXT N
T(N - 1) = Told
RETURN
```

```
1440 ' ******* NUMERICAL INTEGRATION FOR ENERGY IN PARTICLE ; J/KG
     ETOT1 = 0: ETOT2 = 0

     ETOT1 = ETOT1 + .5 * (T(0) - T0) + TP(ii)
     ETOT1 = ETOT1 + .5 * (Ti(0) - T0) / po

     FOR ii = 1 TO nmid - 1
      ETOT1 = ETOT1 + (T(ii) - T0) + TP(ii)
      ETOT1 = ETOT1 + (Ti(ii) - T0) / po

     NEXT ii
     Tmean1 = ETOT1 / (.5 + nmid - 1) / (1 + 1 / po)
     ETOT1 = ETOT1 * Kl / ALL / Roel / 1000 / (.5 + nmid - 2) / (1 + 1 / po)

     ETOT2 = ETOT2 + .5 * (T(nmax) - T0) + TP(ii)
     ETOT2 = ETOT2 + .5 * (Ti(nmax) - T0) / po

     FOR ii = nmid TO nmax - 1
       ETOT2 = ETOT2 + (T(ii) - T0) + TP(ii)
       ETOT2 = ETOT2 + (Ti(ii) - T0) / po
     NEXT ii
     Tmean2 = ETOT2 / (nmax - nmid - .5) / (1 + 1 / po)
     ETOT2 = ETOT2 * KR / ALR / ROES / 1000 / (nmax - nmid - .5) / (1 + 1 / po)
     Tmean = (Tmean1 * (nmid) + Tmean2 * (nmax - nmid)) / nmax
     ETOT = (ETOT1 * nmid + ETOT2 * (nmax - nmid)) / nmax
    RETURN


DEFINT I-K, M-N
'************************* SUB AXES ************************
'
'       Linear Diagram, Plotting, & Screen Printout Subprograms
'X           Horizontal Axis Variable
'Y           Vertical Axis Variable
'
'
'DLTX & DLTY           Scale intervals between printed values along the
'                 X & Y axes
'DLTPX & DLTPY          Scale intervals between scale points along the
'                 X & Y axes
'XMIN & XMAX            Minimum & maximum values of the x axis variable
'YMIN & YMAX            Minimum & maximum values of the Y axis variable
'Nax+1               No. of computed points of the diagram
'x(NAX+1),Y(NAX+1)       Arrays where computed points of the diagram
'                  are stored
'TIT$                 String variable containing the diagram title
'VAR$(0)               X axis variable name
'VAR$(1)               Y axis variable name, for i=1 to NNVAR
'JLOG                 =TRUE for a log (base 10) plot, YMAX & YMIN
'                 must be input as logs of the max and min Y's
'ITICK                =1 for internal grid of ticks
'                 and YY values are logs (LOG(YMAX)/LOG(10),etc)
'IPLOT                =0 to connect data points with lines,
'                 =1 to plot cross at data point,
```

```
’                    =2 to plot crosses and connect points.
’
’*** Diagram Frame & Axes Subprogram ***
’
SUB AXES (xmin, xmax, DLTX, DLTPX, ymin, ymax, DLTY, DLTPY, ITICK, JLOG, TIT$, VAR$())
DIM text(700)
true = -1
’...Draw figure frame & axes........................
CLS : SCREEN 9, , 0, 0: ’set screen up for 640x350 graphics, establish plot margins
      xl = xmin - .12 * (xmax - xmin)
      yl = ymin - .19 * (ymax - ymin)
      xr = xmax + .09 * (xmax - xmin)
      yu = ymax + .05 * (ymax - ymin)
WINDOW (xl, yl)-(xr, yu)
’
’ draw plot frame ..................................
LINE (xmax, ymax)-(xmin, ymin), , B
’
’...Tick Axes and Set unit points on the  axes.......
’
delx = .01 * (xmax - xmin): ticlen = .01 * (ymax - ymin): iflag = 1
’
FOR X = xmin TO xmax + delx STEP DLTPX
   IF ITICK = 1 THEN
      LINE (X, ymin)-(X, ymax), , , &H5500’dotted vertical line
   ELSE
      LINE (X, ymin)-(X, ymin + ticlen): LINE (X, ymax)-(X, ymax - ticlen)’ticks
   END IF
’  Label point with value if interval is dltx
   IF ABS((X - xmin) / DLTX - CINT((X - xmin) / DLTX)) < .05 THEN
        xval$ = STR$(FIX(X) + CINT(10000 * (X - FIX(X))) / 10000)
        yposn = ymin - .02 * (yu - yl)
        CALL TEXTPRINT(xval$, X, yposn, iflag)
   END IF
NEXT X
’
dely = .01 * (ymax - ymin): ticlen = .01 * (xmax - xmin): iflag = 3
’
FOR Y = ymin TO ymax + dely STEP DLTPY
   IF ITICK = 1 THEN
      LINE (xmin, Y)-(xmax, Y), , , &H5500’dotted horizontal line
   ELSE
      LINE (xmin, Y)-(xmin + ticlen, Y): LINE (xmax, Y)-(xmax - ticlen, Y)’ticks
   END IF
’  Label point with value if interval is dlty
   IF ABS((Y - ymin) / DLTY - CINT((Y - ymin) / DLTY)) < .05 THEN
      IF JLOG = true THEN YVAL = 10 ^ Y ELSE YVAL = Y
      YVAL$ = STR$(FIX(YVAL) + CINT(10000 * (YVAL - FIX(YVAL))) / 10000)
      xposn = xmin - .01 * (xmax - xmin)
      CALL TEXTPRINT(YVAL$, xposn, Y, iflag)
   END IF
NEXT Y
’
’
```

```
'TITLE PLOT AND AXES ..................................
'
xposn = (xmax + xmin) / 2: yposn = ymin - .11 * (ymax - ymin): iflag = 2
CALL TEXTPRINT(VAR$(0), xposn, yposn, iflag)'print x-axis name
yposn = yu - .12 * (yu - yl): xposn = xl: iflag = 0
CALL TEXTPRINT(VAR$(1), xposn, yposn, iflag)'print y-axis name
xposn = (xmax + xmin) / 2: yposn = yl: iflag = 4
CALL TEXTPRINT(TIT$, xposn, yposn, iflag)'print plot title
'
END SUB

DEFINT I-J, M-N
'*************************** SUB MIX *******************************
SUB MIX (bwidth, nax, TC())
DIM T(nax)
'Convolve thermocouple curve with triangle function to simulate blurring of
'thermocouple boundary by particle stacking. normalize triangle.
'boundary is 2 * iwidth1 in total width.
 bwsqt = (bwidth + 1) ^ 2
 FOR ii = -100 - bwidth TO nax - 100 - bwidth

     TCT = 0
      FOR jj = -bwidth TO bwidth
      IF ii + jj < 1 THEN
          TCT = TCT + 20 * (bwidth + 1 - ABS(jj))
      ELSEIF ii + jj > nax THEN
              TCT = TCT + TC(nax) * (bwidth + 1! - ABS(jj))
      ELSE
              TCT = TCT + TC(ii + jj) * (bwidth + 1! - ABS(jj))
      END IF
      NEXT jj
     T(ii + 100 + bwidth) = TCT / bwsqt

 NEXT ii
 FOR ii = 0 TO nax
     TC(ii) = T(ii)
 NEXT ii
END SUB

DEFINT I-K, M-N
'**************************** SUB PLOT ******************************
'*** Plotting Subprogram   ****************************************
'
'Can be called more than once to plot several curves in the same diagram
'
'Connect points in the diagram
SUB PLOT (iplot, nax, xmin, xmax, ymin, ymax, X(), Y()) STATIC
'    limit plot to plotting area
 VIEW SCREEN (PMAP(xmin, 0), PMAP(ymin, 1))-(PMAP(xmax, 0), PMAP(ymax, 1))
'    First plot lines (if desired) then mark data points
    IF iplot = 0 OR iplot = 2 THEN
          FOR i = 1 TO nax
              LINE (X(i), Y(i))-(X(i + 1), Y(i + 1))
          NEXT i
```

```
    END IF

    IF iplot = 1 OR iplot = 2 THEN
        FOR i = 1 TO nax + 1
            PSET (X(i), Y(i))
            AAA$ = "R2L4R2U2D4"
            DRAW AAA$
        NEXT i
    END IF
    VIEW
END SUB

DEFINT I-K, M-N
'*************************** SUB TEXTPRINT ***************************
'
'
SUB TEXTPRINT (text$, X, Y, iflag) STATIC' ***************************
'  subroutine to place text at an arbitrary location (x,y)
'  The 25th line is used as workspace by this program.
DIM text(1400)
'TEXT$        is up to 80 characters
'(x,y)        is in world coordinates if WINDOW has been used.
'IFLAG        designates point on text rectangle used as reference.
'           =0 : (x,y) is middle left side
'           =1 : (x,y) is middle of top side.
'           =2 : (x,y) is middle of box.
'           =3 : (x,y) is middle of right side.
'           =4 : (x,y) is middle of bottom side.
vchar = 14 'pixels high on EGA
hchar = 8  ' pixels long on EGA
'
'SCREEN 9, , 1, 0'use if 256K of video memory is available (causes screen blink)
LOCATE 25, 1: PRINT text$;
GET (PMAP(0, 2), PMAP(24 * vchar, 3))-
   (PMAP(hchar * LEN(text$), 2), PMAP(25 * vchar - 1, 3)), text
PUT (PMAP(0, 2), PMAP(25 * vchar - 1, 3)), text
'screen 9,,0,0 'use if 256K of video memory is available (causes screen blink)
'
htext = PMAP(0, 3) - PMAP(vchar, 3)'get label height in world units
ltext = PMAP(hchar * LEN(text$), 2) - PMAP(0, 2)'get label length in w. units.
'
xp = X: yp = Y - htext
IF iflag > 0 THEN xp = xp - ltext / 2  'place box position according to iflag
IF iflag = 3 THEN xp = xp - ltext / 2
IF iflag < > 1 THEN yp = yp + htext / 2
IF iflag = 4 THEN yp = yp + htext / 2
'
PUT (xp, yp), text
END SUB

DEFINT I-J, M-N
'******************************** SUB TILT ************************
SUB TILT (bwidtht, nax, TC())
DIM T(nax)
```

```
'Convolve thermocouple curve with box function to simulate tilt of
'thermocouple boundary . normalize box.
'boundary is iwidth in total width.
  bwsq = (2 * bwidtht + 1)

 FOR ii = -100 - bwidtht TO nax - 100 - bwidtht
        TCT = 0
          FOR jj = -bwidtht TO bwidtht
          IF ii + jj < 1 THEN
                TCT = TCT + 20
          ELSEIF ii + jj > nax THEN
                        TCT = TCT + TC(nax)
          ELSE
                        TCT = TCT + TC(ii + jj)
          END IF
          NEXT jj
        T(ii + 100 + bwidtht) = TCT / bwsq

 NEXT ii
 FOR ii = 0 TO nax
        TC(ii) = T(ii)
 NEXT ii
END SUB
```